UNIVERSITY OF SOUTHAMPTON

FACULTY OF PHYSICAL SCIENCES AND ENGINEERING

Optoelectronics Research Centre

Integrated optical microflow cytometer for bead-based immunoassays

By

Jonathan Butement

Thesis for the degree of Doctor of Philosophy

January 2016

UNIVERSITY OF SOUTHAMPTON

ABSTRACT

FACULTY OF PHYSICAL SCIENCES AND ENGINEERING

Doctor of Philosophy

Thesis for the degree of Doctor of Philosophy

Integrated optical microflow cytometer for bead-based immunoassays

By Jonathan Butement

Flow cytometry is an important tool for medicine and biology with applications from clinical diagnosis to investigations of fundamental cell biology. However, traditional flow cytometers are expensive, bulky and complex to operate. Miniaturised flow cytometers or microflow cytometers offer advantages over traditional devices, being compact, cheap and mass producible and would offer the user ease of operation and low sample consumption. A key challenge for developing a microflow cytometer is the integration of the optical components with the fluidics. Integrated optical waveguides offer an ideal method of light control in microflow cytometers as the waveguides are intrinsically aligned to the analysis region during fabrication.

In this thesis the design, fabrication and demonstration of a silica-based microflow cytometer for bead-based immunoassays is presented. The device consists of a rugged monolithic glass chip with integrated waveguides which deliver excitation light to an etched microfluidic channel and collect light transmitted across the channel. The fluidics are designed to employ inertial focusing to reduce signal variation by bringing the flowing beads onto the same plane as the excitation beam.

A fabrication process was developed using techniques common to the microelectronics industry which are scalable for mass production. This process allowed the realisation of devices with waveguides of a range of widths from 2.0 µm and upwards allowing both single mode and multimode operation at the immunoassay analysis wavelengths of 532 nm and 637 nm. Microfluidic channels with rectangular cross sections suitable for inertial focussing with depths of 30 µm were also realised.

Inertial focussing was demonstrated to confine the flowing beads in two dimensions in the microfluidic channel which effectively reduced the fluorescence signal variation in the device to a CV of 29%. The application of the device was demonstrated by the detection of fluorescence from immunoassay beads incubated with the cytokine tumour necrosis factor alpha at 154 pg/ml. Additional functionality of the device was demonstrated with transmission based detection of flowing beads.

Table of Contents

List of Figures

List of Tables

Declaration of Authorship

I, Jonathan Butement declare that this thesis entitled "*Integrated optical microflow cytometer for bead-based immunoassays*" and the work presented in it are my own and has been generated by me as the result of my own original research.

I confirm that:

1. This work was done wholly or mainly while in candidature for a research degree at this University;
2. Where any part of this thesis has previously been submitted for a degree or any other qualification at this University or any other institution, this has been clearly stated;
3. Where I have consulted the published work of others, this is always clearly attributed;
4. Where I have quoted from the work of others, the source is always given. With the exception of such quotations, this thesis is entirely my own work;
5. I have acknowledged all main sources of help;
6. Where the thesis is based on work done by myself jointly with others, I have made clear exactly what was done by others and what I have contributed myself;
7. Either none of this work has been published before submission, parts of this work have been published as [please see List of Publications]:

Signed: ....

Date:..

Acknowledgements

I would like to thank my brilliant supervisors James Wilkinson and John Chad for giving me the opportunity to work with them on such an engaging project. Your guidance, support and jokes were of great value over the course of this project and I wish to express my deepest appreciation to you both.

My thanks goes to the members of my research group, Zilong Wang, Amy Tong, Alina Karabchevsky, Shahab Bakhtiari Gorajoobi and Mohammed Narizee for all your help and the fun times we have shared in the lab, common room and most importantly at parties. Thanks to Armen Aghajani for his entertaining and motivational stories, Dave Rowe for his enthusiasm and programming help and Vinita Mittal for her endless supply of sweet treats.

My appreciation goes to Senthil G. Murugan who has always offered friendly answers to my questions no matter how trivial and has greatly helped me with practical advice in the lab. I would also like to thank Ping Hua for her guidance with polishing and waveguide fabrication.

I am grateful for the help of Neil Sessions, Owain Clark and Mike Perry for the endless hours of training and advice they have offered to me on cleanroom processes.

My thanks goes to the friends who have made my time during my PhD enjoyable and kept me motivated, Khouler, Lewis, Kat, Zatil, Jess, James, Ben and Sarah, thank you to you all.

Finally I would like to thank my family for supporting me through this process. My great bros Ben, Tim and Sam for distracting me at the weekends with surfing and sailing and my fantastic Mum and Dad who have set a great example to me.

Abbreviations

AWG	Arrayed waveguide grating
BPM	Beam propagation method
BSA	Bovine serum albumin
CCD	Charge coupled device
DI	Deionized
DNA	Deoxyribonucleic acid
e-beam	Electron-beam
FWHM	Full width at half maximum
ICP	Inductively coupled plasma
IPA	Isopropyl alchohol
LOC	Lab-on-a-chip
LOR	Lift off resist
MM	Multimode
MMI	Multimode interference (device)
NA	Numerical aperture
PDMS	Polydimethylsiloxane
PECVD	Plasma enhanced chemical vapour deposition
PMMA	Polymethylmethacrylate
RF	Radio frequency
SEM	Scanning electron microscope
SM	Single mode
SNR	Signal to noise ratio
TE	Transverse electric
TM	Transverse magnetic
TNFα	Tumour necrosis factor alpha
UV	Ultra-violet
WG	Waveguide

Symbols

Re_C	Channel Reynolds number
U	Average fluid velocity
U_{max}	Maximum fluid velocity
h	Fluidic channel height
w	Fluidic channel width
D_h	Fluidic channel hydraulic diameter
ρ	Fluid density
μ	Dynamic fluid viscosity
Re_P	Particle Reynolds number
F_L	Net lift force
C_L	Lift coefficient (added number denotes lift direction)
F_D	Stokes drag
U_p	Particle velocity
U_r	Relative velocity of particle
U_L	Lateral particle migration velocity
L_f	Channel length required for equilibrium
L_m	Transverse migration distance
ϕ	Length fraction
V_f	Volume fraction
R	Fluidic resistance
n	Refractive index
λ	Wavelength
A, B, C	Cauchy coefficients
n_c	Waveguide core refractive index
n_s	Substrate refractive index
NA	Numerical aperture
n_i	Propagation medium refractive index
θ_a	Maximum ½ acceptance angle

h_{WG}	Waveguide height
w_{WG}	Waveguide width
v	Normalised frequency
b	Normalised index
n_{eff}	Effective index
ω	spotsize
η	Coupling efficiency
SNR	Signal to noise ratio
T	Transmission
T_B	Baseline transmission
σ_B	Standard deviation of baseline transmission
R	Fluidic resistance
ΔP	Pressure drop
T_C	Hard mask thickness
S	Etch selectivity
t	Time
T_{PS}	PECVD silica thickness
T_{GS}	Germania:silica thickness
T_S	Bulk silica thickness
R_{PS}	PECVD silica etch rate
R_{GS}	Germania:silica etch rate
R_S	Bulk silica etch rate
I	Gaussian fit to intensity distribution
I_0	Peak intensity
b	Peak intensity postion
c	Gaussian function width parameter
R_f	Fresnel reflection
L_I	Insertion loss
L_C	Coupling loss
L_{WG}	Waveguide length
L_P	Propagation loss
P_W	Waveguide output power
P_I	Laser output power
P_{px}	Power in pixel counts
P_{dB}	Power in decibels

I_{px}	Pixel intensity
F	Camera conversion factor
E_p	Photon energy
G	Camera gain
Q_G	Quantum efficiency
E	Energy

Dedicated to my family…

CHAPTER 1
Introduction

1.1 Project motivations

Integrated optics is a technology which enables the combination of multiple optical devices on a single microchip style device [1]. The concept involves producing microstructured, dense optical circuits in a microchip style package which can produce, modulate and analyse light, performing the same role as macro-scale optical devices which use components such lenses, mirrors, filters, gas lasers and photomultiplier tubes. Typically the microstuctured integrated optical components are manufactured in thin dielectric films on planar substrates using fabrication techniques inspired by the microfabrication of integrated electronic circuits such as, sputtering photolithography and etching. Integrated optical devices have a number of key merits over macroscale optical devices. They are cost effective as the fabrication techniques used allow high volume batch production whilst maintaining excellent device uniformity. They produce stable performance as the integrated optical components are permanently aligned on a single substrate making them resistant to vibration and temperature changes with no need for re-alignment by the user. Integrated optical devices can show improved optical functionality over macro-scale optics. They are capable of producing greater optical power densities compared to free space beams which allows nonlinear properties of device materials to be exploited. The confinement of guided waves into the integrated structures also allows fine control over wave behaviour and the length over which light interacts with materials. Finally the devices are compact, and light weight as they are produced on centimetre sized chips.

Integrated optics is a complementary technology for the rapidly expanding lab-on-a-chip (LOC) field which aims to reduce laboratory processing and analytical functions onto miniaturised chips [2]. These devices typically combine micrometre scale fluidic channels (microfluidic channels) with miniaturised optical and electronic actuation and analysis technologies. Microfluidic channels allow the controlled movement of small volumes of fluid which reduces sample consumption, speeds the equilibration of chemical reactions and allows precise reaction times. Circuits of microfluidic channels can be combined on a single chip to perform automated fluid handling processes in parallel with high throughput [3]. Due to the micron scale feature sizes, microfluidic channels are well suited to fabrication using the same production processes as integrated optics allowing easy integration of both technologies into lab on a chip devices which are mass producible and low cost [4]. The possible applications of LOC devices are widespread in chemistry, biology, medicine and agriculture. The compact nature of the technology makes devices portable which has led to efforts to produce devices which can perform rapid diagnosis of a patient in situ such as monitoring blood lithium levels [5]. These point of care devices promise to allow early diagnosis, personalised treatment plans and greater access to medical services. The low costs and simple operation of LOC devices mean that laboratory analysis equipment which was previously an expensive, shared resource operated by specialist technicians can become a personal, everyday lab tool. LOC devices have been developed as cell culture platforms [6], [7], mass spectrometers [8] and immunoassay platforms [9], [10].

1.1.1 Microflow cytometry

One field which can exploit the advantages of lab-on-a-chip integration is flow cytometry. This mature field involves the sequential analysis and sorting of cells or particles. In a typical bench top flow cytometer a suspension of cells or particles is hydrodynamically focussed into a thin stream which passes through a focussed laser beam. The light path is controlled free-space using objective lenses to focus and collect light, mirrors to direct it and beam splitters and filters to separate wavelengths for analysis. Typical sources and wavelengths used are argon ion lasers at 488 nm, frequency doubled Nd:YAG ($Nd:Y_3Al_5O_{12}$ crystal) lasers at 532 nm and laser diodes at 635 nm. Typical optical detectors are photomultiplier tubes and more recently lower cost avalanche photodiodes [11]. Flow cytometers can take a range of optical measurements from flowing particles. The intensity of the light scattered by a particle over a small angle of 0.5-2.0° is proportional to the particle volume [12] whilst the intensity of side scattered light at angles of 90° or more is dependent on internal structure of the particle and can be used to identify cells [13]. Fluorescence emitted from the particle can also be measured, for example cells can be stained with fluorescently labelled antibodies or DNA binding fluorescent dyes in order to identify cell type and function [14].

Microflow cytometry applies the lab-on-a-chip concept to flow cytometry. Much of the work in this field has been directed toward miniaturising the fluidic systems of flow cytometers using microfluidics and particle positioning techniques [15]. Less attention has been paid to full integration of the optical systems and some microflow cytometers still use free-space excitation and collection optics [16]. Partial integration can be achieved by inserting optical fibres into micro fabricated guide channels aligned with microfluidic channels. Good examples of such devices have been used for analysis of phytoplankton [17] and fluorescence measurement of immunoassay beads [18]. These devices can be manufactured at low cost [19] and with low optical losses but the fibre insertion process is hard to upscale for mass production as it still requires some alignment.

1.1.2 Optical waveguides for microflow cytometry

Integrated optics shows promise to allow full integration of light control in microflow cytometry. The fundamental integrated optical component is the waveguide which is a physical structure which guides the direction of light waves. The simplest waveguide structure is the slab waveguide shown in Figure 1.1, which consists of a planar core layer with a substrate underneath and a cladding layer on top. Light which is coupled into a waveguide core below a critical angle will be vertically confined within the core layer by total internal refraction and is known as a guided mode. Guided modes are represented by a constant electric field distribution transverse to the direction of propagation at all points along the propagation length. The dimensions and refractive index contrast of a waveguide system will determine the number of modes supported. Multimode waveguides will support a number of modes, each with a characteristic electric field distribution and each propagating at different velocities while single mode waveguides support only the fundamental mode.

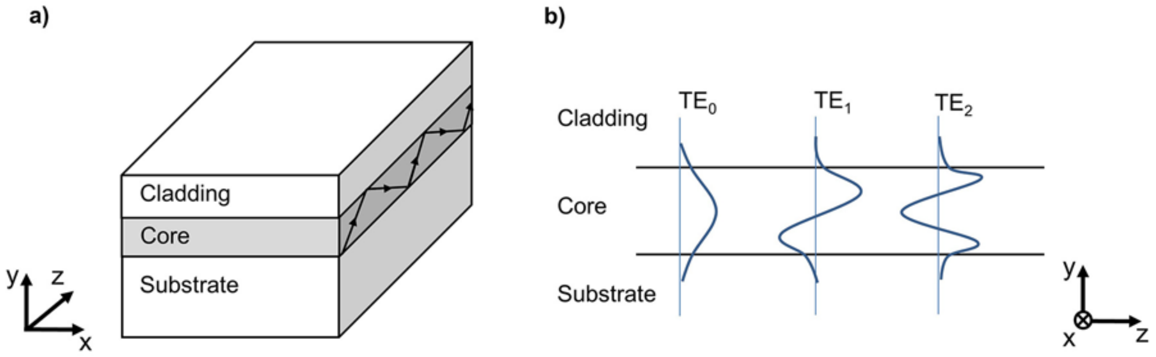

Figure 1.1:(a) Slab waveguide structure with ray diagram of guided mode. (b) Electric field distribution of the first three guided modes in a slab waveguide.

While the 2D structure of a slab waveguide can confine light in one direction, 3D structured waveguides can confine light both vertically and horizontally allowing light to be directed around bends on a chip. Typical structures of 3D waveguides are shown in Figure 1.2 and include channel or strip waveguides, rib waveguides, loaded strip waveguides and diffused waveguides. 3D waveguides are particularly useful in a microflow cytometer as they can be used to guide excitation light to precise locations and collect light from scattering and fluorescence emission at discrete angles and positions. The intrinsic alignment of optical structures during fabrication removes the need for the user to align the optical light path and minimises signal variation caused by moving components. Advanced optical structures can also be included in the optical light path such as multimode interference devices [20] and kinoform microlenses [21] for light focussing and collection as well as arrayed waveguide gratings as spectrometers [22].

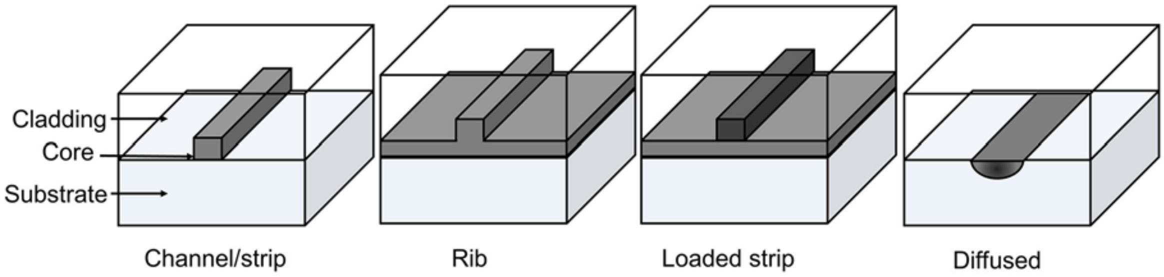

Figure 1.2: Types of 3D waveguide.

A range of waveguide material systems and fabrication techniques are suitable for use in integrated optical microflow cytometers. Polydimethylsiloxane (PDMS) waveguides can be fabricated by mixing different amounts of curing agent to produce different refractive indices in injection moulded structures [23]. Another technique uses photolithography to define waveguides and fluidics simultaneously in a polymer photoresist [24]. Here the waveguide core consists of photoresist and is clad at the side by air gaps and above and below by attached glass slides which also seal the fluidics. Polymer waveguides are appealing as they are often cheap to fabricate requiring low cost materials and processes, they do however suffer from poor fabrication tolerances and mechanical and temperature instability. For example a thermoplastic polymer microflow cytometer with integrated epoxy waveguides was limited to collect forward scatter light at a large angle as waveguides could not be integrated closely enough [25]. Glass based waveguide systems in general offer better optical performance than polymer systems exhibiting low absorption in the visible range [26] and low autofluorescence [27]. They are also mechanically robust and less susceptible to temperature related effects caused by expansion and contraction. Glass based waveguide systems fabricated with highly accurate wafer scale microfabrication techniques can allow realisation of dense and complex optical structures increasing the number of functions that can be performed on a single device [20], [21]. The relatively high costs can be offset by scale and the improved functionality is desirable for researchers. The fabrication processes for microfluidics in glass are well developed [28] but a key challenge is selecting a microfluidic channel design which can use a particle focussing technique suitable for integration with waveguides. A detailed review of particle focussing methods and their suitability for integration is presented in the next chapter. Examples of waveguides combined with rudimentary microfluidic channels in a glass system have been demonstrated [29] however the benefits of such a system have not been implemented in microflow cytometry.

1.1.3 Analysis of bead based immunoassays with flow cytometry

One application of flow cytometry is the analysis of fluorescence from beads used in a bead based immunoassay. The bead based immunoassay is a development of the Enzyme-Linked-Immunosorbent assay (ELISA) [30] and is a way of measuring the concentration of a specific analyte in a liquid biological sample. The protocol for the most popular type of bead based immunoassay, developed by the Luminex corporation is shown in Figure 1.3. Polystyrene beads, 5.6 µm in diameter are functionalised with a capture antibody specific to the analyte of interest. The beads are incubated with a liquid sample containing the free floating analyte where the analyte binds to the detection antibody. A wash step then removes any free floating analyte by removing the liquid and replacing with fresh liquid. A detection antibody, coupled to a fluorescent molecule, R-phycoerythrin (R-PE), is then added to the bead solution and the detection antibody binds to a different binding site on the analyte. A further wash step then removes the free detection antibody and the sample is ready for analysis.

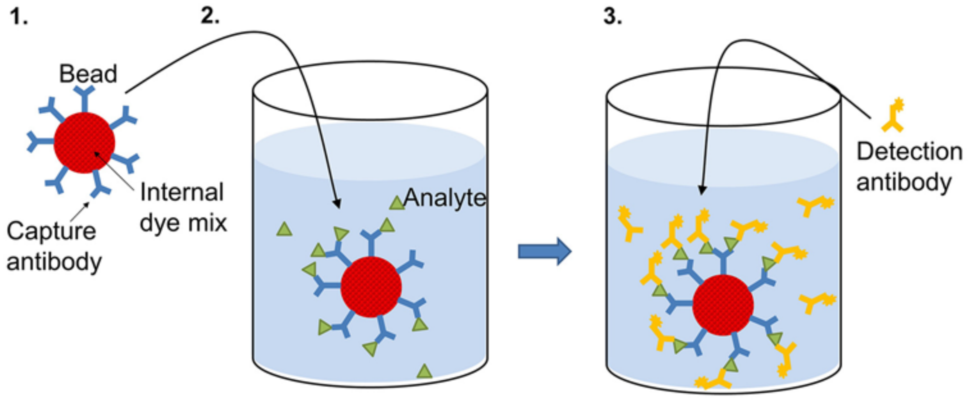

Figure 1.3: Protocol for the bead based immunoassay. 1. Beads functionalised with capture antibody. 2. Incubation of beads in sample with analyte. 3. Addition of fluorophore coupled detection antibody.

A traditional flow cytometer, shown in Figure 1.4, is normally used to analyse the beads. The bead suspension is hydrodynamically focussed into a narrow, high velocity stream and passes through two focussed laser beams. Light at a wavelength of 532 nm excites fluorescence from the R-PE on the detection antibody. The intensity of this fluorescence is proportional to the amount of analyte bound to the bead. Light at a wavelength of 635 nm excites the fluorescence from the two internal fluorescent dyes and the ratio of the fluorescence intensities for the two dyes designates the bead code thus identifying the analyte [31]. This coding system allows up to 100 analytes to be measured simultaneously in the same sample which is ideal for measuring the levels of interdependent signalling molecules such as cytokines [32], [33]. The flow cytometers used to analyse the bead samples cost tens of thousands of pounds and are usually a shared resource between labs which requires specialist technical support. Microflow cytometers should provide a cost effective, easier to use analysis technology greatly increasing access for researchers.

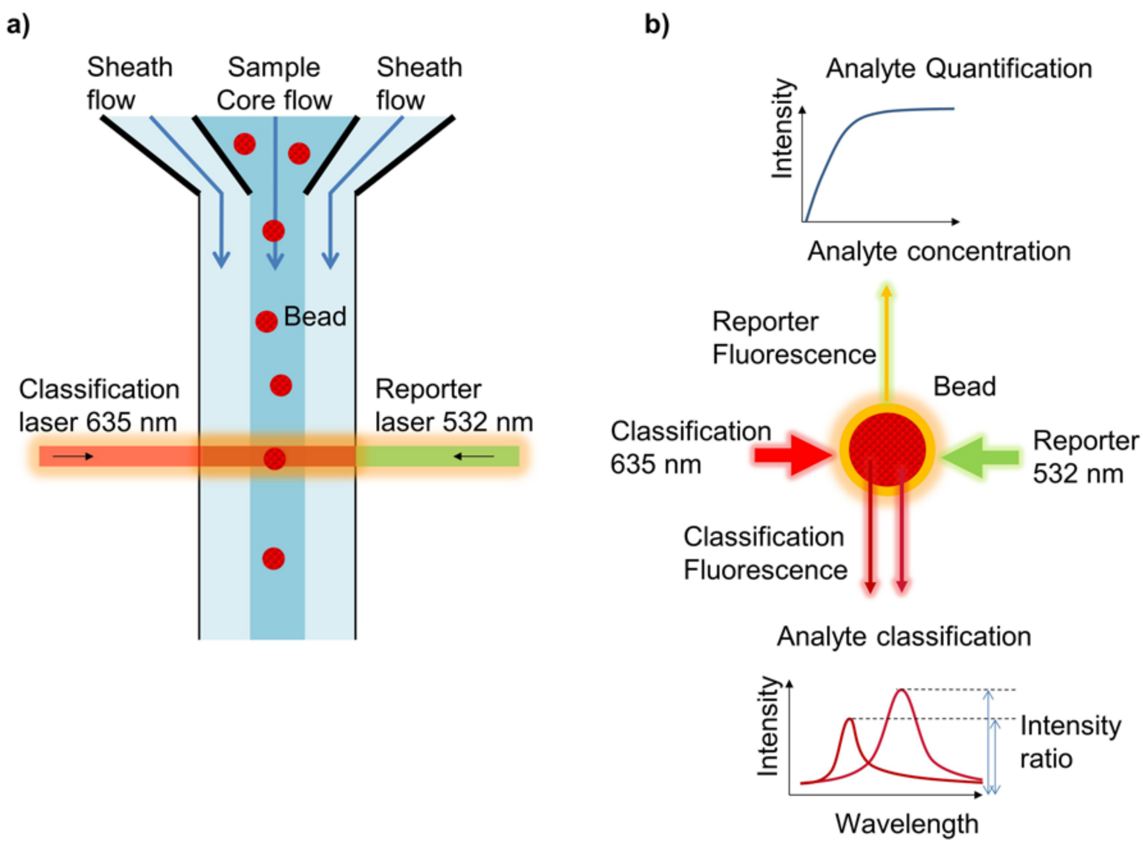

Figure 1.4: (a) Hydrodynamic focussing of beads in Luminex flow cytometer through laser illuminated region. (b) Analysis of the reporter and classification fluorescence.

1.2 Project aim

The aim of this project was to develop a viable microflow cytometry platform benefiting from full integration of waveguides and microfluidics in a monolithic silica chip. To demonstrate the use of the flow cytometer the application selected was that of measuring the fluorescence from beads used in an immunoassay. In order to achieve this aim a series of objectives were identified as follows.

1. Selection of a particle focussing method suitable for combination with integrated waveguides and the design of a microfluidic channel which employs this method.
2. The design of an optical light path using integrated waveguides suitable for excitation of beads at wavelengths of 532 nm and 635 nm and collection of light from the microfluidic channel.
3. Development of a fabrication process capable of mass producing microflow cytometer devices to the design specification.
4. Demonstration of excitation and measurement of fluorescence from flowing beads using fabricated devices.
5. Demonstration of analysis of flowing beads using light collected by waveguides in fabricated devices.

1.3 Structure of thesis

This thesis describes the process taken to achieve the project aim and is structured as follows:

This chapter has introduced the areas of integrated optics and lab-on-a-chip technology and identified the motivation for using integrated optical waveguides as a means to control light in a microflow cytometer.

Chapter 2 reviews the available techniques for focussing of flowing particles in microflow cytometry and assesses their suitability for integration with waveguides in a glass chip. The most suitable technique, inertial focussing is described in detail.

Chapter 3 describes the design of the optical light path using numerical simulations. The effect of the waveguide dimensions are investigated to understand the modal behaviour of the waveguides and optimise input and output coupling efficiency. The optical transmission across a microfluidic channel is simulated to inform the design of the microfluidic channel in the next chapter. The effect of flowing beads on the optical transmission across the microfluidic channel is simulated and presented as a means to detect flowing beads.

Chapter 4 finalises the design of the microfluidic channel that is suitable for inertial focussing of immunoassay beads. The fabrication processes used for the production of the monolithic silica based microflow cytometer devices are then described.

Chapter 5 describes the optical characterisation of the waveguide performance and illumination beam in the fabricated devices. The propagation losses are measured and the modal behaviour of the waveguides is analysed and compared to the simulations. The insertion loss incurred by the microfluidic channel is measured and the illumination beam in the microfluidic channel is imaged.

Chapter 6 presents three studies which evaluate the performance of the fabricated devices according to the design specification. First, the extent to which inertial focussing is occurring in the microfluidic channel and its effect on signal variation is assessed. Second, a device is used to measure the fluorescence from beads used in an immunoassay for the cytokine tumour necrosis factor alpha. Third a device is used for transmission based detection of flowing beads.

Chapter 7 summarises the achievements and conclusions of this work and suggests future areas for development of the integrated optical microflow cytometer.

CHAPTER 2

Particle focussing methods in microflow cytometry

2.1 Introduction

A key requirement for flow cytometry is to accurately control the positioning of particles transverse to the direction of flow in order to minimise signal variation as the particles pass through the analysis region. An excitation beam has a varying transverse intensity distribution and so any positional variation of fluorescent particles as they pass through the beam will result in varying fluorescence emission.

A variety of techniques are used in microflow cytometry to achieve particle positioning and these will be discussed in this chapter with the aim of identifying a suitable technique to combine with integrated optics for the analysis of fluorescent beads. The technique must be simple to fabricate to minimise fabrication time and costs, making mass production easier. In addition it is important that the operation of the device remains as simple as possible as the addition of multiple fluidic/electronic/magnetic controls can introduce operational error and also add to the bulk of the device reducing portability.

2.2 Sheath flow based focussing

Sheath flow based particle focussing is widely used in traditional bench top flow cytometers and involves injecting the sample stream into a faster flowing stream of sheathing fluid which surrounds the sample stream. The surrounding pressure narrows the cross sectional diameter of the sample stream core causing confining the sample particles in two dimensions as they pass through the analysis region. The main advantage of sheath based techniques is the ability to adjust the core stream diameter by adjusting the core to sheath fluid flow rate ratio which allows adjustment for different particles sizes. The sheath fluid also prevents the sample from touching the sides of the fluidic channel which reduces fouling and clogging problems. Disadvantages of sheath based methods are difficulty in recovering sample, high sample consumption and sheathing fluid consumption as well as the requirement for additional pumps for the sheathing fluid.

Sample streams can be focussed with sheath fluid in one dimension in microfluidic chips by having the sample stream injected between two sheath fluid inlets either side [34], [35]. Two dimensional focussing requires more complex channel geometries which in turn require more complex, multistep fabrication processes. Attempts have been made to mimic the conical nozzle system in microfluidic channels by using a suspended sample injector channel and a sloped floor to redirect sheath flow in the vertical direction as well as horizontally. The sloped floor is fabricated by tilt exposure of a negative photoresist film [36]. The process is impressively intricate, this is a drawback however when considering mass production as it requires modification of standard photolithography equipment and additional processing time and expertise. Integration of the negative photoresist microfluidic with glass waveguides can also prove a challenge and negate the advantages of using an all glass system.

Another sheath based approach, shown in Figure 2.1, is to use pairs of chevron shaped grooves in the wall and floor of the channel to redirect some of the sheath flow from side inlets above and below the sample stream causing vertical confinement [37], [38]. Adjustment of core width can still be achieved by adjusting the relative flow rates of the sample and sheath fluid and the core height can be adjusted by changing the number of chevron pairs. Grooved microfluidic channels are fabricated by micro-milling polymer blocks or by injection moulding of polydimethylsiloxane (PDMS). Top and bottom halves are manufactured separately and then aligned and bonded together. A microflow cytometer with groove generated sheath flow and inserted optical fibres for fluorescence collection and excitation was demonstrated for analysis of a multiplex bead based assay [18], [38] and also phytoplankton [17]. It is possible to make such grooved structures in glass using micro-milling techniques [39] however such direct write techniques are not well established in mass production and requires specialist skills.

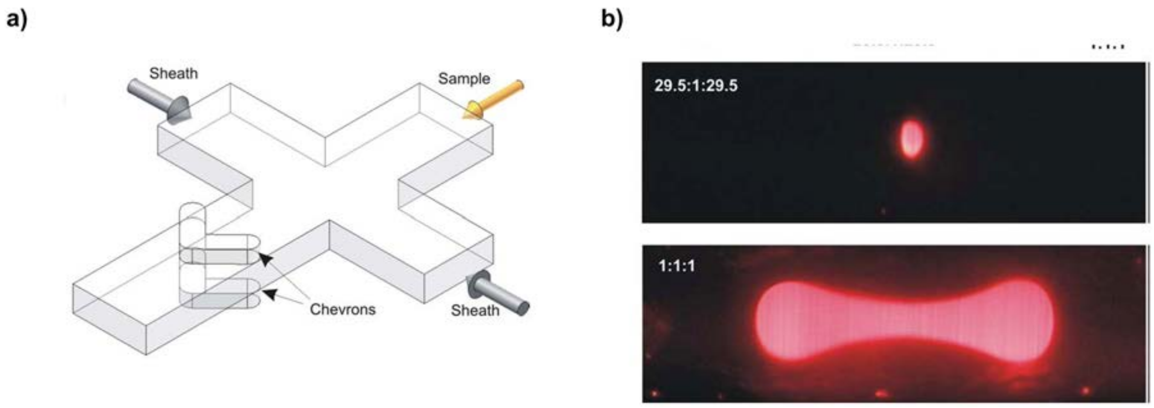

Figure 2.1: (a) Microfluidic channel structure for groove generated 2D sheath based focussing. (b) Fluorescence image of core sample stream cross section demonstrating confinement of the core stream diameter by increased sheath fluid to core fluid flow rate ratio. Images taken from [37]

Efforts have been made to reduce the complexity of 2D sheath focussing designs to make the fabrication less complex. One method, requiring only one sheath flow input for 2D focussing uses a rectangular cross section channel with abrupt contractions and expansions in width shown in Figure 2.2 (a). Here a sheath flow is injected through a single inlet next to the sample flow inlet, when the flow reaches a contraction region lateral vortices, known as Dean flow are induced, redirecting the sheath fluid above and below the sample flow causing vertical confinement. Repeating expansion and contraction regions decelerate and accelerate the flow velocity respectively maintain the Dean flow vortices in a single direction which eventually leads the sample flow stream becoming completely enveloped in sheath flow. Such a design was used to focus a sample flow containing red blood cells [40]. Such types of channels are simple to fabricate with standard glass microfabrication techniques such as photolithography and etching however the design has a drawback that sample particles can get caught in the dead volume of the expansion regions which would pose a possible contamination problem between samples.

Overall sheath based particle focussing methods are well established in microflow cytometry however the requirement for a sheath fluid is a significant drawback as it adds operation complexity and large quantities of sheath fluid are required. Sheathless focussing techniques are also available and will now be discussed.

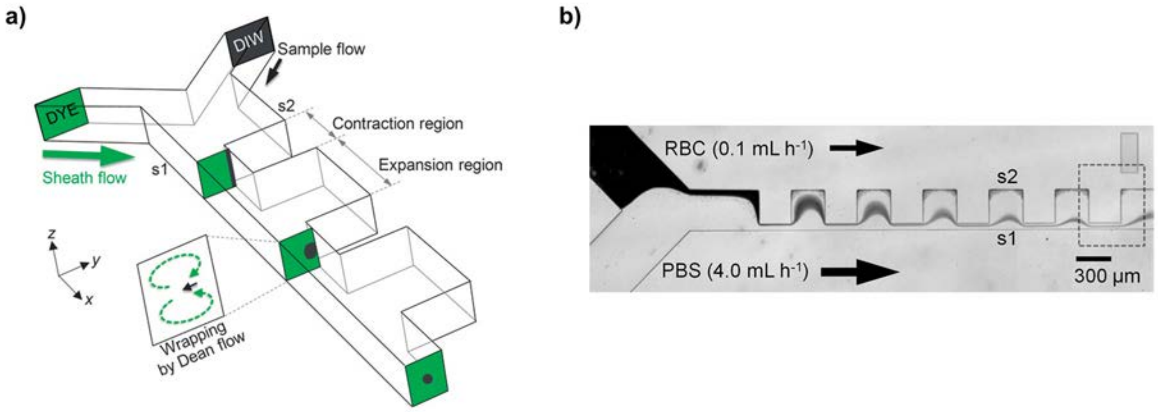

Figure 2.2: (a) Channel structure for 2D sheath based focussing using Dean flow. (b) Demonstration of focussing of a core stream containing red blood cells. Images taken from [40].

2.3 Magnetic focussing

If the particles of interest are magnetic, a magnetic field can be used to focus them in 2D. This is especially relevant for bead-based immunoassays which can be performed on magnetic particles [41]. One method uses a narrow magnetic tip located next to the channel side wall to hold a plug of magnetic beads half-way up the height of the channel side wall. The magnetic retention force is slowly reduced and fluid flow causes the magnetic particles to be released in an evenly spaced stream. Further downstream a single fluid inlet from the same side as the magnetic tip pushes the flowing particles away from the wall to the centre of the channel [42]. Whilst this technique can exploit the magnetic properties of magnetic beads, the system requires careful alignment of the fluidic chip with the magnetic tips, making it less user friendly. There is additional complexity if this technique were to be used with integrated optical chips which also require optical fibre inputs near the region of the magnetic tips. Perhaps most significantly the stop-flow operation of this technique can limit high throughput analysis of thousands of beads.

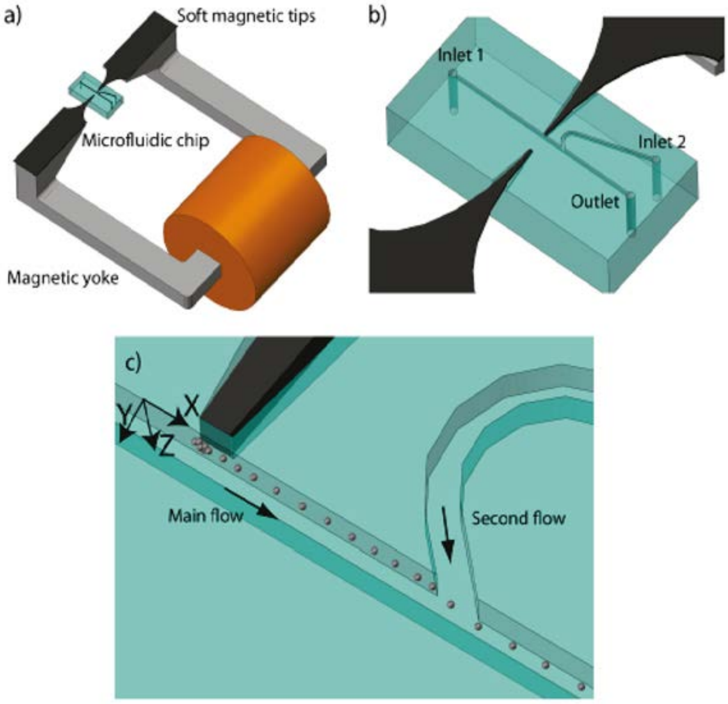

Figure 2.3: Magnetic focussing of beads (a) Magnetic tips attached to a magnetic yoke controlling the strength of the magnetic field. (b) Microfluidic channel layout. (c) Release of magnetically captured beads and introduction of lateral secondary flow producing 2D focussing. Image taken from [42]

2.4 Dielectrophoretic focussing

Dielectrophoretic focussing uses the force applied to a dielectric particle due to the application of a non-uniform, AC electric field to focus particles in to a narrow stream for analysis. Applying the electric field to the particle solution induces a dipole moment in the particle causing the particle to move towards or away from the region of maximum field strength. Particles or cells can be focussed using a positive or negative dielectric force. In positive dielectrophoresis particles are more polarizable than the surrounding fluid and so the particle moves towards the region of maximum electric field strength. In negative dielectrophoresis particles is less polarisable than the surrounding fluid the particle moves away from the region of maximum field strength. 3D negative dielectric focussing has been demonstrated with latex beads. Here latex beads were passed down a 100 µm, channel with an elliptical cross section. Electrodes were patterned around the internal circumference of the channel at intervals along its length. Particles could be focussed into a core stream of 15 µm diameter [43]. Another chip design uses a simpler planar set of electrodes patterned on the floor and roof of a microfluidic channel to vertically focus polystyrene beads using negative dielectrophoresis for a bead based immunoassay [16], [44].

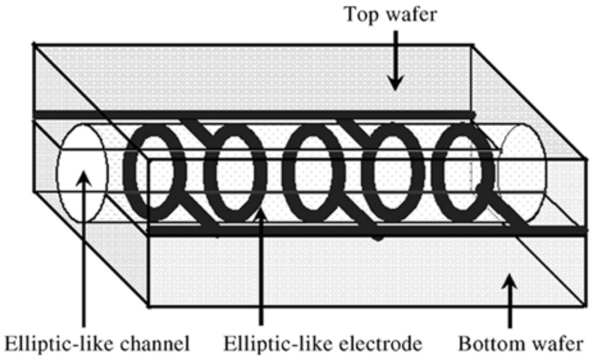

Figure 2.4: Showing the elliptical cross section channel and patterned electrodes used in dielectric focussing in [43].

Dielectrophoretic focussing methods show good potential for fully integrated lab-on-a-chip devices as the method can also be used for particle sorting after identification [45]. They do not require sheath input but do require electrical connections to be made to the device. The patterning of the electrodes is an additional fabrication step which adds to the fabrication time of a device and can reduce yield increasing costs. An integrated optical device with waveguides and fluidics already has a minimum of two photolithographic stages.

2.5 Inertial focussing

Inertial focussing is a phenomenon by which flowing particles become subject to lateral forces known as lift forces which cause the particles to migrate across fluid streamlines to equilibrium positions defined by the channel geometry. The technique is appealing as a particle positioning tool for combination with integrated optics as it requires simple channel geometries, usually square or rectangular cross section channels with smooth walls, which are easy to fabricate with well-established methods such as etching. No sheath fluid is required which minimises the complexity and bulk of the device.

Inertial focussing of flowing particles was first observed in the 1960s [46] however it was not until the establishment of microfluidics that the concept found a suitable application. In 2007 Di Carlo et al. published the first example of inertial focussing in rectangular cross section microfluidic channels and identified the relevant applications of cell and particle positioning [47]. Since then many studies have added to the understanding of the mechanisms behind inertial focussing and the cause of inertial lift forces by a variety of experimental, numerical and some analytical studies. Martel et al. [48]and Amini et al. [49] provide useful reviews of inertial focussing in microfluidics.

For inertial focussing to take effect the inertial forces on the particle must be significant. The channel Reynolds number, Re_C, describes the ratio of inertial forces to viscous forces acting on a fluid flowing in a microfluidic channel.

$$Re_C = \frac{\rho U_{Max} D_h}{\mu} \qquad 2.1$$

Where ρ is the fluid density, U_{Max} is the fluid maximum velocity ($U_{Max} = 2U$, where U is average flow velocity), D_h is the hydraulic diameter of a rectangular cross section channel ($D_h = 2hw/(h+w)$, where h is the height and w is the width of the channel cross section) and μ is the dynamic fluid viscosity. Typically flow in microfluidic channels has a low channel Reynolds number, usually less than 1, because of the small dimensions.

At low channel Reynolds numbers fluid flows in layers parallel to the channel length and is said to be laminar with no turbulence. These layers, or streamlines have a parabolic transverse velocity profile meaning that flow is fastest at the centre of the channel and decreases to zero at the channel wall. When considering particles flowing in a fluid, as in flow cytometry the particle Reynolds number Re_p relates the ratio of inertial to viscous forces acting on the fluid at the particle length scale.

$$Re_p = Re_C \left(\frac{a}{D_h}\right)^2 = \frac{\rho U_{Max} a^2}{\mu D_h} \qquad 2.2$$

Here a is the particle diameter. Inertial effects begin to arise when there is a large velocity gradient across the particle leading to larger lift forces. This may be due to a low fluid viscosity but is more typically due to a high flow velocity, or large particle diameter relative to the hydraulic diameter. A particle is said to be flowing in the inertial focussing regime when the particle Reynolds number is greater than or equal to 1 [50]. For example, in the case of the polystyrene Luminex immunoassay beads ($a = 5.6$ µm) suspended in water ($\rho = 1000$ kg/m^2 and $\mu = 1 \times 10^{-3}$ Pas) flowing in a rectangular cross section channel of dimensions $h \times w = 30 \times 20$ µm^2, then $Re_P > 1$ when $Q >$ 0.16 µl/s ($U_{Max} >$ 0.53 m/s).

A particle flowing in the inertial focussing regime is subject to two main forces which cause lateral migration across fluid streamlines, the shear gradient lift force and the wall effect lift force. Figure 2.5 shows these inertial lift forces acting on a particle in a microfluidic channel. The shear gradient lift force acts to move the particle away from the central axis of the channel. This force arises from the parabolic fluid velocity profile in the microfluidic channel. The velocity of the particle U_p lags behind the fluid and so the fluid has a relative velocity to the particle, $U_r = U_p - U$. The relative fluid velocity is faster on the side of the particle facing the centre of the channel and slower on the side facing the wall. As a result of the differential fluid velocity across the particle diameter a net force is produced down the fluid velocity gradient toward the channel wall [51].

The wall effect lift force acts to move the particle toward the central axis of the channel. It arises in a similar way to the action of an aeroplane wing. The particle lagging behind the flow causes the fluid streamlines to be directed around the particle. The fluid passing over the particle on the side facing the centre of the channel is accelerated around the particle resulting in a lower pressure compared to the fluid passing by the more direct route between the particle and the wall producing a net force acting away from the wall [52]. The wall effect lift force increases rapidly with proximity to the channel wall and so only begins to significantly oppose the shear gradient lift force as the particle approaches the channel wall [53]. A particle with a random position in a channel is subject to both opposing forces and will migrate laterally until it reaches an equilibrium position where the forces are equal. Once at this equilibrium position the particle will remain flowing along that streamline unless acted on by an external force.

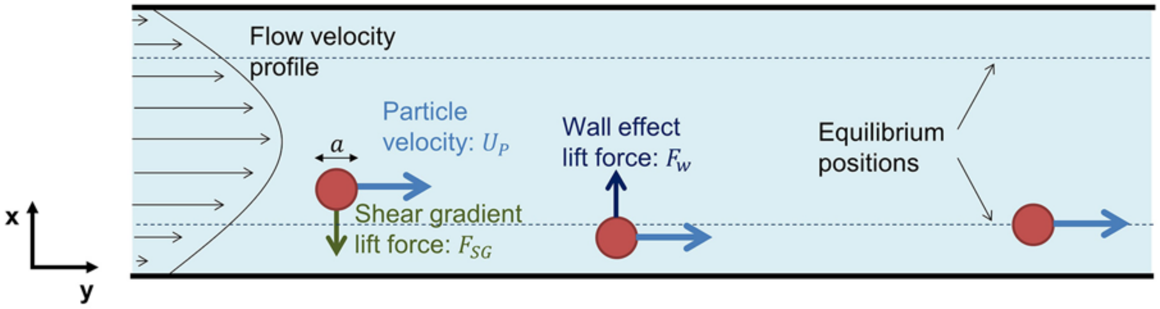

Figure 2.5: Inertial lift forces acting on a particle in a microfluidic channel to bring it to an equilibrium position.

The net inertial lift force, F_L acting on a particle was described by Asmolov using the following equation [52], [54].

$$F_L = \frac{C_L \rho {U_{Max}}^2 a^4}{D_h^2} \qquad 2.3$$

The non-dimensional lift coefficient C_L, scales with particle position within the channel cross section and the channel Reynolds number. When considering flows at $Re_C < 100$, the variation in C_L with particle position is low and so an average value of $C_L \approx 0.5$ can be used to estimate the lift force on a particle positioned near the centre of the channel [47], [52]. For a typical immunoassay bead with $a = 5.6$ µm flowing down an example microfluidic channel with $h \times w = 30 \times 20$ µm^2 at $Re_P = 1$ the inertial lift force directing the particle towards the long channel wall is ≈ 0.2 nN.

The inertial lift force can be used to calculate the lateral migration velocity of a particle, U_L, by balancing the net inertial lift force with stokes drag, $F_D = 3\pi\mu a U_L$.

$$U_L = \frac{C_L \rho {U_{Max}}^2 a^3}{3\pi\mu D_h^2} \qquad 2.4$$

Under the conditions of the previous example with an immunoassay bead, a bead near the channel centre will laterally migrate at a speed of ≈ 4.6 mm/s towards the long channel wall.

The geometry of the channel cross section determines the number and positioning of the equilibrium positions. Figure 2.6 shows the equilibrium positions for a square cross section channel and rectangular cross-section channel. In the square cross section channel shown in Figure 2.6 (a) there are four equilibrium positions close to the walls, centred on each face. This is due to the four-fold rotational symmetry of the square cross-section. If the aspect ratio of the channel is stretched to that of a rectangle with a height: width ratio of 3:2 or greater then there are only two equilibrium positions close to the wall, centred on the long faces, as shown in Figure 2.6 (b). In such a channel the fluid velocity profile parallel to the short face of the channel is steeper than the velocity profile parallel with the long face of the channel and as such the shear gradient force acting towards the long faces is greater than that acting towards the short faces. Inertial focussing in this case occurs in two stages. In stage 1, particles entering the channel have a greater probability of being initially forced towards a long channel face. Subsequently, in stage 2, as the particle approaches the long face of the channel the wall effect lift forces from the two short faces push the particle to the centre of the long face. Stage 1 migration is a fast process occurring over a short downstream distance and stage 2 migration is a slower process occurring over a longer downstream distance [54].

In a rectangular cross-section channel, the downstream distance required for flowing particles to migrate to an equilibrium position, L_f, can be estimated by calculating the particle migration velocities for stage 1 and stage 2 of migration. As each stage of migration occurs under different fluid velocity profiles, each has a different lift coefficient denoted C_{L1} for stage 1 migration parallel to the channel short face (w) and C_{L2} for stage 2 migration parallel to the channel long face (h). The following equation derived from equation 2.4 is used to calculate L_f [54].

$$L_f \approx \frac{3\pi\mu D_h^2}{2\rho U a^3}\left(\frac{w}{C_{L1}} + \frac{h}{C_{L2}}\right), w < h \qquad 2.5$$

If the lift coefficients for each stage of migration are not known then they can be calculated by experimentally measuring the distance required for particles to migrate to equilibrium in each dimension and using the equation below [54].

$$C_L = \frac{3\pi\mu D_h^2}{2\rho U a^3} \times \frac{L_m}{L_f} \qquad 2.6$$

The transverse migration distance L_m depends on the direction of migration so that $L_m = w/2$ for stage 1 migration and $L_m = h/2$ for stage 2 migration when $h > w$.

In rectangular cross section channels, when particle concentrations are sufficiently high so that the inter-particle distance between inertially focussed particles is below 4 particle diameters then inter particle interaction leads to flow with a staggered, even spacing, as shown in Figure 2.6. The inter-particle spacing, d, for a suspension in a channel can be calculated with the following equation.

$$d = \frac{a(2-\phi)}{\phi} \qquad 2.7$$

Here the fraction of particle diameters per unit of channel length $\phi = (6whV_f)/(\pi a^\wedge 2\,)$ where V_f is the volume fraction of the particle suspension. The ordering of particles in the direction of flow is useful for high throughput flow cytometry as it prevents double signals caused by two beads passing through the illumination region simultaneously [50]. In the previously used example with Luminex immunoassay beads, longitudinal ordering will occur when the immunoassay bead concentration is >1.2×10^5 /µl.

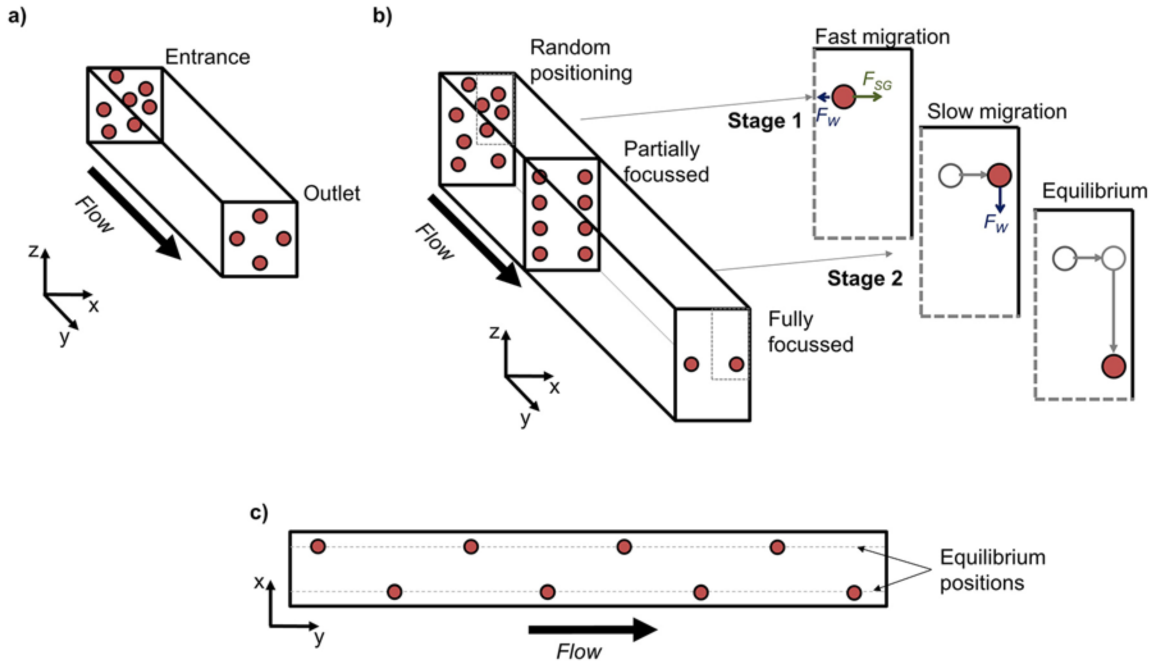

Figure 2.6: (a) Inertial focussing equilibrium positions in a square cross section channel. (b) Inertial focussing in a rectangular cross section channel showing fast, stage 1 migration towards the long face and slow, stage 2 migration towards the centre of the long face. (c) Fully inertial focussed beads in a rectangular cross section channel proceed with a staggered, even spacing at high concentrations.

The location of the equilibrium positions can be affected by the particle Reynolds number. As the particle Reynolds number increases the equilibrium positions shift closer to the channel walls as the shear gradient force increases relative to the wall effect lift force [55]. In rectangular cross section channels higher particle Reynolds numbers can lead to an additional two equilibrium positions centred on the short faces of the channel as the significance of the wall effect lift has been reduced. Experimental observations have concluded that a channel Reynolds number between 0.94 and 1.87 produce 2 typical equilibrium positions whilst $Re_P > 4.6$ leads to 4 focusing positions [50], [56].

Most inertial focussing microflow cytometers demonstrated in the literature use free-space optics for fluorescence excitation and detection [50], [57] but there has been one example of the technique being used with integrated optics in a polymer based chip [25]. This chip is produced by moulding of cycloolefin copolymer (COP) against a photolithographically produced master. Waveguides are integrated into the chip by filling voids left by the moulding with a high refractive index optical grade epoxy. The optical structure layout is shown in Figure 2.7 and comprises integrate micro-lenses to focus the excitation light and collect scattered light. The chip was used to discriminate between bead sizes and also between platelets and red blood cells by measuring the extent of forward scattered light. Beads and cells were inertially focussed in the square cross section, 55 µm by 30 µm microfluidic channel and inertial focussing was shown to decrease signal variability.

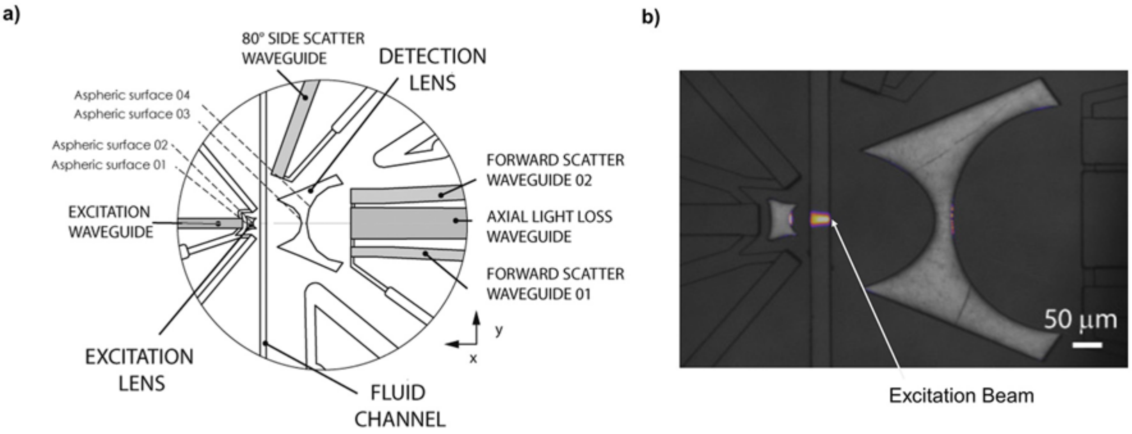

Figure 2.7: (a) Optical layout for a polymer based microflow cytometer using integrated optics and inertial focussing. (b) Excitation beam revealed by fluorescent solution. Images taken from [25]

The main criticism of inertial focussing as a microfluidic particle positioning technique is the requirement for long channel lengths in the region of 1-40 cm which can be hard to fit onto microchips. The channel length can be minimised however by choosing the optimum particle diameter to channel cross section ratio. The long channel lengths combined with high flow rates required lead to a large pressure drop across the microfluidic channel and so the fluidics and channel sealing techniques must be engineered to withstand high pressures.

2.6 Conclusion

Of all the methods described those which are simple to fabricate are especially appealing as they will reduce fabrication time and ultimately cost which are both critical in mass production. It is also important to consider the complexity required to operate the flow cytometer. Based on these criteria inertial focussing shows the best suitability for combination with integrated optics. The straight microfluidic channels with a square or rectangular cross section can be fabricated using conventional mass production techniques such as photolithography and deep reactive ion etching. Control of the focussing is simply via the flow rate of a single fluidic input. Another significant advantage of the technique is the even staggered spacing with which particles align which prevents coincident signals caused by multiple beads passing through the beam at the same time. A straight microfluidic channel with a rectangular cross section with a height:width aspect ratio of at least 3:2 would inertially focus beads into two equilibrium positions centred on the long faces of the channel. Waveguides could be positioned on the same plane as the equilibrium positions allowing excitation of the flowing beads and collection of light from the microfluidic channel. The design of such a channel to inertially focus immunoassay beads in the proposed microflow cytometer device is discussed in Chapters 3 and 4.

CHAPTER 3

Optical light path design

3.1 Introduction

Integrated optical waveguides are an ideal system for control of the light path in a microflow cytometer. As discussed in Chapter 1, they are compact, intrinsically aligned with the microfluidics during fabrication and can be produced in conjunction with microfluidics by widely available mass production techniques used in the microelectronics industry. Fine control of the behaviour of light can also be achieved with optimised waveguide structure designs. Advanced integrated optical structures such as kinoform microlenses [21] and MMI devices [20] can also be included for light focussing and collection.

The microflow cytometer developed in this work was designed to measure the fluorescence from beads used in an immunoassay. The intrinsically aligned waveguide structures were expected to also be a viable system for the collection of light from the microfluidic channel. This chapter describes the design of the optical light path in the microflow cytometer using waveguide structures suitable for excitation of fluorescence from flowing beads in a microfluidic channel and also collection of light from that microfluidic channel. A basic waveguide structure and layout were first chosen. Then the refractive index of the material system to be used were determined from fabricated samples. These values were then used for optimised design of the waveguide dimensions using a commercially available simulation package, BeamPROP v8.1 (Rsoft, Synopsys , USA) which uses the beam propagation method (BPM) [58]. The waveguide dimensions were designed primarily around the need for efficient input and output coupling and single mode or multimode behaviour. The insertion loss of a microfluidic channel between input and output waveguides was simulated in order to estimate the dimensional limitations for design of the microfluidic channel. The interaction of flowing beads with a beam was also simulated in order to estimate the signal that may be measured for transmission based detection of flowing beads.

3.2 Basic waveguide structure and layout

A basic waveguide structure and layout were first chosen, upon which further optimisation could take place. The chosen waveguide structure was that of a buried channel (strip) waveguide structure, shown in Figure 3.1, which consists of a rectangular cross section core on top of a substrate completely buried in cladding material. Using this type of structure with a cladding and substrate of matching refractive index produces a fundamental mode profile with 2 axes of symmetry. This has the advantage of launching a free-space beam with a symmetrical cross section and also improves the input and output coupling efficiency as the symmetry more closely matches the circular mode profile of single mode optical fibres [59].

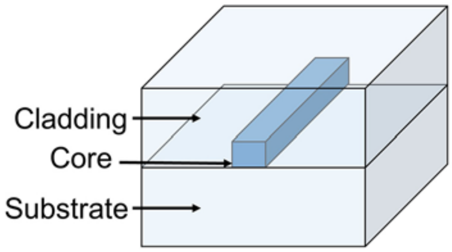

Figure 3.1: Channel (strip) waveguide structure.

A simple waveguide layout, shown in Figure 3.2, was chosen and consisted of an input (excitation) waveguide to direct light to the microfluidic channel and launch a free-space beam, and an output (collection) waveguide, axially aligned with the input waveguide to collect light from the microfluidic channel on the other side. The straight rectangular cross section microfluidic channels suitable for inertial focussing, proposed in Chapter 2, have two equilibrium positions centred on the long faces of channel cross section close to the wall. The waveguide layer is positioned halfway up the long face of the microfluidic channel so that the launched beam can illuminate both equilibrium positions.

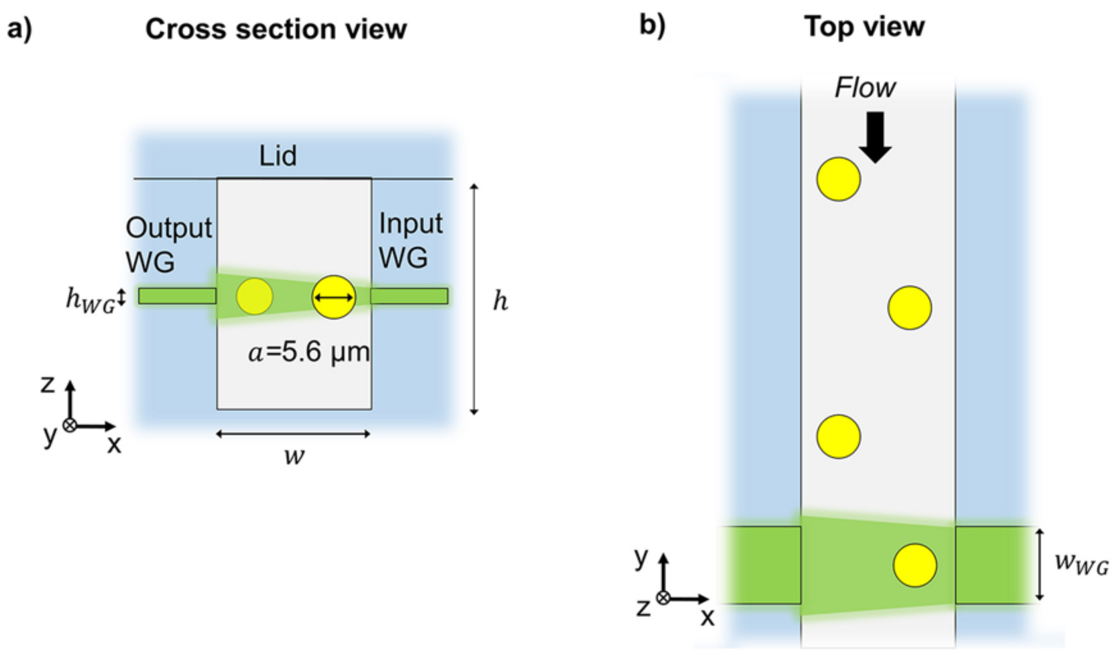

Figure 3.2: Schematic of fundamental waveguide layout relative to the microfluidic channel and inertially focussed beads, and the expected launched free-space beam. Showing (a) cross section view and (b) top view.

More complex waveguide layouts were not used as it was important to establish a simple system first which was mainly concerned with efficient fibre input coupling. The axially aligned input and output waveguides were designed to allow detection of flowing beads through measuring the change in optical power transmitted from the input waveguide to the output waveguide. It was envisaged that future designs with offset, angled output waveguides could be used to collect light from scatter and fluorescence.

3.3 Refractive index measurement of optical materials

A monolithic silica based system was chosen for good optical performance as discussed in Chapter 1. The selected waveguide material system used a bulk SiO_2 substrate, a core of GeO_2 (germania) doped SiO_2 and a cladding of SiO_2. These materials were chosen partly as they were expected to show similar etch rates reducing undercutting, and notches which can lead to distortions in the shape of an etched microfluidic channel and the end facets of waveguides. In addition they can produce waveguides with refractive indices similar to that of commercially available optical fibres improving coupling efficiency [60]. The refractive index difference between the core and the cladding is determined by the molar percentage of germania in the core material. A higher molar percentage of germania increases the core refractive index and thus the refractive index difference with the cladding [61]. The refractive index difference was chosen to be large enough so that the majority of the optical power of a propagating mode is contained within the waveguide core allowing fine control of the modal spot size by adjustment of the waveguide dimensions. The refractive index of test samples of the materials at the bead immunoassay excitation wavelengths of 532 nm and ~633 nm were first measured in order to obtain values to use in the simulation of the waveguides.

Ellipsometry was used to measure the refractive indices of the optical materials. This none contact, optically based technique can measure the refractive index of a transparent film or bulk substrate across a range of wavelengths as well as measure the thickness of a film [62]. Test samples were prepared for each optical layer using the fabrication protocols described in Chapter 4. The substrate refractive index was measured from bulk fused silica substrates with no deposited film. For the core refractive index, 2 µm thick germania:silica films deposited on bulk silica substrates by magnetron sputtering were measured. For the cladding, 18 µm thick films of PECVD SiO_2 on bulk silica were measured. The ellipsometer used was a Woollam M-2000 spectroscopic ellipsometer (JA Woollam Co., USA). The ellipsometry data was used to obtain the coefficients for the Cauchy dispersion equation which describes the relationship between refractive index and wavelength for the material [63].

$$n(\lambda) = A + \frac{B}{\lambda^2} + \frac{C}{\lambda^4} \qquad 3.1$$

Here n is refractive index, A, $B$and C are coefficients and λ is wavelength in micrometres. The dispersion curves calculated for each material are shown in Figure 3.3 and the Cauchy coefficients and calculated refractive indices are summarised in Table 3.1.

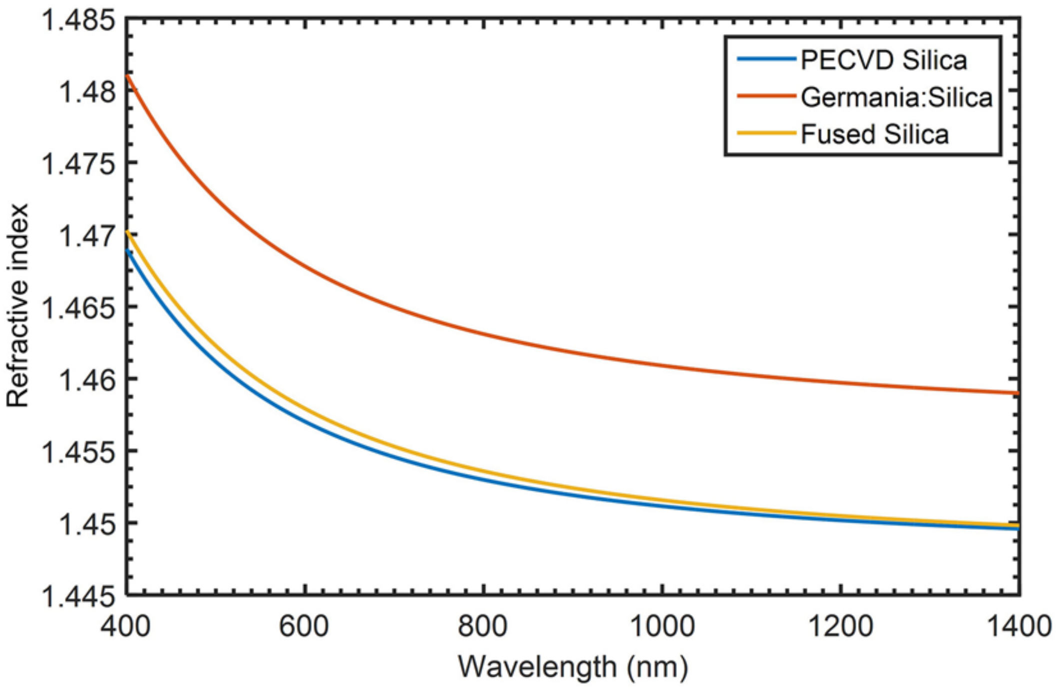

Figure 3.3 Cauchy dispersion curves calculated from ellipsometry data for PECVD silica film on fused silica substrate, germania:silica film on fused silica substrate and fused silica substrate alone.

To confirm the ellipsometry measurements, the refractive index of the materials were measured by another technique known as prism coupling which was capable of measurement at a wavelength of 633 nm [64]. These measurements are also included in Table 3.1 for comparison.

Table 3.1: Ellipsometry data including Cauchy coefficients and calculated refractive index at wavelengths of 532 nm and 633 nm for test samples of each optical material. The refractive indices measured by prism coupling are also shown for comparison.

	Ellipsometry measurements					**Prism coupling measurements**
	Cauchy Coefficients			**Refractive index**		**Refractive index**
Material	**A**	**B**	**C**	**532 nm**	**633 nm**	**633 nm**
germania:silica	1.457	3.94×10^{-3}	-3.41×10^{-5}	1.471±0.001	1.467±0.001	1.469±0.0007
PECVD silica	1.448	3.02×10^{-3}	1.36×10^{-4}	1.460±0.001	1.456±0.001	1.457±0.0001
fused silica	1.448	3.58×10^{-3}	-5.34×10^{-6}	1.461±0.001	1.457±0.001	1.457±0.0001

The refractive index calculated by ellipsometry for the fused silica substrate matches the refractive index from the prism coupling at 633 nm. The refractive index at a wavelength of 633 nm for the Germania:Silica and the PECVD silica are within 0.01 % of those measured by prism coupling. The final indices used for the simulations were taken from the ellipsometry data for consistency. As the PECVD silica index was very similar to the fused silica, the fused silica index was used as the cladding index in the simulations. The indices at both wavelengths used for the simulations were cladding indices of $n_{s532nm} = 1.461 \pm 0.001$ and $n_{s633nm} = 1.457 \pm 0.001$ and core indices of

$n_{c532nm} = 1.471 \pm 0.001$ and $n_{c633nm} = 1.467 \pm 0.001$. The refractive index difference, Δn, used for the simulation was calculated as $\Delta n = n_c - n_s = 0.010$ for both wavelengths.

3.4 Beam propagation method background

The beam propagation method is the numerical method used by the BeamPROP software to simulate wave propagation in waveguide structures. Detailed explanations of the technique are available in the literature in Marz [58]. The BPM is less computationally intensive than finite difference time domain methods due to the approximations made.

The algorithm works by sequentially calculating the field distribution of a beam at discrete slices along the propagation direction in a waveguide [65]. The calculation must start with an input field distribution in the plane perpendicular to propagation. A beam with this field distribution is then propagated a short distance using classical diffraction formulas through a virtual homogenous medium with a refractive index which is the average of the waveguide core and cladding refractive indices. The diffracted beam field distribution is then transmitted through a phase and amplitude mask which is based on the refractive index profile of the waveguide. The mask shifts the phase distribution and amplitude distribution of the beam to produce the beam field distribution at that propagation distance along the waveguide. The diffraction calculation steps and mask transmission steps are repeated sequentially for each slice along the length of the waveguide separated by a short distance in the order of microns.

3.5 Conditions for single mode operation and multimode operation

For a channel waveguide system of fixed refractive index contrast, increasing the cross sectional dimensions increases the number of modes which can propagate. Single mode waveguides offer advantages for use in a microflow cytometer. In single mode waveguides the size of the modal intensity distribution, known as the mode profile is well controlled by the waveguide dimensions allowing fine control over the dimensions of a launched free-space beam. As there is only one mode propagating there is no intermodal interference and so the intensity distribution of a launched free-space beam does not depend on the input waveguide length. Single mode waveguides are also efficient to couple light in and out of by butt-coupling of fibres. The fundamental mode has a field intensity distribution which approximates a Gaussian function, and this is well matched to the shape of the mode profile for a single mode fibre. Multimode waveguides can be useful in a microflow cytometer but have limitations. The intensity distribution of a free-space beam launched from a multimode waveguide depends on the length of that waveguide as the multiple modes propagating at different velocities constructively and destructively interfere along the length of the waveguide. Therefore the length of the multimode waveguide must be tightly controlled to produce a beam of predictable intensity distribution and dimensions. If the length is well controlled however the larger cross sectional dimensions of multimode waveguides can be used to launch a larger diameter free-space beam for illuminating larger particles. Multimode waveguides with higher numerical apertures are also more efficient at collecting light from point sources than single mode waveguides with lower numerical apertures. The numerical aperture of a waveguide is defined by the refractive index contrast of the material system and is a measure of the acceptance angle of a waveguide through the relationship

$$NA = n_i sin\theta_a = \sqrt{n_c^2 - n_s^2} \qquad 3.2$$

where n_i is the refractive index of the propagation medium of the incident light, θ_a is the maximum ½ acceptance angle of the waveguide. A waveguide with a higher NA will therefore accept more light from a point source than a lower NA waveguide as a wider range of angles are collected. Even when a single mode and multimode waveguide have the same NA, the wider multimode mode waveguide will collect more light from a point source the same distance away due to a greater spacial overlap of the emanating light rays.

Once the refractive indices of the waveguide materials had been measured, simulations could be performed using the BeamPROP software to determine the waveguide dimensions for single mode operation and multimode operation. The structure of the simulated channel waveguide is shown in Figure 3.4. The waveguide height, h_{WG}, was set to 2 µm as a likely starting point for single mode operation in the Z direction, based on previous work by Dr Hamish Hunt using the same materials but with a slightly higher refractive index difference [66]. In the simulation the waveguide width, w_{WG}, was varied between 1-11 µm and the effective refractive indices for the first 6 modes were monitored. The effective refractive index, n_{eff}, quantifies the change in wavenumber compared to free-space for a given mode propagating in a waveguide. For a mode to be guided it must have an effective index above that of the cladding index. The simulations were performed at wavelengths of 532 nm and 633 nm which are the excitation wavelengths used in the luminex bead based immunoassay.

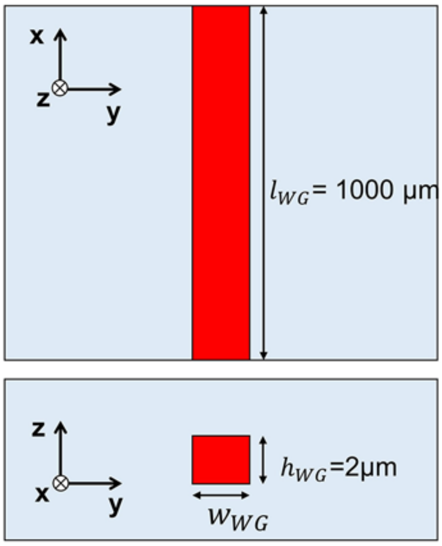

Figure 3.4: Schematic of the waveguide structure used in the simulations showing the core in red and the cladding in blue.

The mode dispersion plot in Figure 3.5 shows the calculated effective refractive index at a wavelength 532 nm for the first six modes as waveguide width increases. The width at which the waveguide begins to guide the first order mode (M_{10}), known as the cut-off width for single mode behaviour, is 2.2 µm.

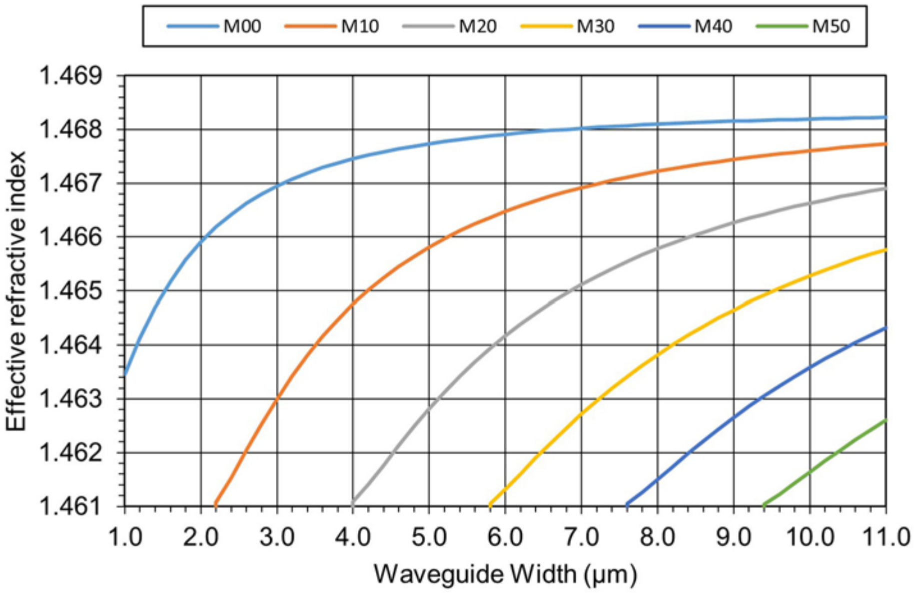

Figure 3.5: Mode dispersion plot showing the effective refractive index at a wavelength 532 nm for the first six modes (MX0) as waveguide width varies and waveguide height remains at 2 µm for TE polarisation.

The mode dispersion plot in Figure 3.6 shows that at a wavelength of 633 nm the cut-off width for single mode behaviour is 2.8 µm. For both wavelengths simulated, the light polarisation did not significantly change the calculated effective indices and so only the results for simulations with transverse electric field (TE) polarisation have been presented.

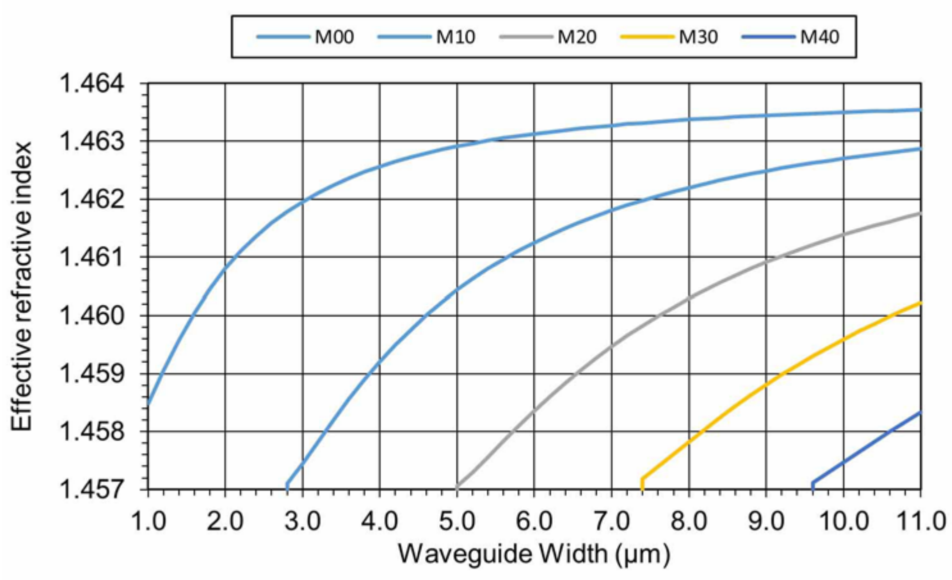

Figure 3.6: Mode dispersion plot showing the effective refractive index at a wavelength 633 nm for the first six modes (MX0) as waveguide width varies and waveguide height remains at 2 μm for TE polarisation.

These simulations were used as a guide to predict the modal behaviour of the fabricated waveguides. The photolithographic mask design used to fabricate the waveguides for the microflow cytometer consisted of arrays of 42, 100 mm long rectangles of widths increasing from 1.4 to 10 μm in 0.2 μm increments. This mask allowed the optical performance of different waveguide widths to be tested experimentally in terms of the number of modes supported, propagation loss, and the dimensions of the free space beam launched by the waveguide. The simulations confirmed that the waveguide layer must have a height of less than 2.2 μm to ensure single mode operation for both wavelengths on the same chip. Practically this was chosen to be 2.0 μm to allow for fabrication error. The simulations suggested that a waveguide with a width of 2.0 μm and a height of 2.0 μm would be single mode for both wavelengths.

3.6 Effective index method

The effective index method is a method for approximately calculating the effective index of a guided mode using the cross sectional dimensions of a channel or rib waveguide and can be used to verify simulation results. The method works by separating a 2D waveguide structure, shown in Figure 3.7(a) into two, 1D slab waveguides with waveguide I in the YZ plane (Figure 3.7(b)) and waveguide II in the XY plane (Figure 3.7(c)).

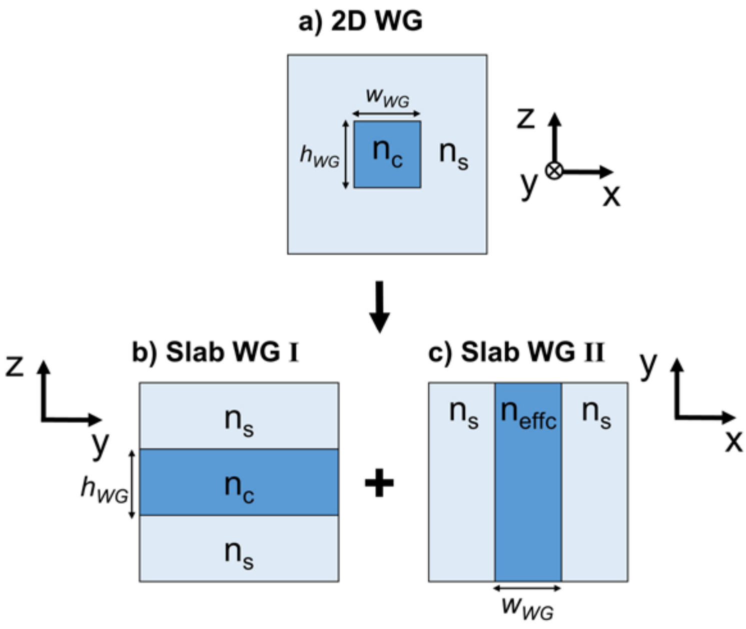

Figure 3.7: The effective index method

First the normalised frequency, v is calculated using the following equation.

$$v = \frac{2\pi}{\lambda} \times h_{WG}\sqrt{(n_c^2 - n_s^2)} \qquad 3.3$$

The normalised frequency is used to ascertain the normalised index, b, from a normalised dispersion curve which are plotted from normalised dispersion equations available in common integrated optics textbooks [67]. The dispersion curve used depends on the mode number,p and whether polarisation is TE or TM. The normalised index is then inserted into the following equation to calculate the modal effective index in the Y direction n_{effc} for waveguide II.

$$n_{effc} = \sqrt{b(n_c^2 - n_s^2) + n_c} \qquad 3.4$$

The effective index of the mode in the 2D structure is calculated by repeating the above procedure but with n_{effc} substituted for n_c and w_{WG} substituted for h_{WG}.

The effective index method confirmed the effective index calculations performed in the simulation software. For example light at an input wavelength of 532 nm propagating in a waveguide of dimensions $w_{WG} \times h_{WG} = 10 \times 2$ μm^2 yielded an effective index of 1.4681 which matched the simulation results to four decimal places.

3.7 Coupling efficiency

Efficient coupling into integrated optical waveguides is important for sensitive detection in a microflow cytometer. The coupling method for launching light into a waveguide should ideally couple as much of the total optical power into the guided modes of the waveguide as possible. Any stray light which is not coupled into the waveguide will propagate in the substrate and can contribute to the background signal. Light must also be efficiently coupled out of a waveguide to maintain a high signal for measurement with detectors.

To couple light into and out of integrated optical waveguides there are two main techniques. Free space coupling or end fire coupling uses an objective lens to focus light into or collect light from a polished waveguide end facet. This method can achieve high coupling efficiencies approaching 100% [67] however the use of large lenses positioned close to the device can restrict the number of optical connections to a device. Free space coupling is also prone to variation in coupling efficiency due to movement of the lenses and waveguides relative to one another. A more compact solution is using a cleaved optical fibre to launch light into or collect light from the end facet of a waveguide. In this method, known as butt-coupling, the optical fibre is axially aligned with the waveguide with the end facets positioned microns apart in order to minimise the divergence of light across the gap. Once aligned for optimal coupling optical fibres can be glued in place with refractive index matching glue allowing a robust optical connection to an integrated chip. The sub-millimetre diameter of optical fibres allow many optical connections to a chip exploiting the dense circuitry capabilities of integrated optics.

The coupling efficiency for butt-coupling of a single mode optical fibre to single mode waveguides of varying widths were simulated in the same channel waveguide structure shown in Figure 3.4. Input coupling was simulated however the calculated efficiencies can also be considered to be the same for output coupling. The waveguide height was set at 2 µm as this was the film thickness that would be used to ensure single mode operation at wavelengths of 532 nm and 633 nm. The waveguide width was varied between 1 µm and 3.5 µm and the coupling efficiency was calculated as the overlap integral between the electric field intensity distribution of the single mode optical fibre input and the electric field intensity distribution at the output of the 1000 µm long waveguide. The spotsizes, ω, defined as the full width of the mode profile at $1/e^2$ maximum intensity, for the commonly available single mode fibres used in the simulation input fields were taken from manufacturers data sheets and were 3.5 µm for 460HP [59] and 4.5 µm for SM600 [68]. Commercial fibres are also available which are single moded at both wavelengths [69]. The simulation used no air gap between the fibre and waveguide to calculate the best possible coupling.

Figure 3.8 shows the calculated coupling efficiencies for both wavelengths. The coupling efficiency at a wavelength of 532 nm is higher than the coupling efficiency at a wavelength of 633 nm for all waveguide widths because the waveguide height is fixed at 2 µm and so there is less spatial overlap between the fibre and waveguide mode in the vertical direction at a wavelength of 633 nm. At 532 nm the maximum coupling efficiency is 0.94 for a waveguide of width 2.9 µm and at 633 nm the maximum coupling efficiency is 0.89 for a waveguide of width 3.2 µm. In the simulations, the centralised launch field excites only the fundamental mode however if waveguides of these widths were actually used there is a possibility of exciting the antisymmetric 1st order mode with an off centre fibre. As discussed previously a 2 µm wide waveguide would ensure single mode operation and still shows a high coupling efficiency at 0.90 and 0.84 for wavelengths of 532 nm and 633 nm respectively.

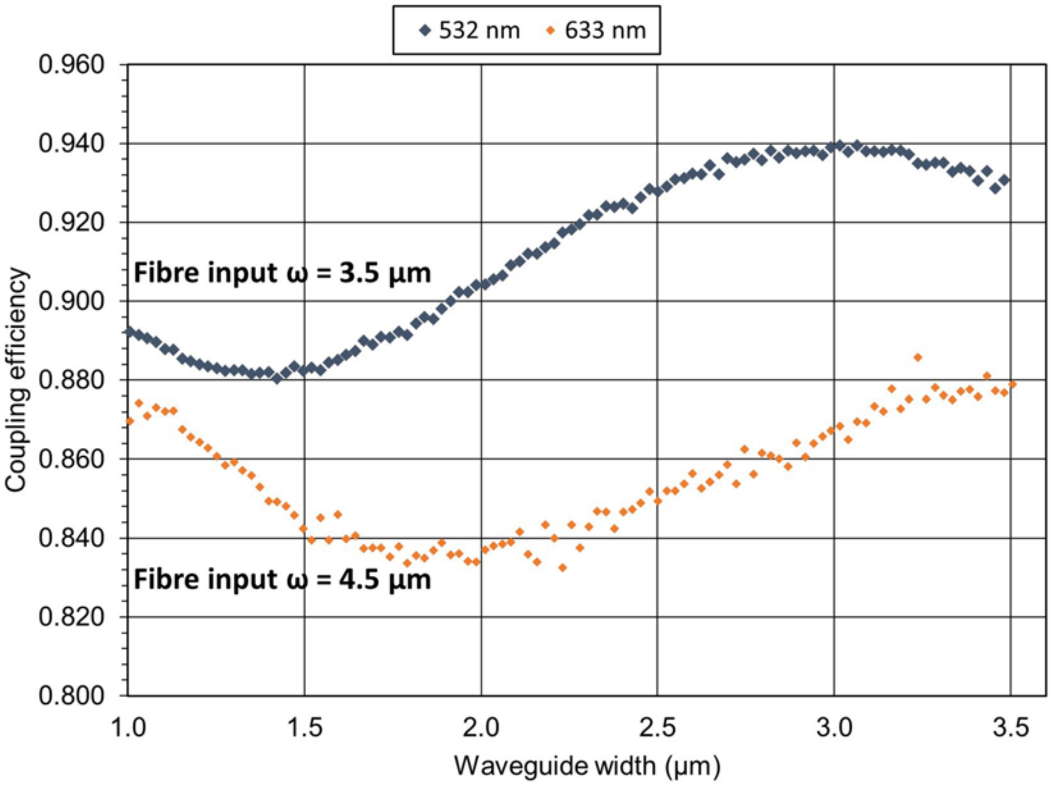

Figure 3.8: Coupling efficiency for coupling of a single mode fibre at wavelength of 532 nm and 633 nm into a waveguide of 2 µm height and varying width.

The coupling efficiency can also be calculated approximately by an overlap integral of two Gaussian distributions of matching widths to the spotsizes of the input fibre and waveguide fundamental modes respectively [67]. The overlap integral for two Gaussian distributions is calculated by the following.

$$\eta = \frac{\left|\int E_i^* E_o \, dA\right|^2}{\int |E_i|^2 \, dA \int |E_o|^2 \, dA} \qquad 3.5$$

Here η is the coupling efficiency and E_i and E_o are Gaussian distributions representing the electric field distributions of the fundamental modes of the input fibre and waveguide respectively. This overlap integral was performed numerically in Matlab™ for the coupling of a single mode fibre to a 2×2 µm^2 at both wavelengths. The spotsizes used for the fibres were those stated above and the spotsizes of the fundamental mode for the waveguide were 2.41 µm and 2.70 µm for wavelengths of 532 nm and 633 nm respectively. The coupling efficiencies calculated by the overlap integral were $\eta_{532\mathrm{nm}} = 0.93$ and $\eta_{633\mathrm{nm}} = 0.88$. These calculated coupling efficiencies are 3-5% higher than those calculated by the BeamPROP simulations which is to be expected as the real mode profiles are not truly Gaussian. This calculation confirms that the simulation results are reasonable.

3.8 Mode profile of single mode waveguide

The mode profiles for the 2 µm wide, 2 µm high waveguide were simulated using the inbuilt mode-solver in BeamPROP at wavelengths of 532 nm and 633 nm in order to calculate the spotsize, ω in the Y and Z direction and analyse the intensity distribution relative to the waveguide structure. The spotsize was defined as the full width of the mode profile at 1/e^2 maximum intensity. Figure 3.9 confirms that the square waveguide cross section produces mode profiles with 2nd order rotational symmetry and with a Gaussian-like intensity distribution characteristic of the fundamental mode. The spotsizes were the same in Y and Z and were 2.41 µm and 2.70 µm for wavelengths of 532 nm and 633 nm respectively. These values are summarised in Table 3.2. The spotsizes presented are for TE light as changing polarisation did not change the spotsize.

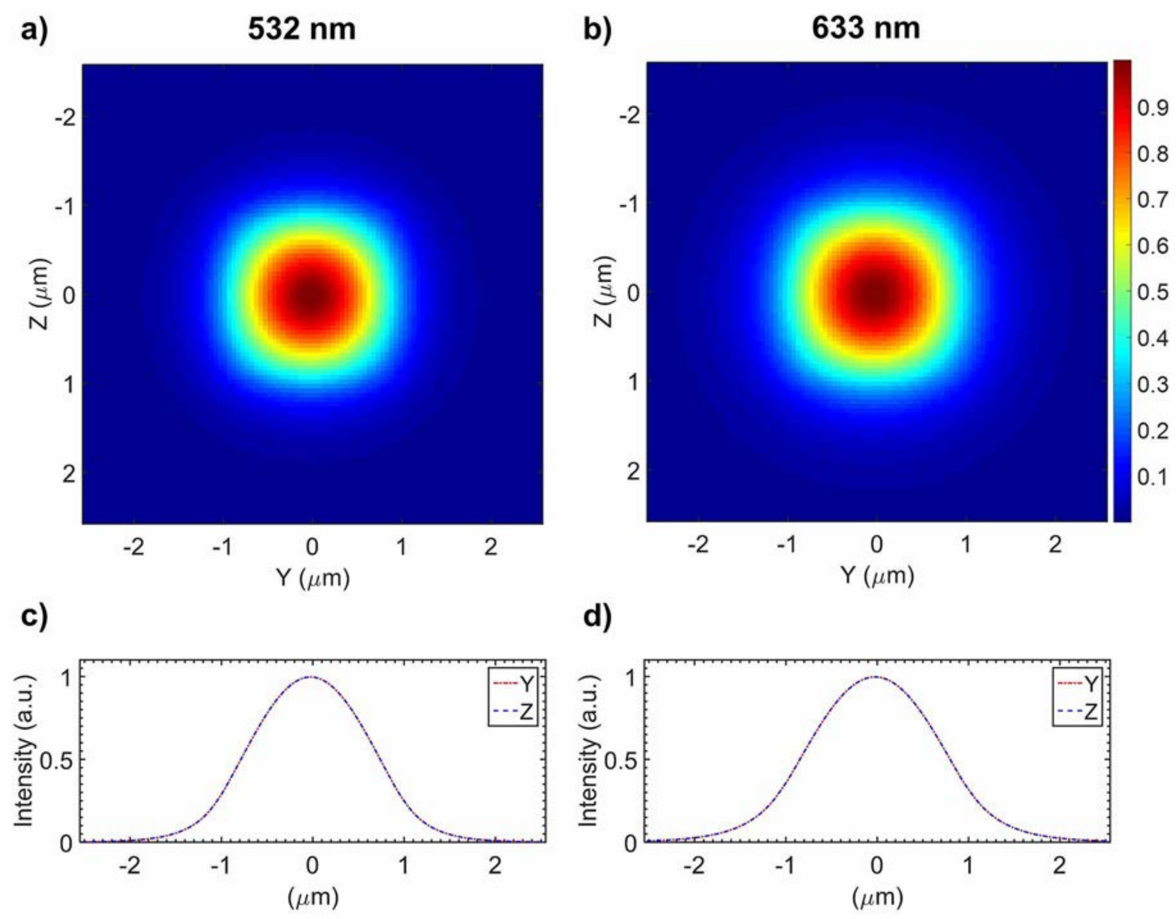

Figure 3.9: Mode profiles for a 2 µm wide, 2 µm high waveguide at wavelengths of (a) 532 nm and (b) 633 nm. The intensity profiles through the intensity maxima in Y and Z are shown underneath for wavelengths of (c) 532 nm and (d) 633 nm.

Table 3.2: Spotsize (full width 1/e^2 maximum intensity) of fundamental mode in Y and Z for wavelengths of 532 nm and 633 nm

532 nm		**633 nm**	
ω_y	ω_z	ω_y	ω_z
2.41 µm	2.41 µm	2.70 µm	2.70 µm

The simulated mode profiles confirm that the majority of the optical power is confined to the core of the waveguide.

3.9 Insertion loss of microfluidic channel

The optical loss incurred by inserting a microfluidic channel between the collection and excitation waveguide was simulated in order to inform the design of the microfluidic channel width. For transmission based detection of flowing beads it was desirable to have as high a coupling efficiency as possible. By ensuring as much light as possible is coupled back into the output waveguide the output signal is maximised and the stray light propagating in the substrate is minimised. For transmission based detection of flowing beads a high coupling efficiency provides a high baseline transmission against which to measure the negative peak caused by a particle interrupting the beam. The signal to noise ratio (SNR) for transmission based detection of beads is defined as

$$SNR = \Delta T / \sigma_B \tag{3.6}$$

where σ_B is the standard deviation of the baseline signal and ΔT is the change in transmission compared to the baseline transmission, T_B, ($\Delta T = T_B - T$, where T is the transmission peak amplitude). If σ_B is kept constant by minimising vibration and electrical noise then a high coupling efficiency ensures a high baseline transmission signal which allows for a greater negative ΔT and thus a high signal to noise ratio allowing positive identification of a bead signal.

A 3D simulation was performed of an input waveguide transmitting light at a wavelength of 532 nm across a microfluidic channel filled with water ($n_{532nm} = 1.334$ $n_{633nm} = 1.332$) to an identical output waveguide. The width of the microfluidic channel was increased and the coupling efficiency which is the normalised power transmitted from the excitation waveguide to the collection waveguide was determined.

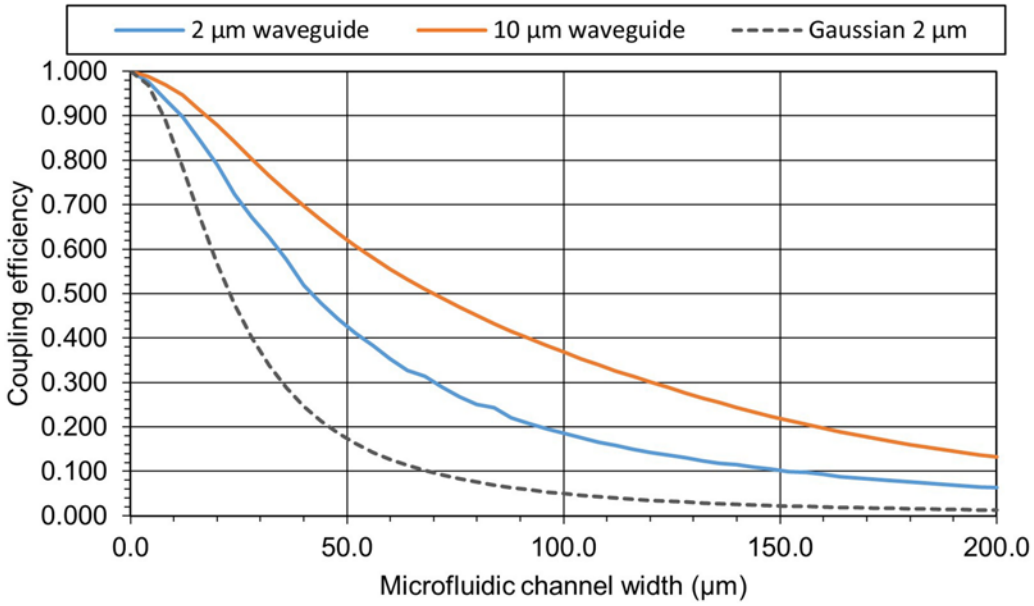

Figure 3.10: Coupling efficiency between the input and output waveguides of 2 µm height separated by a water filled microfluidic channel of varying width for 2 µm and 10 µm waveguide widths. With input light at a wavelength of 532 nm. Graph also shows the coupling efficiency for a Gaussian beam with the same spotsize as a 2 µm waveguide.

Figure 3.10 shows that increasing the microfluidic channel width reduces the coupling efficiency. This is due to diffraction of the beam in the water causing it to diverge in the Y and Z direction so that less light to enters the output waveguide. The 10 µm width waveguide shows better coupling efficiency than the 2 µm width waveguide for all channel widths. This is because the wider waveguide has a larger spotsize and thus a lower rate of divergence compared to the smaller spotsize from the narrower waveguide.

For both waveguide widths, a microfluidic channel width below 40 µm has a coupling efficiency greater than 0.5 which was considered to be good for transmission based detection of flowing beads. For channels wider than 40 µm, focussing structures such as multimode interference (MMI) devices [20] and kinoform microlenses [21] could be included to reduce the divergence of the beam and increase coupling efficiency. The microfluidic channel design section in Chapter 4 takes into consideration these results for the choice of microfluidic channel dimensions. The channel chosen for in the microfluidic design section had a design width of 20 µm which was simulated to have a high coupling efficiency of 0.79 for a 2 µm wide waveguide and 0.88 for a 10 µm wide waveguide. The coupling efficiencies correspond to coupling losses of 1.0 dB and 0.6 dB for waveguides of 2 µm width and 10 µm width respectively.

Figure 3.10 also shows the analytically calculated coupling efficiency, η across the microfluidic channel for a Gaussian beam with an identical launch spotsize ($\omega_0 = 2.41$ µm) to a 2 µm width waveguide calculated using the following equation [70], [71].

$$\eta = \left(1 + \left(\frac{w\lambda_0}{2\pi n_l \left(\frac{\omega_0}{2}\right)^2}\right)^2\right)^{-1} \qquad 3.7$$

Here n_l is the refractive index of the medium the beam is propagating through which in this case is water ($n_l = 1.334$). The analytically predicted coupling efficiency across a 20 µm channel for a 2 µm waveguide follows the shape of the equivalent simulation results but the coupling efficiency is lower at 0.57 (2.4 dB). This difference is due to the simulation mode profiles not being Gaussian.

3.10 Simulation of transmission signal of passing bead

The axially aligned input and output waveguide layout is designed to allow detection of flowing beads by measuring the change in optical power transmitted from the input waveguide to the output waveguide as beads flow through the beam. A simulation was performed to measure the change in transmission due to a bead flowing through a beam coupling an input and output waveguide. The results of the simulation would be used to understand how a flowing bead will interact with the beam and give a quantitative estimate for amplitude of the transmission signal change that might be measured in the real device.

As a full 3D simulation would be too computationally intensive, the 3D channel waveguide structures were converted into equivalent 2D slab waveguides by substituting the core refractive index with the effective index of the fundamental mode for the equivalent width 3D channel waveguide. The input and output waveguides used in the simulation were both single mode and so the n_{eff} for the 3D, 2 µm wide by 2 µm high waveguide was used in this simulation so $n_{eff} = 1.466$. Single mode waveguides were used as opposed to multimode waveguides to simplify the bead interaction with the beam. Figure 3.11 shows the structural layout used in the simulation. A 2 µm wide, single mode input waveguide transmits a beam across a 20 µm wide microfluidic channel to a 2 µm wide, single mode output waveguide. A 5.6 µm diameter polystyrene bead ($n_{532\text{nm}} = 1.598$), was translated in the Y direction across the beam, 5 µm from the channel wall at the estimated near side and far side equilibrium positions.

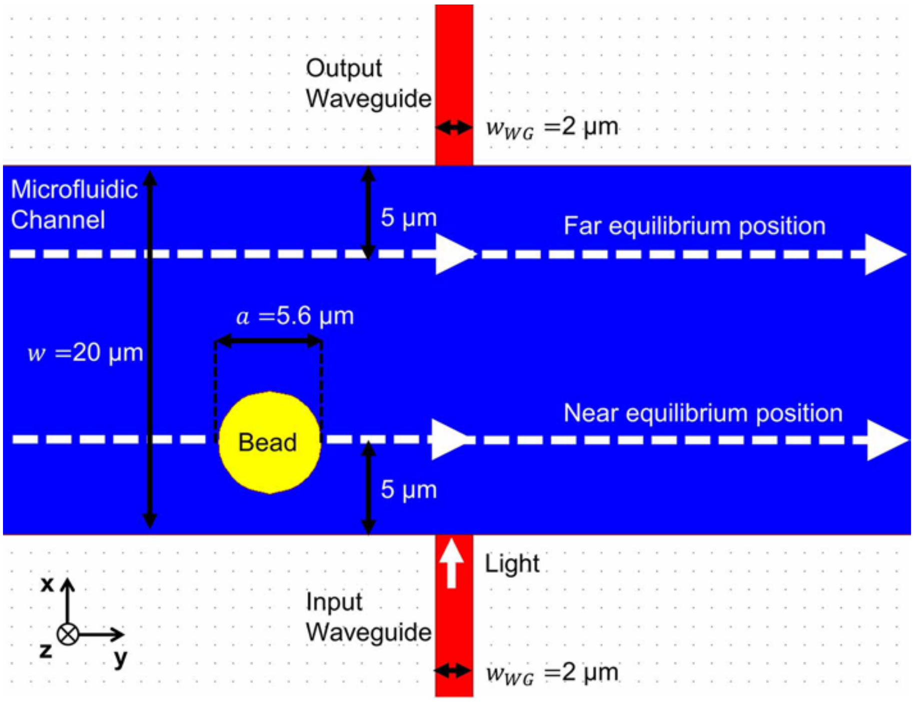

Figure 3.11: Schematic of the optical structure layout for simulation of the transmission signal as a bead flows through the beam crossing the microfluidic channel.

Figure 3.12 shows the overlaid transmission signals for a bead passing on the near and far equilibrium positions. The X axis scale of Figure 3.12 shows the bead displacement in the simulation Y direction from the central axis of the input waveguide. Figure 3.13 shows the electric field distribution for the beam crossing the channel for bead Y displacements which produce the minimum and maximum transmission for both the near and far equilibrium positions.

For a bead passing on the near side equilibrium position to the input waveguide, the transmission signal decreases as the bead enters the beam and deflects the beam away from the output waveguide reaching a minima of 12.0% at Y=-2.2 µm. The deflection, shown in Figure 3.13(a) is caused by refraction of the beam as it passes through the bulk of the circle representing the bead which has a higher refractive index ($n_{532\text{nm}} = 1.598$) than the surrounding water ($n_{532\text{nm}} = 1.334$). As the bead approaches the central axis of the input waveguide the transmission increases to a maximum of 102.6% at Y=0. The transmission is increased slightly from the baseline transmission when no bead is interacting with the beam because the higher refractive index, circle representing the bead acts as a lens to focus more power into the output waveguide as shown in Figure 3.13(b). As the bead moves away from the central axis of the input waveguide the transmission signal decreases in a manner symmetrical to when the bead entered the beam reaching a minima of 12.0% transmission at Y=2.2 µm. The transmission signal for a bead passing at the equilibrium position on the far side of the channel to the input waveguide shows a transmission signal which almost identically matches the transmission signal for a bead passing at the near side equilibrium position. For a bead passing at the far side the two transmission minima are 12.0% at Y displacements of -2.2 µm and 2.2 µm and the maximum transmission at Y=0 is 102.7%. As with the passage on the near side equilibrium position, on the far side the bead acts to deflect (Figure 3.13(a) and (c)) and focus (Figure 3.13(b) and (d)) the beam to reduce and increase transmission respectively.

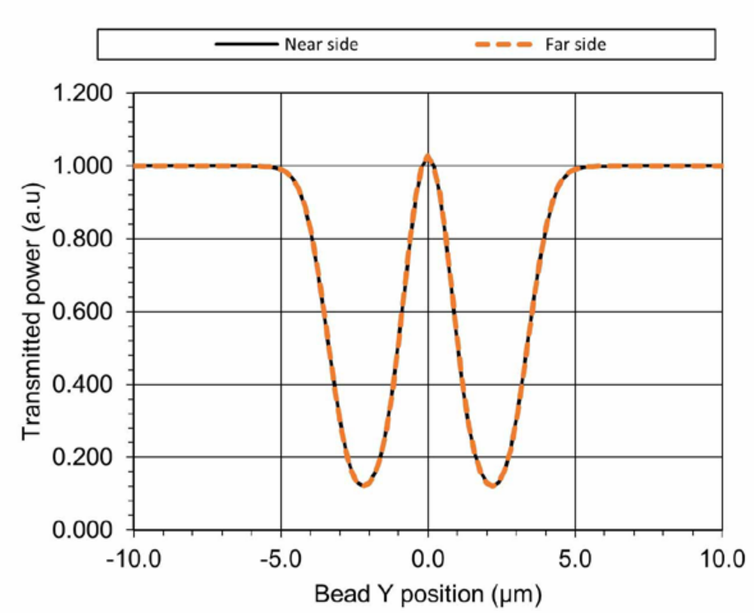

Figure 3.12: Simulation results showing power measured at the collection waveguide output as a bead is translated in the Y direction through the beam. The Y position is relative to the input waveguide central axis. The signals for beads at the near side and far side equilibrium positions relative to the input waveguide are overlaid.

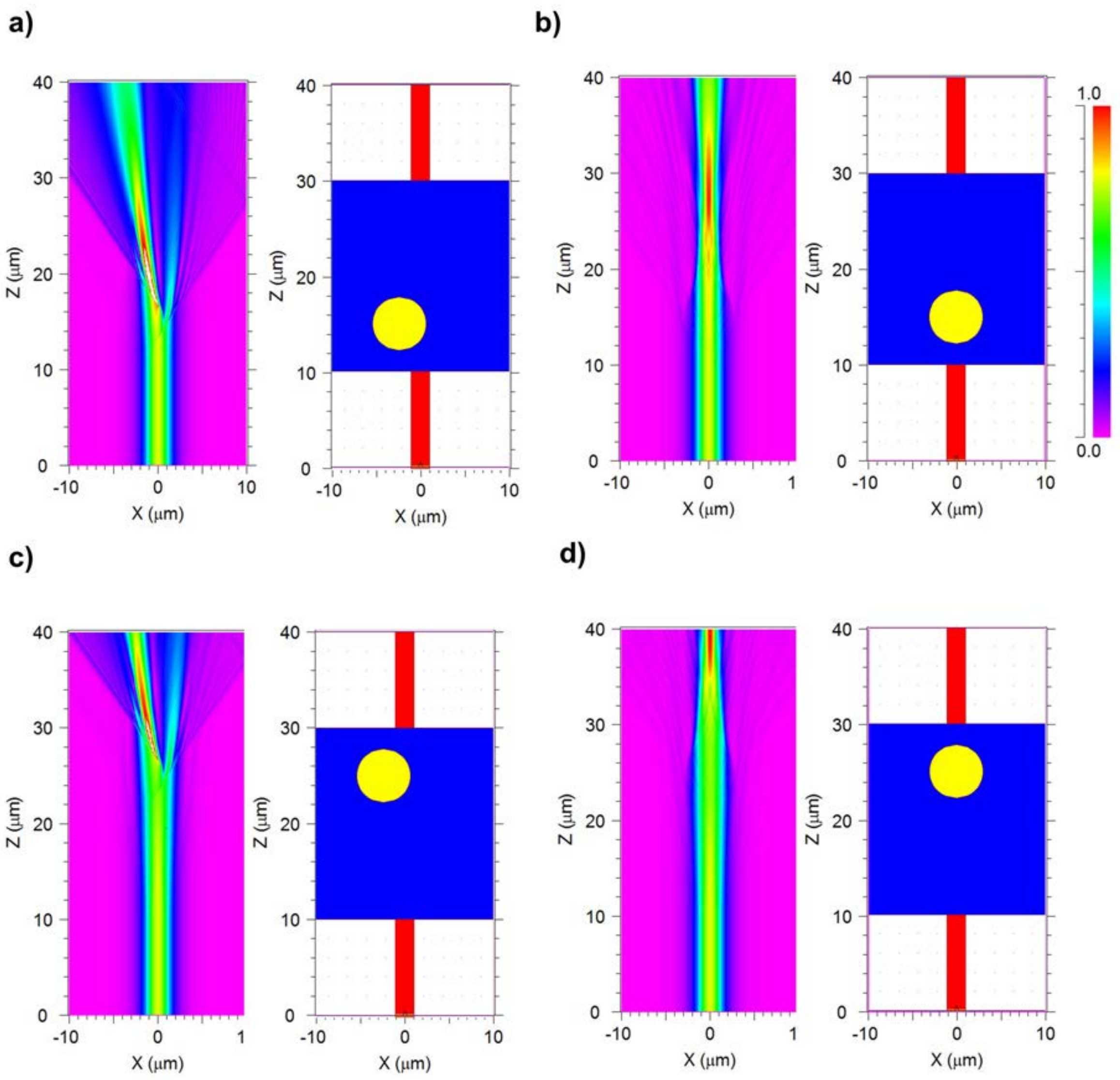

Figure 3.13: Electric field distribution for a beam crossing the microfluidic channel when the bead is at the (a) near side and offset by -2.2 µm, (b) nearside and axially aligned, (c) far side and offset by -2.2 µm and (d) far side and axially aligned.

The transmission minima for beads passing at both equilibrium positons corresponds to an 88% reduction in transmitted power which, provided the baseline transmission signal variation is ≪ 88% of the baseline transmission amplitude, will ensure transmission based detection of beads with a high signal to noise ratio. The small increase in transmission of 2.6% will be harder to detect as it will require a very low baseline transmission signal variation.

3.11 Conclusion

This chapter has detailed the design of the optical light path to allow excitation of fluorescence from flowing beads and also collection of light from the fluidic channel. A basic waveguide layout of axially aligned input and output channel waveguides bisected by a rectangular cross section microfluidic channel was devised. Positioning the waveguide layer halfway up the height of the microfluidic channel cross section would allow illumination of both inertial focussing equilibrium positions and allow transmission based detection of flowing beads.

A silica based material system with a germania doped core was selected as the refractive index is similar to that used in the cores of commercially available optical fibres allowing efficient input and output coupling. The index contrast is sufficient to ensure the majority of the optical power is contained in the core allowing fine control of the spotsize by adjustment of the waveguide dimensions. The high silica content in the core material also minimises any difference in etch rates which can cause etch defects. The refractive indices of the deposited films at the wavelengths required for excitation of bead based assays were measured by ellipsometry and confirmed with prism coupling. The sputtered germania-silica films had a refractive index of 1.471 and 1.467 at wavelengths of 532 nm and 633 nm respectively. The PECVD silica had a refractive index of 1.461 and 1.456 at wavelengths of 532 nm and 633 nm respectively, and was shown to match that of bulk silica.

These refractive indices were used as parameters in the subsequent numerical simulations of the optical light path using the BeamPROP software which uses the beam propagation method. The waveguide dimensions required for single mode operation at both 532 nm and 637 nm wavelengths were determined to be 2 µm wide by 2 µm high. The coupling efficiency for butt-coupling of light with a single mode waveguide to a 2 µm wide by 2 µm high integrated waveguide were calculated as 0.90 and 0.84 for wavelengths of 532 nm and 633 nm respectively. Simulated mode profiles of the single mode waveguides confirmed the majority of the optical power is confined in the core. Simulations of the coupling efficiency of axially aligned channel waveguides, optically coupled across a microfluidic channel determined that a 20 µm microfluidic channel has a coupling efficiencies of 0.79 and 0.88 for 2 µm and 10 µm waveguide widths respectively allowing enough light across to the collection waveguide for transmission based detection of flowing beads. The effect of a flowing bead interrupting transmission between waveguides by passing through the beam was simulated revealing a dual dip transmission signal caused by refraction based deflection of the beam by the passing bead. The transmission minima corresponded to a transmission dip of 78% which was expected to allow transmission based detection with a high signal to noise ratio.

CHAPTER 4

Device Fabrication

4.1 Introduction

The ability to mass produce highly accurate, identical devices with intrinsically aligned elements is a key virtue of integrated optics. The microflow cytometer device developed in this work was designed as a monolithic silica based chip partly to exploit the mass production techniques used by the microelectronics industry.

In Chapter 3 the designs for the waveguides and the basic microfluidic channel structure were described. For the waveguide structures a germania:silica was selected, BPM based simulations concluded that a waveguide core layer of 2 μm thickness would allow single mode waveguides to be produced but also allow wider waveguides to be produced to allow for wider beam widths. A rectangular cross section microfluidic channel was selected as it would produce inertial focussing of beads with two equilibrium position.

In this chapter the dimensions of the microfluidic channel are first designed and the final chip design is presented. Then a detailed description is given of the fabrication processes used to produce the integrated optical microflow cytometer devices. The fabrication processes were selected and developed with the aim to realise the designs with the best possible accuracy whilst keeping to the key aim of making a device suitable for mass production. The fabrication protocol was built around the widely available mass production techniques of photolithography, magnetron sputtering, plasma enhanced chemical vapour deposition (PECVD) and inductively coupled plasma (ICP) etching.

4.2 Microfluidic channel design

4.2.1 Theoretical determination of channel dimensions

Having identified inertial focussing as the ideal particle focussing method in Chapter 2, this section describes the design of the microfluidic channel dimensions using theoretical relationships. Using a straight, rectangular cross section microfluidic channel produces inertial focussing at two equilibrium positions centred on the long faces of the channel cross section. By positioning the waveguides halfway up the long face of the channel, the beam crossing the channel will illuminate both equilibrium positions as shown in Figure 4.3 (a) and (b).

As the particle diameter is set at 5.6 µm for a standard Luminex immunoassay bead the fluidic channel dimensions must be chosen to allow inertial focussing to take place whilst being simple to fabricate and operate at practical back pressures and flow rates. As a first step the minimum channel aspect ratio of $h/w = 3/2$ known to produce two equilibrium positions, was chosen in order to minimise the depth of channel required for a given width [49]. The channel depth determines the fabrication time as it determines the thickness of cladding and the etch depth required for correct vertical positioning of the waveguides. For a set aspect ratio the channel width and length determine the minimum flow rate and flow velocity required for inertial focusing to take place, the channel length required for beads to reach equilibrium and ultimately the fluidic resistance of the channel and pressure drop across it. As full inertial focussing occurs when $R_p \geq 1$, the minimum flow rate required for inertial focussing can be calculated for any channel width when $a = 5.6$ µm, $Re_p = 1$ and $h = 1.5w$ using the following equation derived from equation 2.2.

$$Q = \frac{3Re_p \mu w^4}{4\rho D_h a^2} = \frac{5\mu w^3}{8\rho a^2} \qquad 4.1$$

Figure 4.1(a) shows that the minimum flow rate required for inertial focussing increases rapidly with channel width as $Q \propto w^3$. The minimum average fluid velocity required for inertial focussing is shown to increase linearly with increasing channel width as $U \propto w$ because $U = Q/A$. Using this minimum average fluid velocity in equation 2.5 with estimated lift coefficients of $C_{L1} = 0.5$ and $C_{L2} = 0.05$ [49] yields the channel length required for beads to reach equilibrium which is shown in Figure 4.1(c) to increase with channel width as $L_f \propto w^2$.

The fluidic resistance, R of a channel when $L = L_f$ for varying widths can now be calculated according to the following equation [72].

$$R = \frac{12\mu L}{hw^3(1 - 0.63w/h)} \qquad 4.2$$

Then the pressure drop, ΔP, can be calculated using the minimum required flow rate Q.

$$\Delta P = RQ \qquad 4.3$$

It can therefore be observed from Figure 4.1(d) and Figure 4.1(e) that the fluidic resistance of a channel of $L = L_f$ decreases with channel width but the total pressure drop across the channel increases linearly with channel width as a greater flow rate and channel length are required for inertial focussing to take place in wider channels.

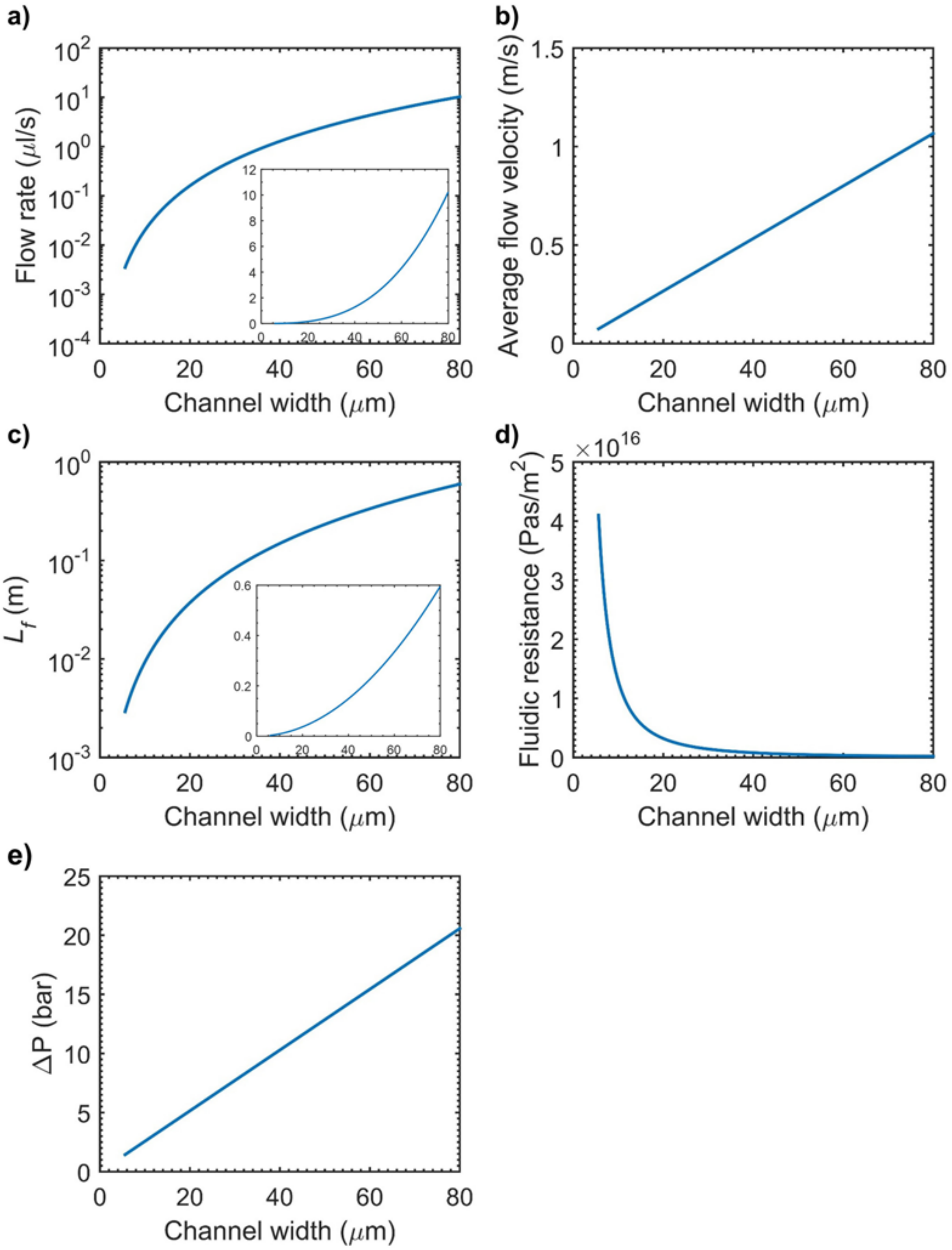

Figure 4.1: Theoretical graphs showing how varying the microfluidic channel width when $h = 1.5w$, $Re_p = 1$ and a=5.6 µm affects (a) flow rate required for inertial focussing, (b) average flow velocity required for inertial focussing (c) the channel length, L_f, required for beads to reach equilibrium (d) fluidic resistance for a channel of length L_f and (e) the pressure drop across a channel of length L_f at flow rate Q. Inset plots show a linear Y axis.

From these calculations channels with widths approaching the bead diameter appear to be advantageous as they are quicker to fabricate and also incur a lower overall pressure drop however a significant practical drawback is that they are vulnerable to blocking. As a compromise to minimise the pressure drop and channel length but reduce blocking vulnerability a channel with a height of 30 µm and width of 20 µm, shown in Figure 4.3 (a), was selected. For this cross sectional dimensions inertial focussing is theoretically predicted to occur at a minimum flow rate of 0.16 µl/s which produces an average fluid flow velocity of 0.27 m/s. Figure 4.2 shows the theoretical downstream length required to focus immunoassay beads in a channel with the above cross sectional dimensions for a range of flow rates calculated using equation 2.5 with estimated lift coefficients of $C_{L1} = 0.5$ and $C_{L2} = 0.05$ [49]. This relationship yields a maximum channel length required for inertial focusing of 37 mm at the minimum flow rate of 0.16 µl/s operating at a pressure of 5.1 bar which can be effectively sealed using adhesive based wafer sealing techniques [73]. Using a higher flow rate will allow inertial focussing to take place over a shorter downstream distance for example a flow rate of 0.3 µl/s ($U = 0.5$ m/s) gives $L_f = 20$ mm. A channel of 20 µm width was also simulated in Chapter 3 to produce an input waveguide to output waveguide coupling efficiency of 0.79 which was expected to allow transmission based detection of flowing beads with a high signal to noise ratio.

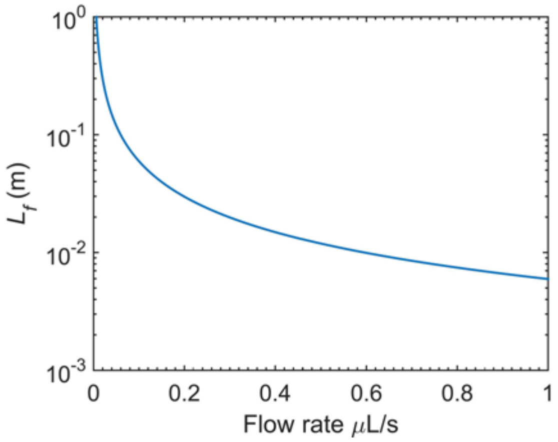

Figure 4.2: Theoretical downstream length required to focus 5.6 µm diameter beads in a fluidic channel with cross sectional dimensions of $h \times w = 30 \times 20$ µm^2 with varying flow rate.

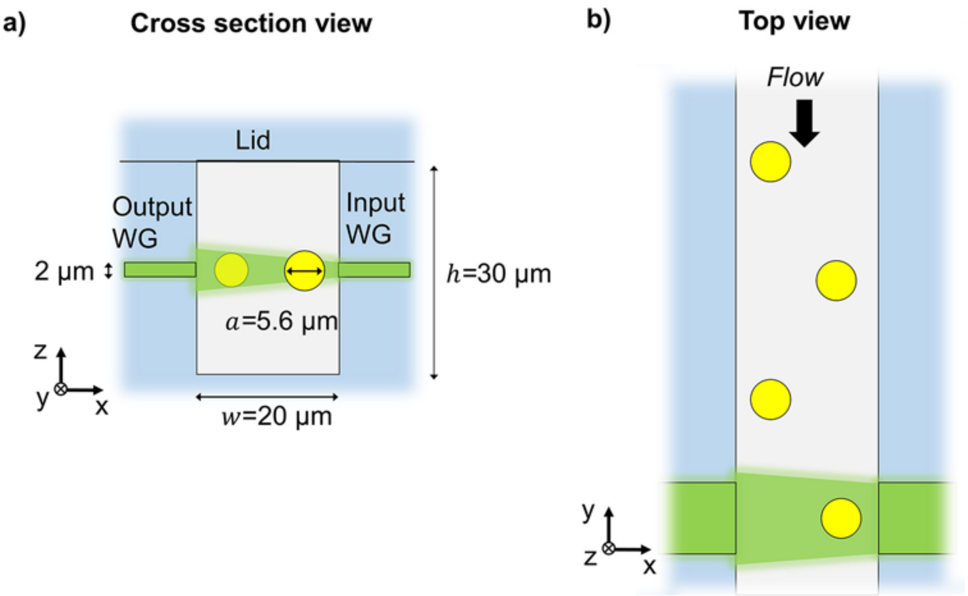

Figure 4.3: (a) Cross section view of microfluidic channel with inertially focussed 5.6 µm diameter beads at approximate equilibrium positions. (b) Plan view of microfluidic channel showing inertially focussed beads passing through the beam

4.2.2 Experimental determination of inertial focussing length using test channels

A preliminary study with PDMS test channels was conducted to experimentally measure the length of channel required for inertial focusing to take place and compare this to the theoretical predictions. The channel length required to focus beads parallel to the long face of the microfluidic channel was assessed as migration in this direction requires the most downstream distance.

The PDMS test channels were manufactured with standard soft lithography techniques [74], [75]. The PDMS microfluidic blocks were bonded to a glass substrate using oxygen plasma sealing [76], [77] and input and output ports were punched at each end of the channels and fluidic tubing was inserted. The PDMS channels were fabricated with a slightly smaller cross section as they were expected to expand under flow to approximate the dimensions of a 30 × 20 µm^2 glass channel. Figure 4.4 shows a microscope image of the cross section of the fabricated PDMS channel which had dimensions of w = 25.5 µm, h = 12.2 µm and L = 40 mm. The long face of the channel was orientated parallel to the glass substrate to allow viewing of the bead flow streams in this direction.

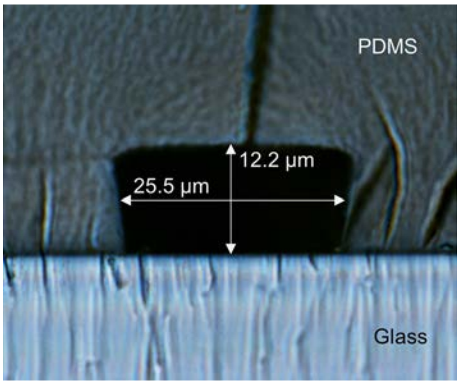

Figure 4.4: Microscope image of the cleaved cross section of PDMS microfluidic channel oxygen plasma sealed to a glass substrate.

5.6 µm fluorescent calibration beads (CAL1, Luminex, USA) were flowed down the channel at a flow rate of 0.13 µl/s ($U = 0.22$ m/s). Higher flow rates could not be achieved with the tubing connections used. The fluorescence streaks from multiple fluorescent beads were imaged using the method described in detail in Chapter 6, section 6.2.2. Fluorescence was excited from the flowing beads by transmission illumination using a laser beam from a 633 nm Helium-Neon (HeNe) laser focussed through a 20× microscope objective onto a region of the microfluidic channel. The illuminated region was imaged onto a CCD camera using a fluorescence microscope and a video was recorded of the fluorescent streaks left by flowing beads. Image processing to combine the fluorescence streaks from multiple beads onto a single image displayed the distribution of all bead flow paths during the video acquisition period.

Figure 4.5 shows the images of the fluorescence streaks taken at 5 mm intervals down the length of the microfluidic channel. At the channel entrance the bead flow streams were spread from wall to wall and as beads progressed down the channel the flow streams became confined into a narrow flow stream at the centre of the microfluidic channel wall due to inertial focussing. By taking the intensity profile across the channel width in each image it was possible to measure the distribution of bead flow streams. Figure 4.6 shows the width of the intensity profile of each image, measured as the full width at half maximum intensity was reduced to near the bead diameter by 15 mm downstream from the channel entrance indicating inertial focussing had effectively confined all beads to the middle of the channel. The bead flow streams remained confined until the channel outlet at 40 mm.

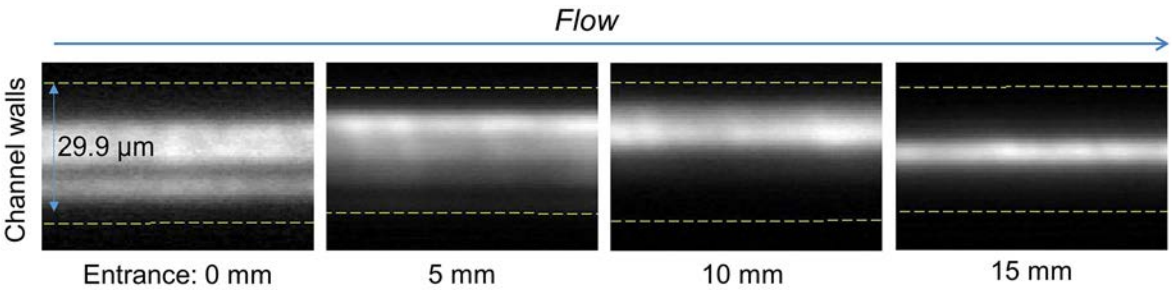

Figure 4.5: Fluorescence microscope images of the fluorescent streaks from multiple flowing fluorescent beads flowing in the PDMS test channel. Images from left to right show the distribution of bead flow streams sequentially at 0 mm, 5 mm, 10, mm and 15 mm from the microfluidic channel entrance.

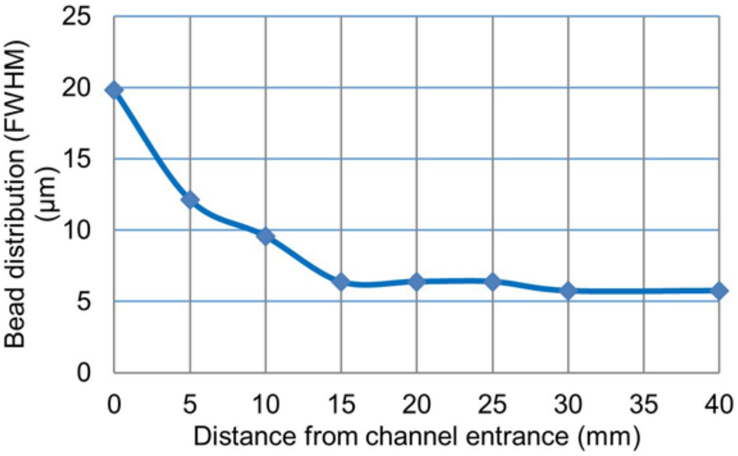

Figure 4.6: Distribution of beads across the channel width measured as the full width at half maximum intensity of the imaged fluorescence streaks at successive intervals downstream from the channel entrance.

Measurement of the channel width during sample flow revealed that the pressure caused the elastomeric PDMS channel to expand in width by 17% to 29.9 µm. The expanded channel width approximated the dimensions chosen for the final silica channel height and so could be used to estimate the downstream required length for inertial focussing in the final device. Inserting this measured channel length into equation 2.6 yields the lift coefficient for particle migration along the channel long face as C_{L2}=0.07. This is higher than the lift coefficient suggested in the literature of $C_{L2} = 0.05$ [49] and explains why inertial focussing is observed experimentally to occur over a shorter downstream distance than predicted by theory.

Based primarily on the experimental results it was decided that a channel of 30 mm length should be long enough to allow full confinement by inertial focussing and provide enough additional length to position waveguides for illumination of the focussed stream. A plan view schematic of the final microfluidic channel design on the chip is shown in Figure 4.7 (a). The microfluidic channel inlets and outlets consisted of circular reservoirs which were designed to allow a flat bottomed ferule to be pressure sealed on top for fluidic connections.

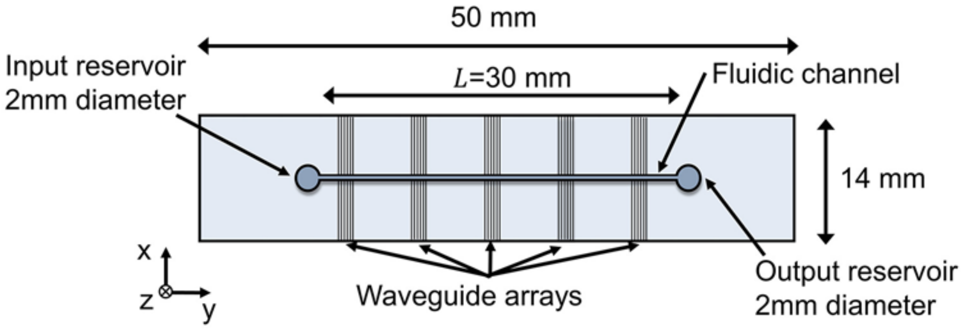

Figure 4.7: Plan view schematic of the proposed chip design.

The final channel dimensions chosen for the microfluidic channel in the microflow cytometer device were 20 µm wide by 30 µm deep and 30 mm long.

4.3 Fabrication overview

The fabrication steps required to make the integrated optical microflow cytometer developed in this work are shown in Table 4.1. Detailed explanations of the fabrication techniques used, and the reasoning behind them are given in the subsequent sections.

Table 4.1: Overview of all fabrication steps required to make the integrated optical microflow cytometer.

Step	**Process**
	Waveguides
1.	Clean substrates with solvent clean then piranha clean
2.	Deposit 2 µm GeO_2:SiO_2 films by sputtering
3.	Anneal, 6 hours 950 ºC in 5 L/min O_2.
4.	Define waveguide layout using photolithography
5.	Deposit 200 nm thick chrome by electron-beam evaporation.
6.	Remove resist by lift-off, to reveal chromium mask layer.
7.	ICP etch GeO_2:SiO_2 film to a depth of 2 µm.
8.	Remove chrome mask with wet etching.
9.	Clad waveguides with up to 4 µm SiO_2 by PECVD.
10.	Anneal cladding at 950ºC for 6 hours in 5 L/min O_2.
11.	Repeat steps 9 and 10 until a cladding thickness of 18 µm is reached.
12.	Cut out separate chips using a wafer dicing saw.
13.	Planarize cladding by polishing the chip surface.
	Microfluidic channel
14.	Clean substrates with solvent clean then piranha clean.
15.	Define microfluidic channel layout on chip with photolithography.
16.	Deposit 1 µm thick chrome by electron-beam evaporation.
17.	Remove photoresist by lift-off to reveal chrome mask.
18.	ICP etch to depth of 30 µm.
19.	Remove chrome mask with wet etching.
	Polishing
20.	Cut off 1mm of end of waveguides with wafer dicing saw.
21.	Polish waveguide end facets.
	Sealing microfluidic channel
22.	Seal top of microfluidic channel with SU-8 coated coverslip with access holes predrilled.

4.4 Substrate selection and preparation

A SiO_2 (silica) based material system was chosen for the device for several reasons. Primarily silica offers superior optical characteristics compared to polymers [78], including low absorption in the visible range and low autofluorescence which can be a source of background noise for fluorescence measurements. Also the rigid and hard nature of silica means devices can withstand high fluid pressures and can be used many times without deformation of the device structure. Additionally, the low coefficient of thermal expansion reduces temperature related effects on optical performance, which is especially important for integrated optical components with stringent dimensional tolerances such as MMI devices and kinoform lenses. Also silica is compatible with a wide range of relevant biological solutions including most acids, buffered saline and solvents.

Bulk silica substrates (Spectrosil 2000, UQG optics, UK) of dimensions 50 mm × 50 mm and 1 mm thick were used as the transparency allows viewing of the device from both sides and the bulk silica matches the thermal expansion properties of the layers deposited on top. Two chips could be fitted on a substrate allowing some batch production. An alternative substrate would be thermally grown SiO_2 on silicon, which is more cost effective in large wafer sizes making it more suitable for batches, however the opaque silicon and the potential for thermal expansion mismatch are drawbacks.

Cleaning the substrate is a vital part of the fabrication process as any contamination on the surface can cause problems further down the fabrication chain. Particles can cause pin holes in deposited films or inclusions which can increase waveguide propagation losses or prevent any light guiding at all. Surface layers of organic contaminants can lead to poor adhesion of deposited layers. The cleaning procedure used for all substrates and newly deposited films was to sonicate, in acetone, then isopropanol for 10 minutes each, followed by a water rinse. This step removes the majority of particulates and grease on the surface. A further 20 minute immersion in a so called ‘piranha’ mixture consisting of 1 part 38% hydrogen peroxide added to 3 parts 98% sulphuric acid was used to completely remove organic contaminants. Following this the substrate is again rinsed in DI H_2O and oven dried for 4 hours at 120 ºC to dehydrate the surface.

4.5 Magnetron sputtering of GeO_2:SiO_2

RF sputtering was chosen as the deposition method for the GeO_2:SiO_2 films as it has excellent thickness uniformity, good film adhesion and the refractive index can be controlled by the sputtering target composition.

A typical RF sputterer configuration is shown in Figure 4.8 and consists of a cathode mounted target which is composed of the material to be sputtered, opposite to an anode mounted substrate, all contained in a vacuum chamber. Gases are pumped into the chamber and ionised into a plasma by a 13.56 MHz alternating voltage between the electrodes. The ions are accelerated towards the cathode bombarding the target, ejecting the target atoms which deposit on the substrate surface. For GeO_2:SiO_2 deposition Ar ions bombard the target whilst the O_2 ions combine with free Ge and Si to maintain stoichiometry in the deposited film [79].

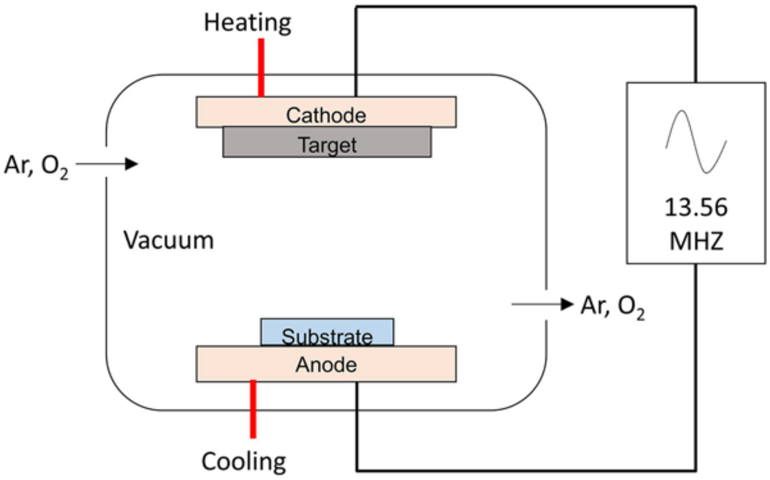

Figure 4.8: Schematic of the chamber setup for RF sputtering.

Substrates were sputtered on a Plasmalab 300 sputtering machine made by Oxford Instruments, UK. The target used had a GeO_2:SiO_2 composition of 24.75%:75.25% by weight respectively which was expected to give a refractive index difference over bulk silica of ~0.015 [61], [80]. The sputtering conditions were a magnetron power of 300 W, chamber pressure of 10 mTorr, the gasses used were O_2 at 5 sccm and Ar at 20 sccm. These parameters were selected based on the work by Dr Hamish Hunt [66] and advice from Neil Sessions. Two chamber temperatures were investigated, 20 ºC and 200 ºC to investigate the effect of deposition temperature on film propagation losses.

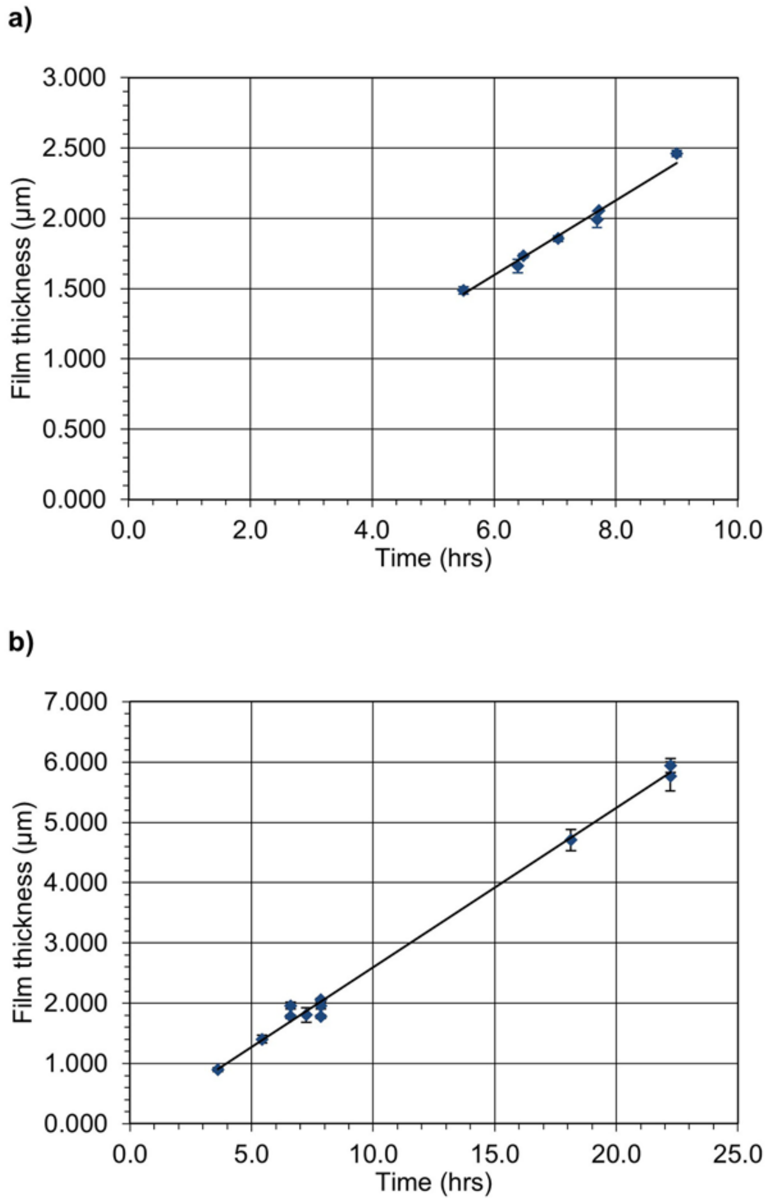

Figure 4.9: The deposition thickness with respect to time, measured by profilometer for sputtering at substrate heating temperature of (a) 20 ºC and (b) 200 ºC.

The thickness of the deposited films compared to a tape-masked region was measured on a KLA-tencor P-16 stylus profilometer. Figure 4.9 shows that the sputtering rates for both chamber temperatures were similar at 0.27 µm/hr and 0.26 nm/hr for 20 ºC and 200 ºC respectively. Prism coupling at a wavelength of 633 nm was used to measure the refractive indices and propagation losses of the sputtered films after annealing. The refractive index was the same for both deposition temperatures at 1.469 ±0.0007. The propagation losses were 1.5 dB/cm ± 0.4 dB/cm and 0.7 dB/cm ± 0.4 dB/cm for the films deposited at 20 ºC and 200 ºC respectively. The lower propagation loss for the film deposited at 200 ºC was thought to be due to an annealing effect during deposition, reducing structural discontinuities in the film and homogenising the refractive index.

GeO_2:SiO_2 films for the final devices were deposited at 200 ºC to thickness of 2.0 µm, with a thickness variability of 0.05 µm (1 standard deviation) for a single film and thickness variability of 0.07 µm between samples.

4.6 Silica PECVD

Plasma enhanced chemical vapour deposition (PECVD) was chosen to deposit the SiO_2 cladding mainly because the high deposition rate is more efficient for the thick cladding than sputtering. Other advantages include, good adhesion, surface conformity and the ability to control the film refractive index using the flow ratio of the precursor gases.

Figure 4.10 shows the setup for the PECVD machine (Plasmalab 100 system PECVD, Oxford Instruments, UK) used in this work. The chamber contains two electrodes, a top electrode, through which a gas shower head runs, and a bottom electrode which is a heated table on which the sample sits. The top electrode is connected to a RF power source oscillating at 13.56 MHz while the bottom electrode is grounded. The heated table raises the substrate temperature to a range between 250 ºC and 450 ºC. Precursor gases are pumped into the chamber through the shower head and out through the bottom of the chamber which is maintained at a pressure range of 0.5-1.0 Torr. The gases are ionized into a plasma by the RF voltage between the electrodes, the free electrons produced initiate the reaction of neutral precursor molecules on the surface of the substrate. Additionally, ions are accelerated towards the bottom electrode and bombard the substrate producing more active sites at the surface, increasing the deposition rate [79].

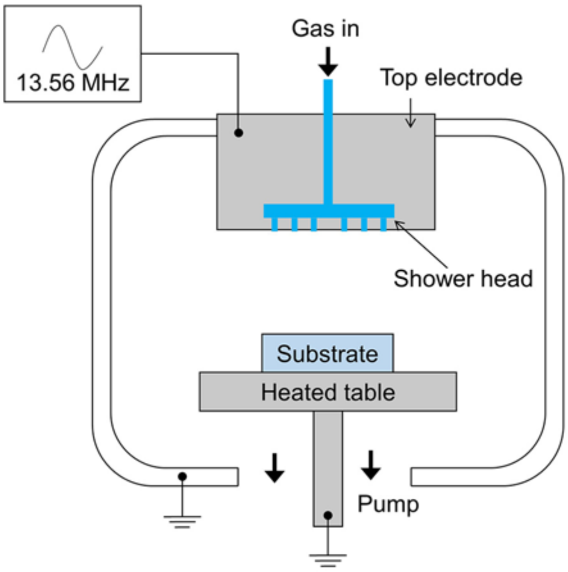

Figure 4.10: Schematic of the PECVD setup used.

The basic parameters used in this work for deposition of SiO_2 was an RF power of 20 W, chamber pressure of 1000 mTorr, table temperature of 350ºC. These parameters were selected based on advice from oxford instruments and Dr Owain Clark. The gases used were N_2 at 80 sccm and precursor gases of N_2O and SiH_4, at a range of flow ratios.

The first batch of annealed films deposited with precursor gas flow ratio of 141:1, $N_2O:SiH_4$ were observed to crack when stored in the presence of air in Teflon (polytetrafluoroethylene) boxes for a period of 1 week or more indicating that the films were under tensile stress. This was especially apparent with films of 8 µm and above. In addition the refractive index of these annealed films was measured by prism coupling at a wavelength of 633 nm to be 1.470 which was too high for use as a cladding. The cause of the tensile stress and high refractive index was thought to be due to a silicon rich film based on reports in the literature [81], [82]. The effect of the flow ratio of the precursor gases, on the film refractive index was investigated with the aim of depositing a low stress film with a refractive index as close to bulk SiO_2 as possible. The refractive index of the film was used as a metric for the film stoichiometry. Figure 4.11 shows that as the ratio of $N_2O:SiH_4$ was increased the refractive index of the non-annealed film decreased, tending towards that of SiO_2. This trend matches those reported in the literature [82] however the gas ratios used here to achieve the same refractive indices are approximately 25× higher. This was later attributed to a clogged gas filter in the PECVD machine which may have slowed the actual input gas flow rate for both gases.

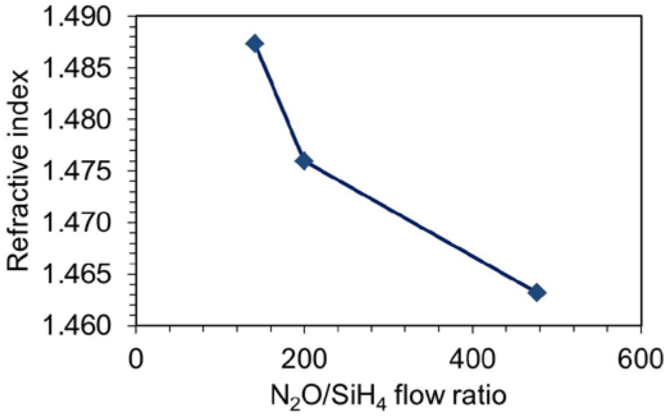

Figure 4.11: Refractive index of PECVD silica before annealing versus precursor gas flow rate ratio. Error for each measurement is 0.0001 (1 SD).

The final optimised flow rates selected for PECVD silica deposition were N_2O at 2000 sccm and SiH_4 at 4.2 sccm. This flow ratio produced a non-annealed film refractive index of 1.4632 ± 0.0001 and an annealed film refractive index of 1.4571 ± 0.0001 at a wavelength of 633 nm. The annealing process is described in the next section. At this flow ratio the deposition rate was 1.92 µm/hr, which is much faster than sputtering of SiO_2 which was measured at 0.135 µm/hr. As an extra measure to reduce film stress the cladding was deposited in steps of no more than 4 µm followed by annealing. The cycle was repeated until the final cladding depth required for the devices of 18 μm was achieved.

4.7 Annealing

Newly deposited films are annealed in the presence of oxygen to relieve film stress and also to restore the film stoichiometry. Oxygen deficiency can change the refractive index of the film and lead to high losses due to absorption.

The GeO_2:SiO_2 substrates with the newly deposited films were annealed in a tube furnace at 600ºC for 6 hours with an O_2 flow of 2 L/min and a temperature ramp up/down rate of 5 ºC/min. The effectiveness of the annealing process was investigated by measuring the refractive index and propagation losses of the deposited films by prism coupling.

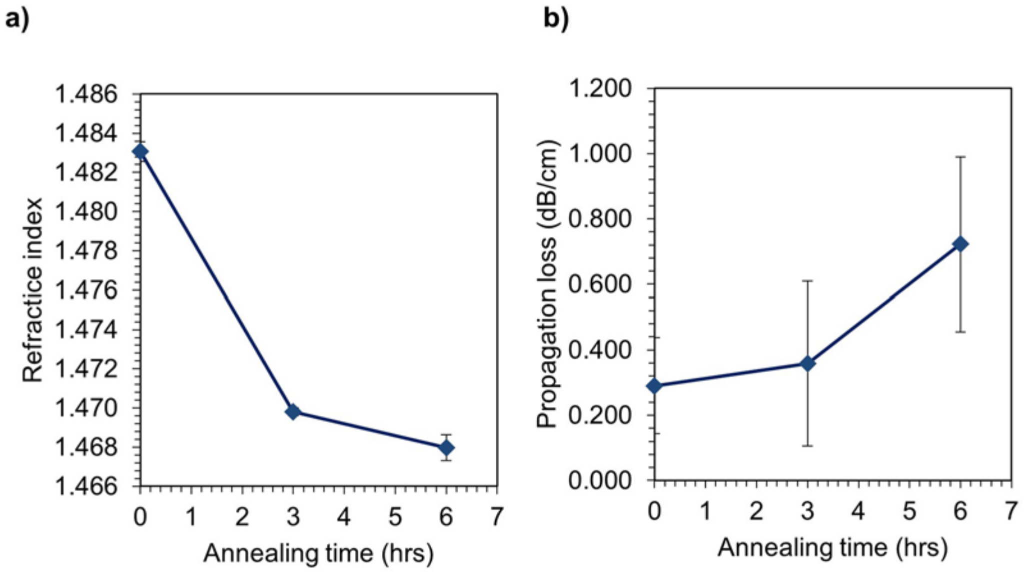

Figure 4.12: Effect of annealing GeO_2:SiO_2 films at 600 ºC on (a) refractive index and (b) slab propagation loss. Measured using prism coupling with TE polarisation.

Figure 4.12 shows the effect of annealing the GeO_2:SiO_2 films at 600 ºC on the refractive index and on the propagation loss of the film. The refractive index was shown to decrease with annealing time, after 6 hrs the final refractive indices were 1.4680 and 1.4685 for TE and TM polarisations which is lower than reported in the literature [61], [83]. The birefringence of the films is the difference in refractive index for TE and TM polarisations and so was deemed to be negligible at 5×10^{-4}. The propagation losses were shown to increase with annealing time.

The PECVD silica films were annealed after each 4 μm thick deposition step at 950 ºC for 6 hrs. The higher temperature was used for more effective stress release as it is closer to the softening temperature of silica [84].

4.8 Photolithography and Lift-off

Photolithography was chosen as the waveguide and microfluidic channel pattern transfer technique as it is highly accurate, with a resolution of down to 0.8 µm, and can produce batches of identical devices, simplifying mass production. Other pattern transfer techniques for producing waveguides in include direct writing of the waveguide core using UV writing [85] and e-beam lithography [86] to define a photoresist mask. Microfluidic channels can also be fabricated by micromilling [39]. All of these direct write methods are suitable for rapid prototyping with high accuracy but do not have the mass production capability of photolithography.

The lift-off process is a method by which metal patterns are created on a substrate using a sacrificial photoresist layer. A bi-layer lift-off process, using two layers of resist was used in this work as it allows micron thick chrome layers to be deposited. The general procedure is shown in Figure 4.13. First the lift-off resist layer is spin coated onto the substrate, and soft baked to remove the solvent. Then the imaging resist is applied using the same process. Next the imaging resist is exposed to UV light through a patterned mask. The exposed imaging resist is soluble in developer and is dissolved during the development stage, exposing the lift-off resist layer which is also dissolved leaving an undercut. The substrate is then coated in chromium by electron-beam (e-beam) evaporation deposition, which is described in more detail in the next section. The final step is to dissolve away the resist bilayer leaving only the chromium in direct contact with the substrate.

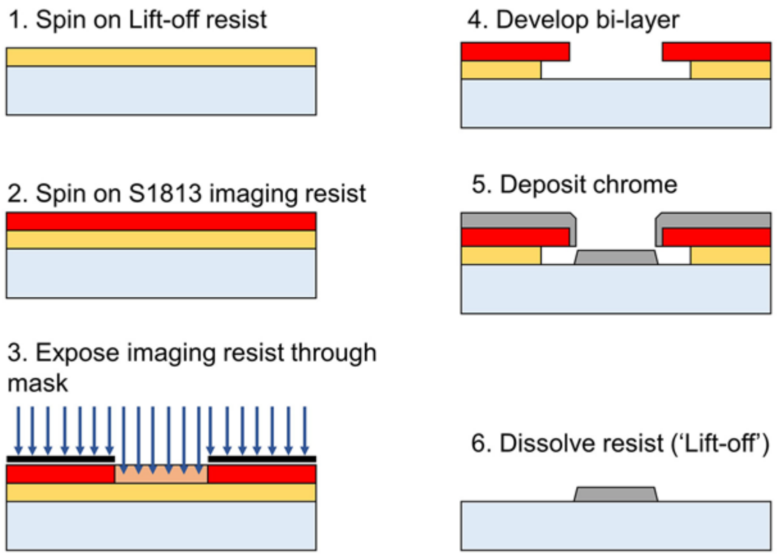

Figure 4.13: Bi-layer photolithography and lift-off process.

For the waveguide hard mask a 300 nm thick lift-off resist layer (LOR-3B) with a 1.3 µm imaging resist layer (S1813) was used. For the microfluidic channel hard mask a 2.8 µm thick lift-off resist layer (LOR-30B) with a 1.3 µm imaging resist layer (S1813) was used [87]. All resists were supplied by Microchem Corp, USA.

4.9 Electron-beam evaporation deposition

Chromium was selected as the hard mask material for ICP etching as it has a low etch rate compared to SiO_2. Electron-beam evaporation deposition was chosen as the deposition method for the chrome mask as it is capable of producing micron thick layers at a high deposition rate. In addition the deposition process is line-of-sight which gives a cleaner lift-off. In the e-beam deposition system used, the substrate is placed in a vacuum chamber on a rotating stage above a crucible containing the metal to be deposited. A high intensity beam of electrons is magnetically focussed into the crucible to sublimate the metal into a vapour which condenses on the substrate [79].

Hard masks were deposited on substrates at a rate of 0.65 µm/hr. The thickness of the hard mask required, T_C, based on the required etch depth, h, and etch selectivity, S, was calculated using the following equation.

$$T_C > \frac{h}{S} \times 1.85 \tag{4.4}$$

The multiplication factor was determined by multiple etch tests and is required to add extra chrome thickness on any sloped features on the substrate. The hard masks thicknesses used for the etching of the waveguides and microfluidic channels were 100 nm and 1.3 µm respectively.

4.10 ICP etching

Inductively coupled plasma (ICP) etching was used to etch the channel waveguide structures and the microfluidic channels. The technique was chosen as it can produce etched structures with vertical side walls at a high etch rate [88]. A waveguide cross section with vertical side walls is desirable as it will produce a symmetrical mode profile for efficient input/output coupling. Vertical side walls are also important for the fluidic channel cross section in order to minimise deflection of the beam crossing the channel and also to ensure the correct rectangular shape to enable inertial focussing. Also it is important that the three optical layers are etched at a similar rate in order to minimise distortion to the microfluidic channel shape. ICP etching is ideal as it provides fine control of the selectivity through the ratio of etch gases and also the plasma energy.

Figure 4.14 shows the setup for the ICP system (Plasmalab 100 ICP380, Oxford instruments, UK) used. The substrate is loaded into the chamber and sits on a Helium cooled table. Gases are pumped into the chamber and ionised into a dense plasma by the RF driven coil in the upper part of the chamber. The etch process is partly physical and partly chemical. An RF bias on the substrate table at the bottom of the chamber accelerates the ions down onto the substrate ejecting molecules from the substrate surface. Chemical etching is performed by free radicals from the plasma which adsorb to the substrate surface and react chemically producing volatile products which are pumped out of the chamber. Additionally gas molecules adsorbed to the substrate surface react to form a passivating polymer layer. Any passivation layer on the horizontal surfaces of the substrate are etched away by the ion bombardment, exposing the substrate below to further chemical etching. The side walls of the substrate features remain protected by the passivation layer and so the overall etching process is anisotropic, producing straight, vertical side walls [79].

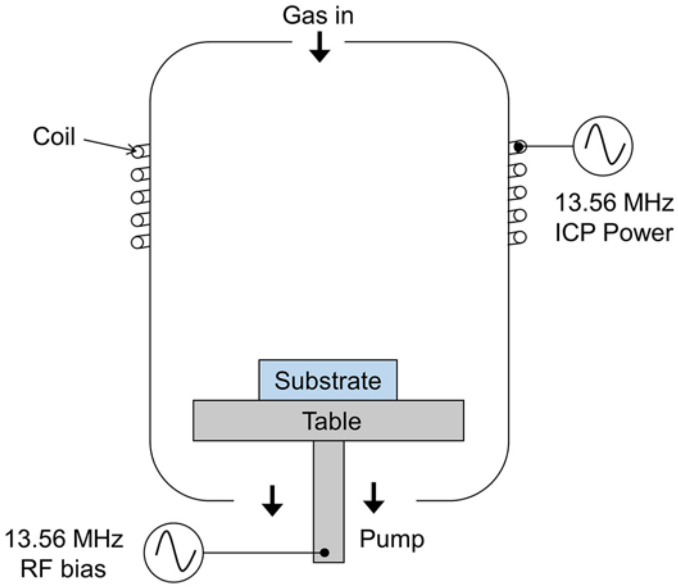

Figure 4.14: Schematic of ICP system used.

4.10.1 Etch rate of materials

In this work the small substrates were loaded into the ICP etcher on top of a 6” silicon carrier wafer. Table 4.2 shows the two ICP processes used. In both processes The C_4F_8 provides fluorine free radicals which chemically etch the SiO_2 and also polymerise to passivate the side walls. The O_2 removes the polymer from the horizontal surfaces and also prevents excessive build-up of polymer. Recipe 1 uses a higher ICP power to produce a dense plasma and the high RF power provides high energy ion bombardment for a fast etch process. Recipe 2 uses lower ICP and RF powers and substrate temperature to increase selectivity as the lower powers and temperature favour polymer formation.

Table 4.2: ICP etch recipes

Parameter	Recipe 1	Recipe 2
ICP Power (W)	2500	1500
RF bias Power (W)	70	32
Chamber pressure (mTorr)	10	10
O_2 flow rate (sccm)	15	10
C_4F_8 flow rate (sccm)	40	28
Table temperature (°C)	45	20
He cooling (sccm)	15	15

Figure 4.15 shows the etch depth versus time for recipe 1, measured on a profilometer on several different samples, for bulk SiO_2 and for sputtered GeO_2:SiO_2. Both show a linear trend showing that etch rate does not change significantly with depth. The etch rate for PECVD silica was also measured but only for a single sample. The etch rate for each material is summarised in Table 4.3. The highest etch rate was for the GeO_2:SiO_2. The PECVD SiO_2 etched at a faster rate than the bulk SiO_2 which suggests the former is of a lower density. The recipe shows a minimum selectivity of 43:1 so a 30 µm deep channel requires a chromium masking layer at least 0.7 µm thick.

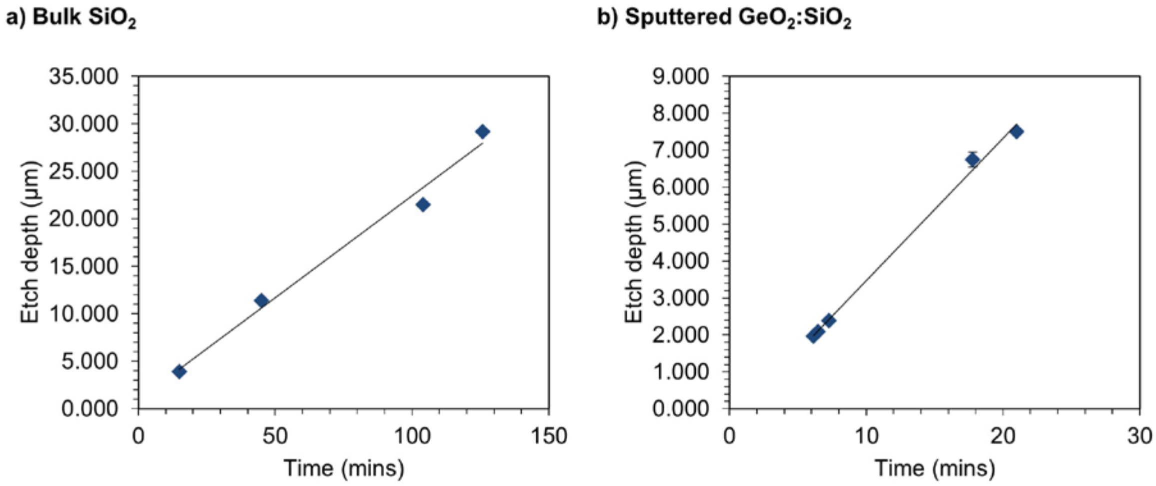

Figure 4.15: Etch depth versus time for (a) bulk SiO2 and (b) sputtered GeO_2:SiO_2 using etch recipe 1.

Table 4.3: Etch rates using ICP etch recipe 1.

Material	Etch rate (µm/min)
PECVD SiO_2	0.261
GeO_2:SiO_2	0.387
Bulk SiO_2	0.215
Chrome mask	0.005

The etch rates allow calculation of the etch time using the following equation.

$$t = \frac{T_{PS}}{R_{PS}} + \frac{T_{GS}}{R_{GS}} + \frac{T_S}{R_S} \qquad 4.5$$

T_{PS}, T_{GS}, and T_S are the thickness and R_{PS}, R_{GS}, and R_S are the etch rates for PECVD SiO_2, GeO_2:SiO_2 and bulk SiO_2 respectively. A 30 µm deep channel took 124 minutes to etch.

4.10.2 Etching of waveguides

Etch recipe 1 was used to etch the channel waveguide structures. The 2.0 µm thick GeO_2:SiO_2 films with a chromium masking layer were etched to a depth of 2.4 µm to ensure complete removal of the core material around the waveguide structure. The side wall angle of the etched waveguides was measured by imaging the end facet of a PECVD clad sample on a scanning (SEM) electron microscope in back scattering mode to enhance the contrast between the core and cladding material. SEM Images of the end facets for the waveguides with an original mask width of 1.8 µm and 10.0 µm are shown in Figure 4.16 (a) and (b) respectively. The waveguides have a trapezoidal cross section with an average top corner angle of 96.8 °±1.4 °, measured for 40 different waveguides. The trapezoidal cross section did not significantly affect the mode symmetry of the intensity profile produced by the waveguides as described in Chapter 5.

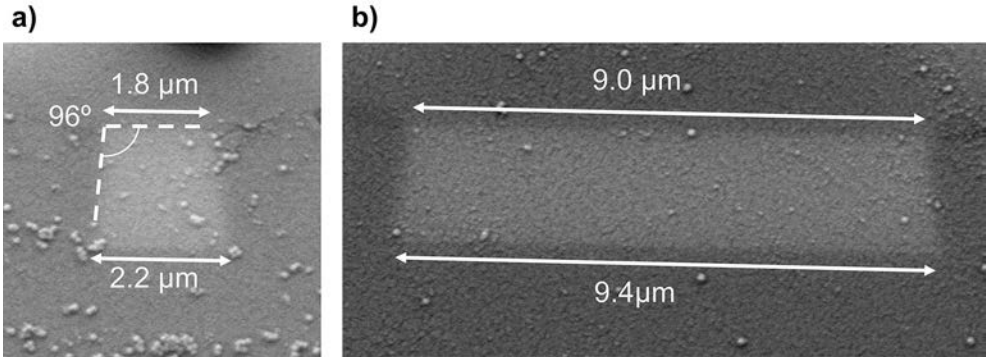

Figure 4.16: SEM images of PECVD clad channel waveguide cross sections for original mask widths of (a) 1.8 µm and (b) 10.0 µm.

Figure 4.17 shows the fabricated waveguide widths versus the original mask width. The narrowest waveguides are larger than the original mask width while the wider waveguides are smaller than the original mask width. The range of waveguide widths fabricated allowed a waveguide width to be selected for single mode or multimode operatation. The 1.8 µm wide mask design produces a waveguide with an average width of 2.0 µm and so should best approximate the dimensions for a single mode waveguide with a symmetrical mode profile specified in Chapter 3.

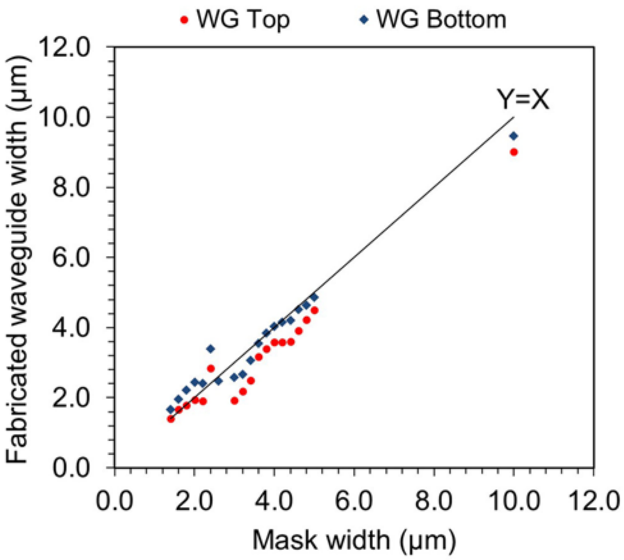

Figure 4.17: Fabricated waveguide width (top and bottom) versus original mask width.

4.10.3 Etching of microfluidic channels

Test samples were etched and the etched structures were imaged by SEM. Figure 4.18 (a) shows the face of the microfluidic channel side wall revealing the three optical layers. The faster vertical etch rate of the GeO_2:SiO_2 is apparent as there is a narrow trench sitting on top of the ridge on the fluidic channel floor. The ridge itself is 2.4 µm high and is due to the original surface ridge formed by the waveguide cladding before etching. The size of the ridge may affect the direction and velocity of the fluid flow. This effect can be reduced by planarization of the chip surface before etching which is described in the next section. The etching has caused some cracking or discontinuity between the PECVD SiO_2 and the substrate SiO_2 which may have been due to heating of the substrate during etching. This cracking is not observed at the polished end facet of the waveguide and so may only be in the immediate vicinity of the microfluidic channel. Figure 4.18 (b) shows the cross section view of a 14.5 µm wide by 27.5 µm deep test microfluidic channel etched into a SiO_2 substrate. The channel cross section shows good verticality overall with an average sidewall angle of 91 º±4.3º measured for 6 different channels on the same substrate. Overall the cross section is a good approximation of the rectangular shape needed for inertial focussing. The trenches at the bottom of the channel are likely due to bombarding ions being deflected by the angled facet of the chromium mask, leading to a higher rate of etching at the bottom corners [79]. This mechanism is illustrated in Figure 4.18 (c). As the trenches run parallel to the direction of flow they are unlikely to significantly alter the direction of fluid streamlines and influence inertial focussing behaviour.

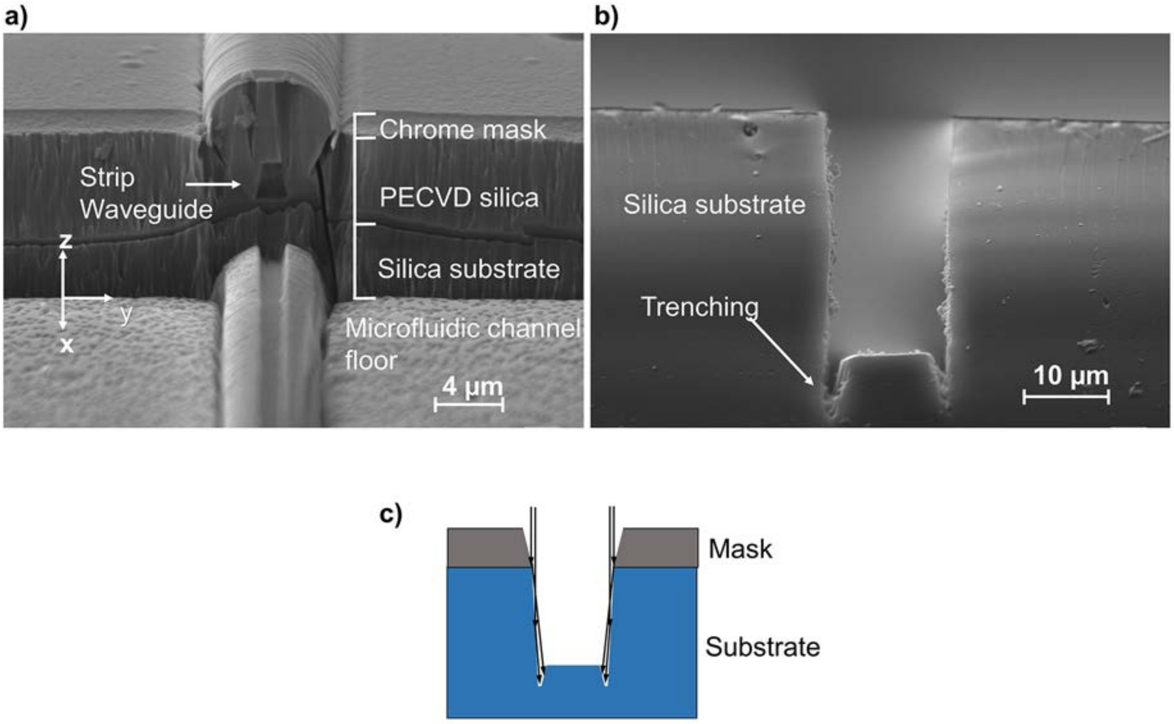

Figure 4.18: Scanning electron microscopy images of the etched microfluidic channels. (a) Angled view of the sidewall of an 8 µm deep channel showing the different optical layers. (b) Cross section of 14.1 µm wide by 27.5 µm deep microfluidic channel etched into bulk SiO_2. (c) Mechanism of ion deflection which produces trenches at the bottom of the microfluidic channel.

Chips with channel waveguides, clad in PECVD silica and with a chromium hard mask were etched to the target depth of 30 µm. Three devices with integrated waveguides and microfluidic channels were fabricated, numbered 1 to 3. Devices 1 and 2 were designed with a microfluidic channel width of 20 µm and were etched using recipe 1.

Device 3 was designed with a microfluidic channel width of 14 µm and was intended to be used for investigation of the effect of a higher aspect ratio microfluidic channel on inertial focussing. The device was not used in the flow cytometry studies however as the narrower channel was susceptible to blocking. The microfluidic channel for device 3 was etched using Recipe 2, the parameters were based on work by Messow et al [88] and the recipe was expected to show improved selectivity and reduce trenching. The recipe showed a better selectivity than recipe 1 at 54:1, but a lower SiO_2 etch rate at 0.091 µm/min. Microscope imaging of the channel cross section of test channels revealed that the trenching effect was significantly reduced, as can be seen in Figure 4.19. This is thought to be due to a lower RF bias power reducing the bombarding ion energy. Drawbacks of this process are the slower etch rate which requires nearly double the time to etch.

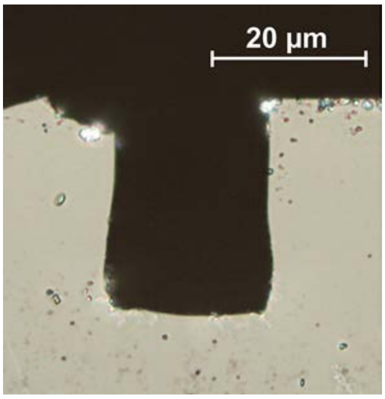

Figure 4.19: Cross section view of a 21 µm wide channel etched into bulk SiO_2 using ICP etch recipe 2.

The final dimensions of the microfluidic channels etched into the three complete devices are shown in Table 4.4. The width of the etched channels was measured as 1.1 µm wider than the mask width on devices 1 and 2 and 1 µm wider than the mask width on device 3. The increase width was thought to be due to a combination of a chromium hard mask with slightly wider features than the design and a small amount of lateral etching.

4.11 Planarization by polishing

As noted in the analysis of Figure 4.18 (a) the etching of the ridged chip surface results in ridges on the floor of the microfluidic channel measured to be 2.4 µm high. Such ‘micro-weir’ structures have been shown to redirect flow to produce a vertical force on flowing particles and so may push the inertial focussing equilibrium positions up [89]. Planarization of the chip surface before etching can prevent these features. Three planarization methods were trialled. Using an FHD deposited cladding was shown to produce a planar top surface however the process required further optimisation to prevent stress based cracking. An etch back process was trialled but produced high surface roughness on the etched surface.

The approach chosen was to surface polish the ridge features flat using chemical-mechanical polishing. The chip was affixed with wax onto a self-levelling mounting block which allowed it to freely rotate. The polishing jig, shown in Figure 4.20 (a) pushes the chip surface against a rotating polishing wheel, shown in Figure 4.20 (b) covered in polishing fluid (Alkaline colloidal silica solution, SF1 polishing fluid, Logitech, UK).

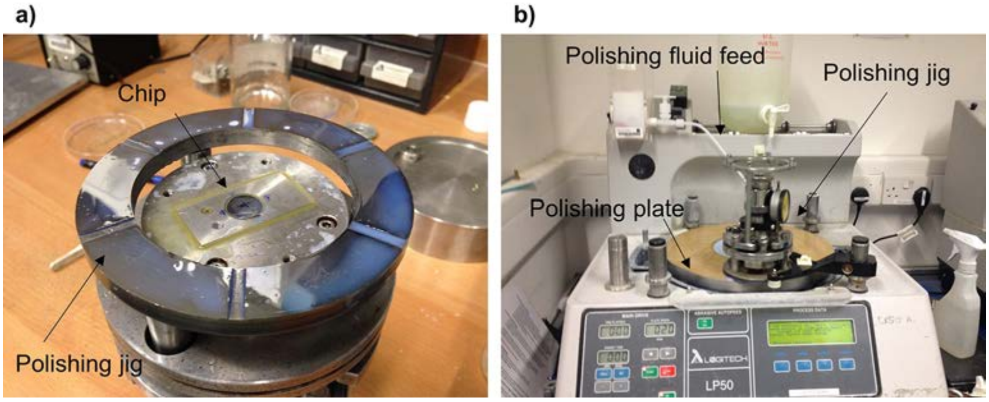

Figure 4.20: (a) Chip affixed to a polishing jig. (b) Polishing jig on rotating polishing plate.

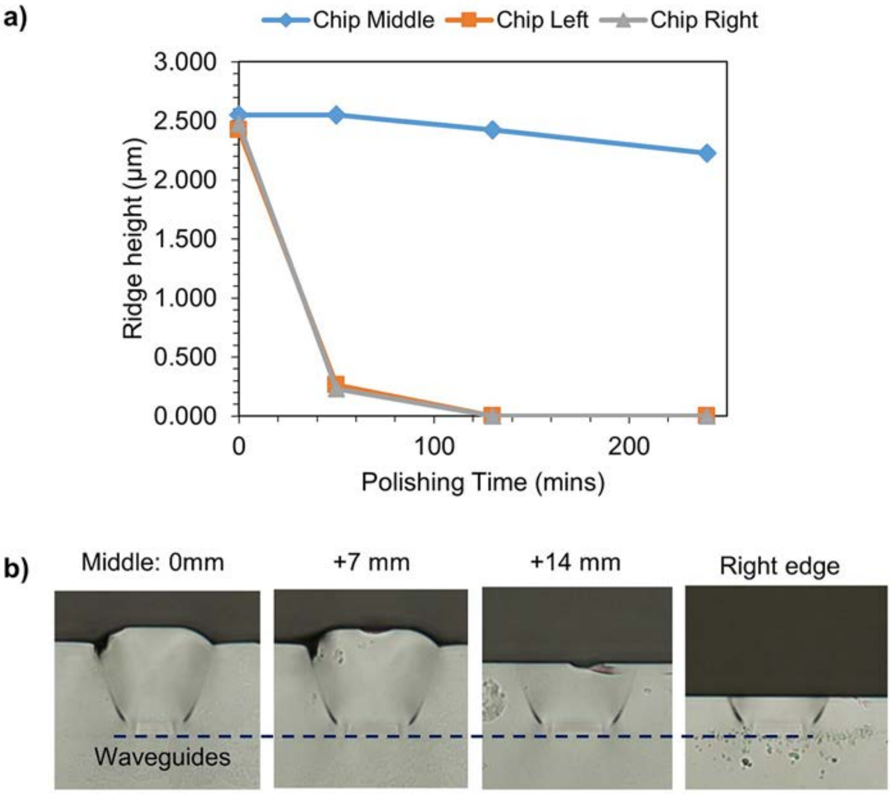

Figure 4.21: (a) Surface ridge height versus polishing time at different lateral position on chip. (b) Cross section view of surface ridges for different lateral position on chip after planarization.

Figure 4.21 (a) shows that the surface polishing rate is fastest at the edge of the chip, and slowest in the middle of the chip. This is because more polishing fluid is able to access the regions close to the edge of the chip, making the polishing rate faster. Figure 4.21 (b) shows the cross-section view of the surface ridges at increasing lateral distance from the middle of the chip, after 4 hrs of polishing. The ridge at the middle shows no planarization whilst the ridge at the right edge is fully planarized and in addition 15 µm of cladding has been removed.

The chemical mechanical planarization process was shown to be effective at local planarization however the polishing rate was dependant on the proximity from the middle of the chip. For the illumination of flowing beads, the waveguides selected for used were halfway up the height of the channel. Whilst this trial used basic equipment available in our lab, chemical-mechanical planarization is used industrially to produce wafers with excellent planarization uniformity [79].

4.12 End facet polishing

After the microfluidic channel were etched, the end facets of the waveguides were polished using conventional lapping and polishing setups. Briefly, chips to be polished were stacked together in wax and affixed to a polishing jig similar to that shown in Figure 4.21 (a). The end facets were first lapped with abrasive alumina slurry to remove around 1mm of waveguide length and planarize the end facets. Next the chip end facets were polished to reduce the surface roughness, giving an optical finish for efficient coupling into the waveguides. The polished end facets of the waveguides are shown in Figure 4.21 (b). The polishing and lapping machines used were Logitech LP50 models each fitted with a polishing and lapping plate respectively.

4.13 Sealing methods

The microfluidic channels required for inertial focussing are long and narrow producing a high back pressure and therefore requires a robust sealing technique. The designs used in this work are 20 µm wide, 30 µm high and 30 mm long and must operate at flow rates up to 0.4 µl/s which gives a pressure drop, calculated using equations 4.2 and 4.3, of 10.36 bar.

A sealing technique using a Polydimethylsiloxane (PDMS) lid bonded to top of the chip using oxygen plasma activated bonding was trialled. Oxygen plasma bonding is a method for irreversibly bonding a PDMS surface to another piece of PDMS or glass by creating covalent bonds between the two surfaces. PDMS consists of polymer chains of $–O\text{-}Si(CH_3)_2$- monomer units. Exposure of the chains near the surface to oxygen plasma causes the $–CH_3$ groups to be replaced with –OH groups. When two activated surfaces are brought into close contact the OH groups form an Si-O-Si bond with the loss of water. Higher bond strengths are achieved by increasing the density of OH sites on a surface by using optimised plasma conditions. Generally a higher plasma pressure (200-1000 mTorr) low RF power (20 W) produce a greater density of surface sites. The exposure time must be limited, usually to less than 30s, to prevent damage to the polymer chains of the PDMS which can lead to decreased bond strength [90]. Bond strength can also be improved after contact by baking the sealed devices in an oven at 95 °C to drive out water at the interface produced from the condensation reaction. Oxygen plasma sealed microfluidic channels sealed using a Tepla 300 plasma system at 1000 mTorr O_2 at 20 W for 20s were observed to delaminate above a channel pressure drop of 2.59 bar ($Q = 0.1$ µl/s, $U_f = 0.17$ m/s). Another technique using pressure clamping of a PDMS lid was shown to leak above a channel pressure drop of 1.29 bar ($Q = 0.05$ µl/s, $U_f = 0.08$ m/s).

The most pressure resistant sealing technique was adhesive bonding of a glass lid over the microchannel using a thin film of SU-8 photoresist as the adhesive. In adhesive bonding the uncured liquid adhesive conforms to the surface it is placed in contact with. Curing of the adhesive causes the monomeric precursors to polymerise into long chains hardening the adhesive layer. The close contact (<0.5 nm) between the adhesive and surface creates very strong van der Waals forces between OH groups on the polymer chain of the adhesive and OH groups on the surface [91]. To ensure a strong bond very close conformal contact must be achieve by ensuring the surface to be adhered to is clean and has a higher surface energy than the adhesive and so is effectively wet by the adhesive. Applying pressure to an interface also improves conformation.

The adhesive sealing procedure was adapted from several techniques used in the literature [92], [93]. Microfluidic channel lids were prepared from 170 µm thick cover slips made from borosilicate glass. The lids were cut to size and two, 2 mm diameter access holes were drilled through 32 mm apart. These lids were cleaned using the silica cleaning protocol and then spin coated with a 3 µm thick layer of the negative photoresist SU8-2 (Michrochem corp, USA). The SU-8 layer was soft baked on a hot plate at 65 ºC for 5 minutes and then 95 ºC for 3 minutes. The hot plate was then reduced until the SU-8 temperature is 72 ºC and slightly tacky. The chip was aligned by hand with the microfluidic reservoirs opposite to the lid access holes and then pressed down onto the lid. The chip and lid were then flipped over and tweezers were used to apply pressure to the lid until full contact was achieved. An assembled device with a lid is shown in Figure 4.22.

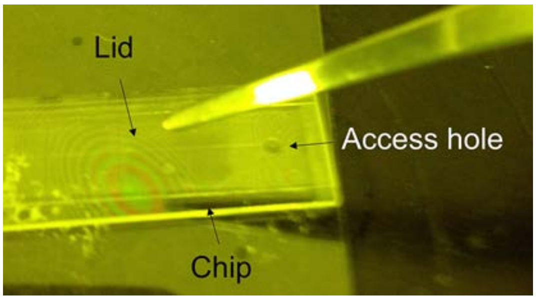

Figure 4.22: Adhesive bonding of SU-8 coated lid onto chip. The chip is on a hotplate with tweezers applying pressure to bring the lid into full contact.

The adhesive bonding technique allowed operation of devices 1 and 2 up to a channel back pressure of 5.18 bar ($Q = 0.2$ µl/s, $U_f = 0.33$ m/s). Further improvements to the bond strength can be made by fully planarizing the chip surface to maximise the contact area and also by applying more pressure during bonding using a heated screw press.

4.14 Complete devices fabricated

Using the processes described, three devices were fabricated with channel waveguides integrated with a straight, square cross section microfluidic channel. All devices had a waveguide core layer of 2 µm height with a range of waveguide widths from 2 µm to 9.2 µm. Device 1 and 2 were fabricated with mask designs for microfluidic channels 20 µm wide. The actual fabricated channels were measured on a microscope to have a width of 21.1 µm ±0.9 µm and 21.1 µm ±0.2 µm for device 1 and device 2 respectively. Device 3 was fabricated with a mask design for a microfluidic channel 14 µm wide. The actual fabricated channels were measured to have a width of 15.0 µm ± 0.2 µm. The depth of the microfluidic channels was measured using a Z-scope optical profiler to be 28.8 28.8 ±0.4 µm for device 1, 30.5 ±0.5 µm for device 2 and 30.0 ±0.4 µm for device 3. These measurements are summarised in Table 4.4. Figure 4.23 shows a photograph of device 2 without a microfluidic lid.

Table 4.4: Measured dimensions for waveguides and microfluidics of fabricated devices.

	Device 1	**Device 2**	**Device 3**
Waveguide height	2 µm	2 µm	2 µm
Waveguide width	2-9.2 µm	2-9.2 µm	2-9.2 µm
Microfluidic channel width	21.1 µm ±0.9 µm	21.1 µm ±0.2 µm	15.0 µm ±0.2 µm
Microfluidic channel height	28.8 ±0.4 µm	30.5 ±0.5 µm	30.0 µm ±0.4 µm

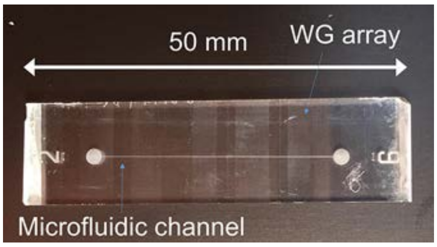

Figure 4.23: Photograph of device 2 without the microfluidic channel lid.

Devices 1 and 2 were used in the flow cytometry studies described in Chapter 6.

4.15 Conclusion

The dimensions of the microfluidic channel required for inertial focussing of 5.6 µm diameter beads were determined. The cross sectional dimensions of 30 µm high and 20 µm wide were determined from rules in the literature and the limitations of the fabrication processes to be used and operating pressures. The channel length required for the devices was determined to be 30 mm with an experimental study using PDMS test channels.

The fabrication process developed enables the production of monolithic, SiO_2 based microflow cytometer devices with fully integrated microfluidic channels and waveguides. The total processing time to produce a chip is 88 hours including all annealing and drying steps. Whilst this is longer than the production time for equivalent devices made with polymers (1 day) [25] the glass based production techniques allow robust optical circuits to be manufactured with the potential for inclusion of advance integrated optical components. The use of expensive cleanroom facilities can also be offset by producing large batches, for example at least 20 chips can be manufactured at a time on an 8” diameter wafer.

In summary the production process was as follows. The GeO_2:SiO_2 films forming the waveguide core were deposited with magnetron sputtering showing good thickness uniformity at 2 µm ± 0.050 µm with a refractive index of 1.469 ±0.0007 at a wavelength of 633 nm. The sputter deposition process at 200 ºC showed lower slab propagation losses than the process at 20 ºC suggesting the higher temperature process produces a film with fewer discontinuities and a more homogeneous refractive index. Annealing of the films in oxygen was shown to reduce the film refractive index and may increase propagation losses. ICP etching of the films protected by an e-beam deposited chrome hard mask was shown to produce waveguide structures with a width ±10% of the original mask design. Waveguides of 2.0 µm average width and 2.0 µm high were produced which are a good approximation of the single mode waveguide structures identified in the BPM simulations in Chapter 3. Additionally waveguides of up to 9.2 µm wide were produced allowing multimode operation. PECVD deposition of SiO_2 was shown to be a viable technique for the deposition of a thick cladding, up to 18 µm with a refractive index matching that of bulk SiO_2. Increasing the flow rate of N_2O relative to SiH_4 was shown to produce films of matching refractive index to bulk silica and alleviated stress induced cracking of the films. Planarization techniques were trialled as a means to reduce ridges in the cladding and chemical/mechanical polishing was shown to be successful at local flattening of ridges.

The microfluidic channels were fabricated using the same technique as the waveguides. The structures were defined with an e-beam deposited chrome hard mask and ICP etched to the required depth. Microfluidic channels were etched in multilayer substrates with integrated waveguides. The microfluidic channels produced were rectangular in cross section and could be made up to 30 µm deep and with any chosen width. A sealing technique using adhesive bonding of a glass coverslip lid on top of the microfluidic channel was shown to be effective up to a channel pressure drop of 5.18 bar ($Q = 0.2$ µl/s $U = 0.33$ m/s).

Three complete devices were fabricated, numbered 1-3. The next chapter describes the optical characterisation of the optical light path in these devices and then Chapter 6 describes the use of the devices for analysis of flowing beads.

CHAPTER 5

Characterisation of waveguide performance and illumination beam

5.1 Introduction

The design of the optical and fluidic components and the optimised fabrication processes required to realise the integrated optical flow cytometer devices have been described in the previous two chapters. Having fabricated the devices the optical light path including the waveguides and illumination beam were characterised. This allowed the theoretical design process to be verified and also informed the interpretation of the data from the flow cytometry studies which are described in the Chapter 6.

In this chapter first the modal behaviour of the narrowest 2.0 µm average width waveguide is assessed by imaging of the mode intensity profile. Then the power budget for the device is established in order to assess how optical attenuation may affect the function of the device. The real mode intensity profiles are compared to the simulated mode intensity profiles to verify if the simulated coupling efficiencies from Chapter 3 can be used as an approximation. The propagation loss of the waveguides are measured with two methods, the total waveguide insertion loss and by measuring the decay in scatter or autofluorescence along the waveguides. The insertion loss of the microfluidic channel is then measured and compared to the simulated insertion losses. Finally the shape of the beam launched into the microfluidic channel by the 2.0 µm wide and 9.2 µm wide waveguides are analysed by imaging the beam with fluorescent dye solution in the microfluidic channel. This would later clarify how beads were illuminated in the flow cytometry studies presented in Chapter 6.

5.2 Mode profiling

In Chapter 3, the BPM simulations determined the waveguide dimensions for single mode operation using the selected germania:silica material system. Chapter 4 showed waveguides of 2 µm high by 2 µm average width could be produced by conventional photolithography and etching. This section evaluates the mode intensity profile of these waveguides to confirm single mode operation and to measure the spotsize and compare this to the simulated spotsize. Mode profiling involves imaging the output of a waveguide and analysing the intensity distribution. Single mode operation is indicated by a Gaussian-like intensity distribution in the horizontal and vertical dimensions which does not change shape as the input radiation is scanned across the input facet.

The optical apparatus used to image the mode profile at wavelengths of 532 nm and 637 nm is shown in Figure 5.1. Light from either a laser diode pumped solid state laser at 532 nm (20 mW, OZ-2000-532-3.5/125-P-40-3S-3A-1-20, OZ optics, Canada) or a 637 nm laser diode (5mW iFLEX2000, QIOPTIQ, USA) was butt coupled into the polished end facet of the waveguide via a single mode fibre under polarisation control. The chip was imaged from above using a microscope and CCD camera (ORCA R2 Hamamatsu Photonics, Japan) to aid alignment during butt-coupling. The transverse intensity distribution at the end facet was imaged with a 20× 0.40 NA onto a CMOS camera (Moticam 2, Motic, HK).

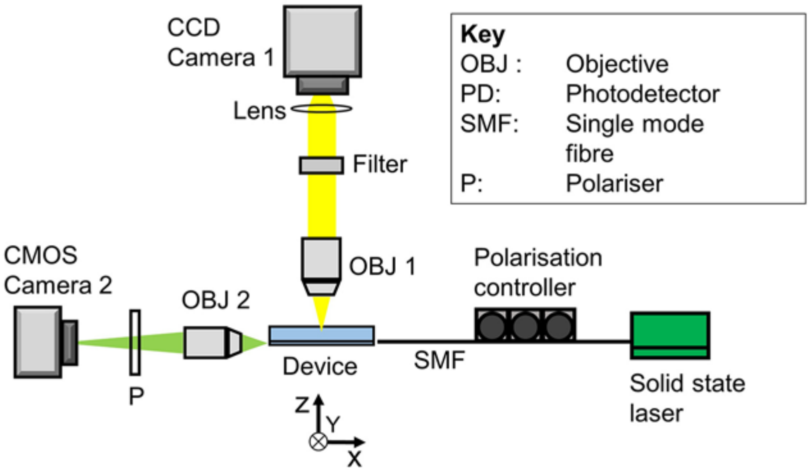

Figure 5.1 Schematic of the optical setup used to image the mode profile of the waveguides.

The known distance between adjacent waveguides within the same field of view was used to calibrate each image. Polarisation was confirmed by adjusting the polarisation controller to maximise the mode profile pixel intensity with a TE or TM orientated polariser in front of the camera [94]. The images for the mode profile were analysed in MATLAB to provide the intensity distribution in the Y and Z direction through the peak of the mode intensity distribution. A Gaussian curve, described by the following equation, was fitted to the data points for each intensity distribution.

$$I = I_0 \exp\left(-\frac{(x-b)^2}{2c^2}\right) \qquad 5.1$$

Where I_0 is the peak intensity, b is the peak position, c is the width related to the spotsize ω (Full width at 1/e^2 intensity) by $c = \frac{\omega}{4}$. The mode profiles were measured for the 2.0 µm average width by 2.0 µm high waveguide on device 1 before the microfluidic channel was etched.

First a test was performed to confirm that the waveguide was single moded by translating the input fibre in the Y and Z directions in order to attempt to excite higher order modes. Figure 5.2 and Figure 5.3 shows that when the input fibre position relative to the waveguide central axis, IP, was translated in Y and Z by 1 µm increments the mode intensity profile in Y and Z remained Gaussian-like with only the peak amplitude changing, indicating single mode operation at both wavelengths. These observations agree with the predictions made by the simulations in Chapter 3 that a 2.0 µm wide by 2.0 high waveguide would be single moded at both wavelengths.

a) Input fibre Y translation, Y profile **b)** Input fibre Y translation, Z profile

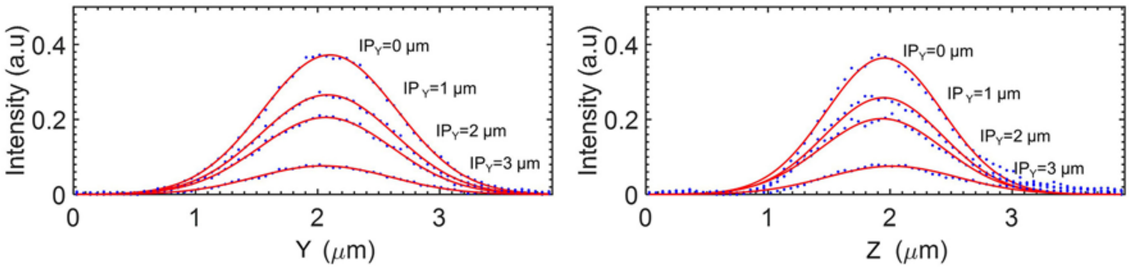

c) Input fibre Z translation, Y profile **d)** Input fibre Z translation, Z profile

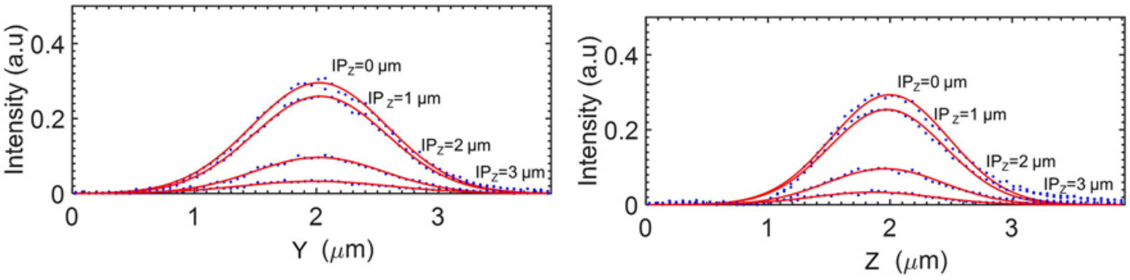

Figure 5.2: Confirmation of single mode operation at a wavelength of 532 nm by analysis of the mode profile cross section as the butt coupled input fibre is translated in 1 µm increments relative to the axial centre of the waveguide. Input fibre translation in Y direction showing (a) Y profile and (b) Z profile. Input fibre translation in Z direction showing (c) Y profile and (d) Z profile.

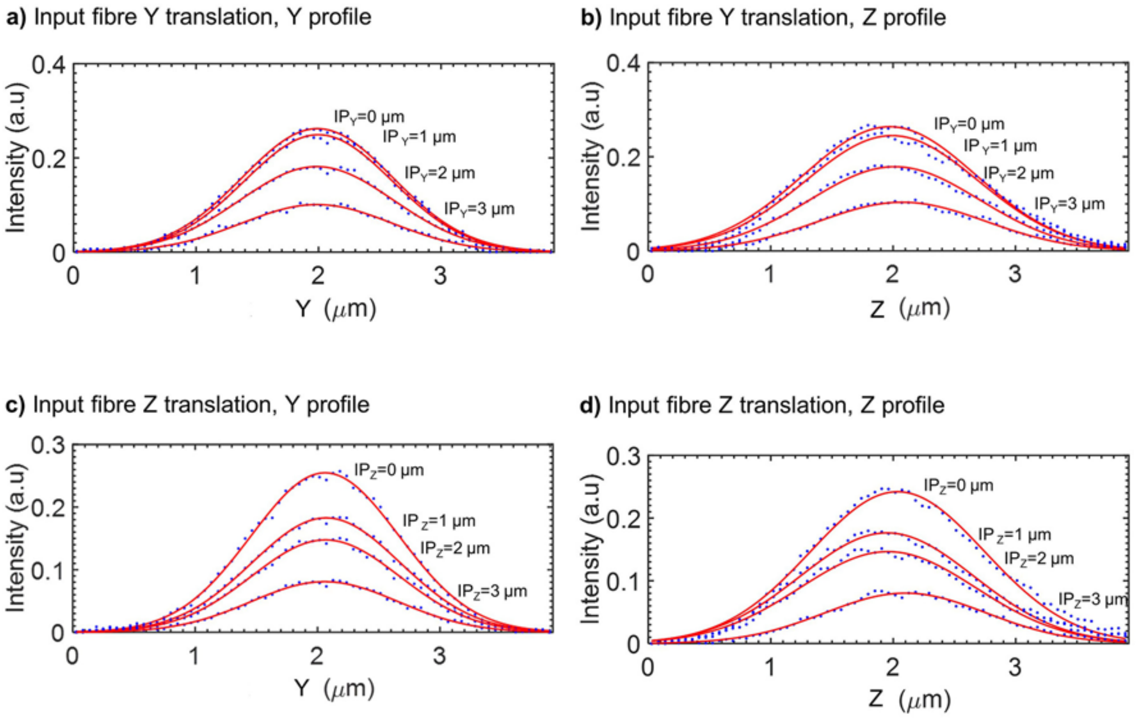

a) Input fibre Y translation, Y profile

b) Input fibre Y translation, Z profile

c) Input fibre Z translation, Y profile

d) Input fibre Z translation, Z profile

Figure 5.3: Confirmation of single mode operation at a wavelength of 637 nm by analysis of the mode profile cross section as the butt coupled input fibre is translated in 1 µm increments relative to the axial centre of the waveguide. Input fibre translation in Y direction showing (a) Y profile and (b) Z profile. Input fibre translation in Z direction showing (c) Y profile and (d) Z profile.

Figure 5.4 shows the TE mode intensity profiles for the 2.0 µm average width by 2.0 µm high waveguide for wavelengths of 532 nm and 637 nm. Changing the polarisation of the input fibre was shown not to change the mode profile dimensions significantly and so only the mode profiles for TE polarisation are presented.

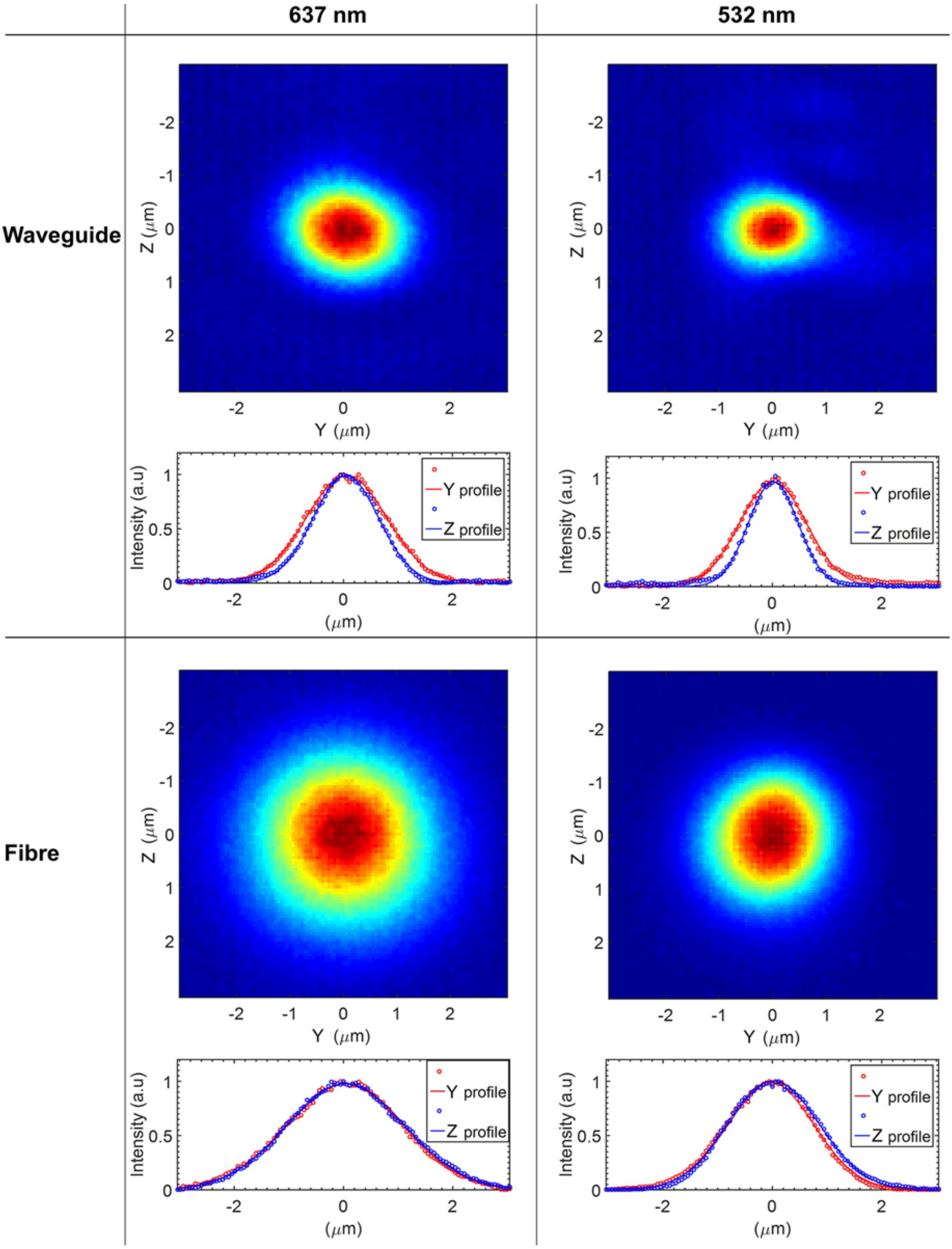

Figure 5.4: False colour images showing the mode profile for the fabricated 2.0 μm average width by 2.0 μm high channel waveguide at wavelengths of 532 nm and 637 nm with TE polarisation input. The cross-section in Y and Z through the mode peak is shown below each picture. Mode profiles of the single mode input fibres are also shown for comparison.

The cross sections in Y and Z at both wavelengths displayed in Figure 5.4, approximate a Gaussian distribution indicating that the fundamental mode is being predominately excited. Table 5.1

compares the measured waveguide spotsizes at the full width at $1/e^2$ intensity to the simulated spotsizes from Chapter 3 and the measured single mode fibre spotsizes. There is good agreement between the measured waveguide spotsize and the simulated waveguide spotsize in the Y direction at a wavelength of 532 nm. At a wavelength of 637 nm the spotsize is slightly larger in the Y direction than the simulated spotsize. For both wavelengths the measured spotsize is wider in Y than in Z which disagrees with the symmetrical spot suggested by the simulation results. The smaller dimensions in the Z direction may be due to a vertical tilt in the sample which could not be accounted for by the calibration measurement which is done horizontally. The spotsizes for the fibre are within the region stated by the manufacturer of 3.5 µm ±0.5 µm for 460HP [59] and 3.6 µ - 5.3 µm for SM600 [68].

Table 5.1 Measured spotsize in Y and Z for a 2.0 µm average width by 2.0 µm high channel waveguide at wavelengths of 532 nm and 633 nm with TE polarisation compared to simulated 2 µm wide by 2 µm high channel waveguide and measured single mode input fibres.

	532 nm		**637 nm**	
	ω_y (µm)	ω_z (µm)	ω_y (µm)	ω_z (µm)
Measured waveguide	2.5	1.8	3.0	2.4
Simulated waveguide	2.4	2.4	2.7	2.7
Measured single mode fibre	3.2	3.3	4.5	4.5

5.3 Device power budget

A power budget for the device was established in order to assess how optical attenuation in the device may affect the device signal to noise ratio for fluorescence and transmission based detection of flowing beads.

5.3.1 Coupling losses

The Coupling loss is the fraction of the optical power lost when light from a fibre or free-space beam is coupled into a waveguide. Coupling losses are due to two main factors, a mismatch in the intensity distribution of the modes supported by the waveguide and the modes of the input fibre and Fresnel reflections at interfaces such as air to glass or glass to water.

The waveguides dimensions and refractive index were designed to ensure a high coupling efficiency with a single mode fibre by ensuring a close spatial overlap in the mode intensity distributions of the fibre and the waveguide. In general the measured spotsizes and the simulated spotsizes for the waveguide showed good agreement. It was therefore expected that the real coupling efficiencies would approach the simulated coupling efficiencies of 0.90 and 0.84 for wavelengths of 532 nm and 633 nm respectively calculated in Chapter 3. These values correspond to coupling losses of 0.46 dB and 0.76 dB for wavelength of 532 nm and 633 nm respectively.

The real coupling efficiencies would be expected to be slightly lower due to diffraction across the air gap between the fibre and waveguide and Fresnel reflections at the waveguide interface. The proportion of light reflected at the air to waveguide interface, R_f, can be estimated with the Fresnel equation [95].

$$R_f = \frac{(n_1 - n_2)^2}{(n_1 + n_2)^2} \qquad 5.2$$

Where n_1 is the air refractive index and n_2 is the waveguide core refractive index. Using this equation the proportion of light reflected at the interfaces was calculated as 0.04 for both wavelengths.

Accounting for the Fresnel reflections the estimated coupling efficiencies for the realised 2.0 µm wide by 2.0 µm high waveguide were 0.86 and 0.79 for wavelengths of 532nm and 637 nm respectively. These values correspond to coupling losses of 0.66 dB and 1.02 dB for wavelengths of 532 nm and 637 nm respectively These high coupling efficiencies would ensure that the amount of stray light propagating in the substrate was minimised maintaining a high signal to noise ratio for fluorescence and transmission based detection.

5.3.2 Propagation losses

The propagation loss of a waveguide is the optical power lost per unit length and is usually expressed in dB/cm. Propagation loss is due to absorption of light by the waveguide material and cladding and by scattering of light at the core/cladding interface and at discontinuities in the core [95].

The insertion loss of a waveguide, L_I, can be used to calculate the propagation loss per unit length L_P, if the coupling losses, L_C, and the waveguide length, L_{WG} are known by using the following equation.

$$L_P = (L_I - L_C\,)/L_{WG} \qquad 5.3$$

The insertion loss of the 2.0 µm average width by 2.0 µm high waveguide was measured using the optical setup shown in Figure 5.5. The output light from the waveguide was collected by butt coupling a 50 µm diameter core multimode fibre with a numerical aperture of 0.22 which was optically connected to a photo detector power meter. The output power of the fibre coupled laser was measured by butt coupling the single mode fibre from the laser to the multimode fibre. The coupling loss for collection with a multimode fibre was considered to be negligible.

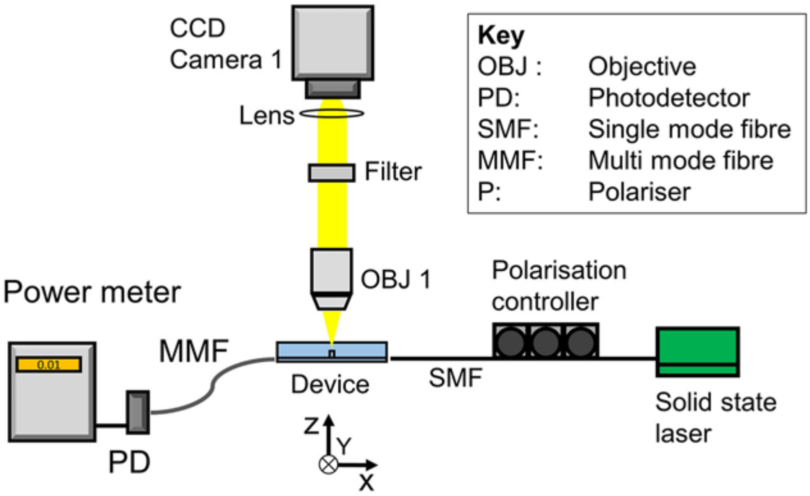

Figure 5.5: Optical setup used to measure the insertion loss and propagation loss of the waveguides.

The insertion loss in decibels is calculated by the following equation.

$$L_I(dB) = -10\log_{10}\left(\frac{P_W}{P_L}\right) \qquad 5.4$$

Where P_W is the waveguide output power and P_L is the fibre coupled laser output power. The measured insertion loss at a wavelength of 532 nm for the 2.0 µm wide by 2.0 µm high waveguide with a length of 2.12 cm was 31 dB. This insertion loss corresponds to a propagation loss of 14.3 dB/cm. The insertion loss of the waveguide at 637 nm was not measured but was expected to be lower due to reduced scattering loss at the longer wavelength.

Propagation losses were also calculated by measurement of the light intensity along the length of the waveguide originating from either scattered light or autofluorescence. The microscope apparatus shown in Figure 5.5 was used to image scattered light from the waveguides and used a 5× 0.15 NA objective and a top mounted CCD camera. The images were post processed in MATLAB. First the image was background subtracted using an image of the same field of view but with the laser switched off. Then the pixel intensity orthogonal to propagation direction was summed to get the power in pixel counts (P_{px}) and converted to power in decibels (P_{dB}) using the equation.

$$P_{dB} = 10\log_{10}(P_{px}) \qquad 5.5$$

Images were taken along the lengths of each waveguide and the measured propagation losses were averaged to give a mean propagation loss with a reported error of 1 standard deviation. Propagation losses were measured in this manner for the 2.0 µm average width and 9.2 µm average width waveguides on device 1 at wavelengths of 532 nm and 637 nm and for both input polarisations.

At an input wavelength of 532 nm a significant amount of autofluorescence was excited along the length of the waveguide as light was still visible with a long pass 542 nm filter (BLP01-532R-25, Semrock, USA) in front of the CCD camera. This was thought to arise from metal impurities in the germania:silica core or the PECVD silica cladding. At an input wavelength of 637 nm there was not significant autofluorescence as the light was cut out when a long pass 645 nm filter (BLP01-633R-25, Semrock, USA) was inserted in the microscope. For both light originating from scattering and from autofluorescence, the intensity is directly proportional to the optical power interacting with the scattering/autofluorescing body and so both can be used to measure propagation loss.

Figure 5.6(a) and (b) show the false colour images of the autofluorescence along a section of the 2.0 µm wide waveguide excited by input light at a wavelength of 532 nm for both input polarisations. Figure 5.6(c) and (d) shows the power in decibels, calculated from the MATLAB processing, plotted against the X position along the waveguide for both polarisations. The power lost per unit length was taken as the gradient of the linear fit.

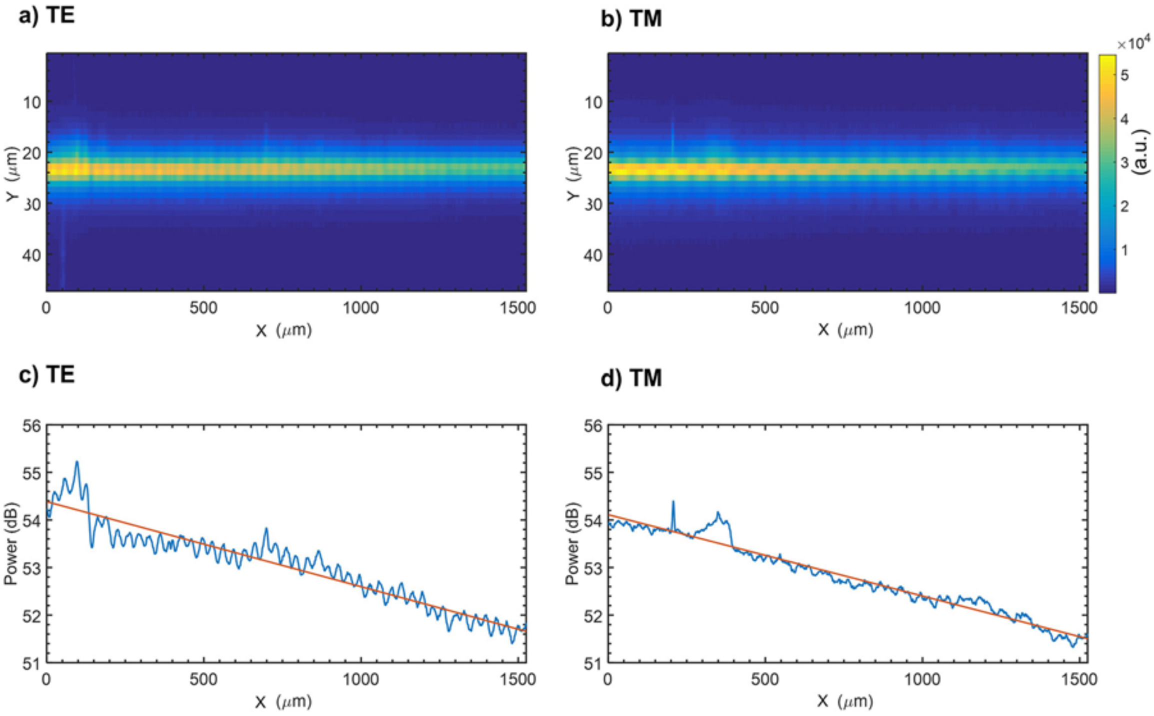

Figure 5.6 : Top row: False colour image of the autofluorescence from a 2 µm wide waveguide excited by input light at a wavelength of 532 nm for (a) TE polarisation and (b) TM polarisation. Bottom row: Autofluorescence power versus propagation length (X direction) measured from each image.

Figure 5.7 (a) and (b) show the false colour images of the scattered light along a section of the 2.0 µm wide waveguide with input light at a wavelength of 637 nm for both input polarisations. Figure 5.6(c) and (d) show the power in decibels, calculated from the MATLAB processing, plotted against the X position along the waveguide for both polarisations. Sample images for the 9.2 µm wide waveguide were also taken but are not presented.

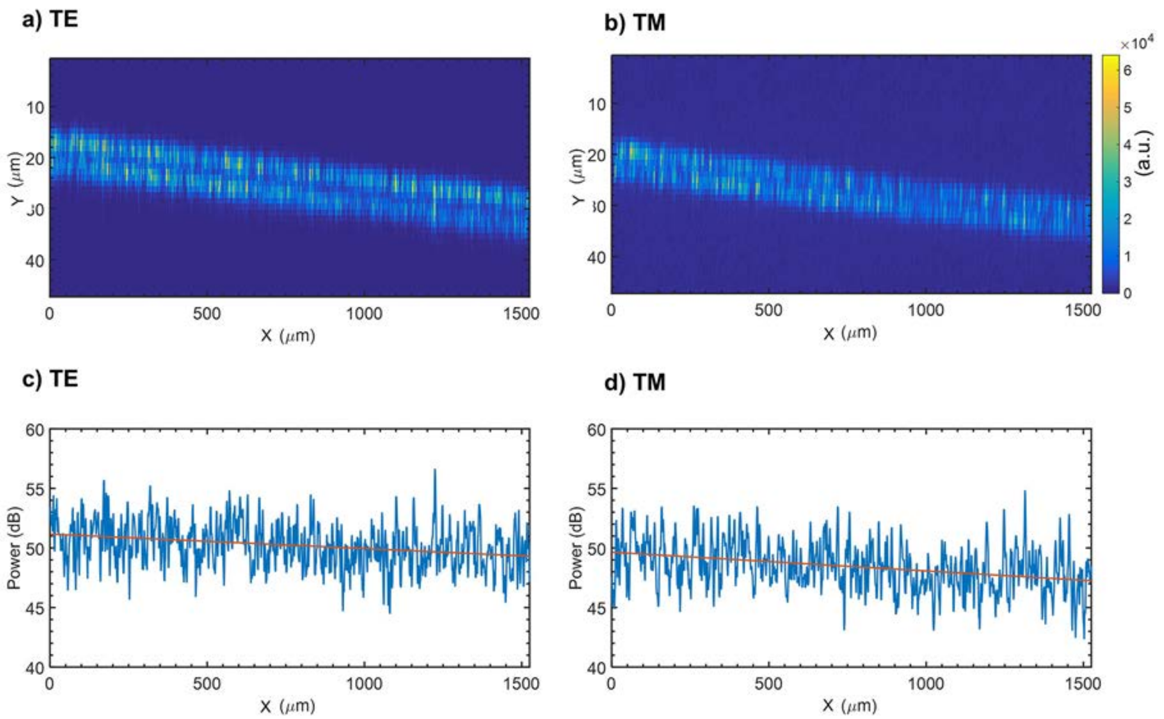

Figure 5.7: Top row: False colour image of the scattered light from a 2 µm wide waveguide excited by input light at a wavelength of 637 nm for (a) TE polarisation and (b) TM polarisation. Bottom row: Scattered light power versus propagation length (X direction) measured from each image.

Table 5.2 summarises the measured propagation losses for the 2.0 µm wide and 9.2 µm wide waveguides at both polarisations.

Table 5.2: Propagation loss measured by image analysis of waveguide autofluorescence (532 nm) or scatter (637 nm). Error represents 1 standard deviation of the mean. NM = not measured.

	532 nm				**637 nm**			
	TE		**TM**		**TE**		**TM**	
WG Width	dB/cm	±	dB/cm	±	dB/cm	±	dB/cm	±
2.0 µm	-15.5	1.6	-14.2	2.5	-14.8	5.4	-11.0	3.4
9.2 µm	-13.9	2.7	-14.8	1.7	NM	-	NM	-

The propagation loss for the 2.0 µm waveguide measured by microscope imaging was close to the propagation loss calculated using the waveguide insertion loss. The input polarisation showed no significant effect on the propagation loss within the measurement error for both widths of waveguide measured. The input wavelength also showed no significant effect on propagation loss within the measurement error for the 2.0 µm wide waveguide. The losses at an input wavelength of 637 nm for the 9.2 µm wide waveguide were not measured. If the measurement error was reduced it would be expected that the longer wavelength should exhibit lower propagation loss due to reduced scattering. The waveguide width did not significantly affect the measured propagation loss at 532 nm.

The measured propagation losses are in the region of 13.9 -15.5 dB/cm and are high for waveguides. The high losses may be due to roughness in the side wall of channel waveguides or due to inclusions or discontinuities in the germania:silica film. The autofluorescence exhibited at an input wavelength of 532 nm will also contribute to light absorption during propagation. A further study of the deposition parameters, annealing and etch process for the waveguides would reveal a good course of action to reduce the propagation losses but was outside the scope of this work. The relatively high propagation losses did not affect function of the devices as fluorescence based and transmission based detection of flowing beads was still achieved with a high signal to noise ratios as described in Chapter 6.

5.3.3 Microfluidic channel insertion loss

The microfluidic channel insertion loss is the proportion of optical power lost in transmission from the input waveguide to the output waveguide across the microfluidic channel. A low microfluidic channel insertion loss is desirable to ensure enough optical power is collected by the output waveguide to allow transmission based detection of flowing beads with a high signal to noise ratio.

The insertion loss incurred by the 21.1 µm wide microfluidic channel filled with water ($n_{532\mathrm{nm}}$= 1.334) in device 1 was measured using the same setup, and a similar technique to that used to measure propagation loss. An image was taken of the waveguide autofluorescence with the excitation and collection waveguide in the same field of view, bisected by the microfluidic channel. As with the propagation loss measurements, the pixels in the image orthogonal to the propagation direction were summed to give the autofluorescence power versus propagation length for both waveguides. The power in pixel counts was converted to dB using equation 5.5. Separate linear fits were then applied to the input waveguide power data and the output waveguide power data. The insertion loss in dB was calculated as the difference between the last point on the line of best fit of the input waveguide and the first point on the line of best fit of the output waveguide. Using this technique it was only possible to measure the insertion loss at a wavelength of 532 nm as at a wavelength of 637 nm, strong scattering occurs at the microfluidic channel obscuring measurement. The insertion loss of the 21.1 µm wide microfluidic channel were measured for the 2.0 µm wide waveguide and for the 9.2 µm waveguide at both polarisations.

Figure 5.8 shows the autofluorescence power in decibels versus propagation length measured for 2.0 µm and 9.2 µm wide waveguides at both input polarisations. All plots show a sharp dip in power coinciding with the microfluidic channel. The insertion loss for the 2.0 µm wide waveguide was 2.75 dB and 3.46 dB for TE and TM inputs respectively. The insertion loss for the 9.2 µm wide waveguide was 3.61 dB and 3.58 dB for TE and TM input polarisations respectively.

a) 2.0 µm wide WG, TE polarisation **b) 2.0 µm wide WG, TM polarisation**

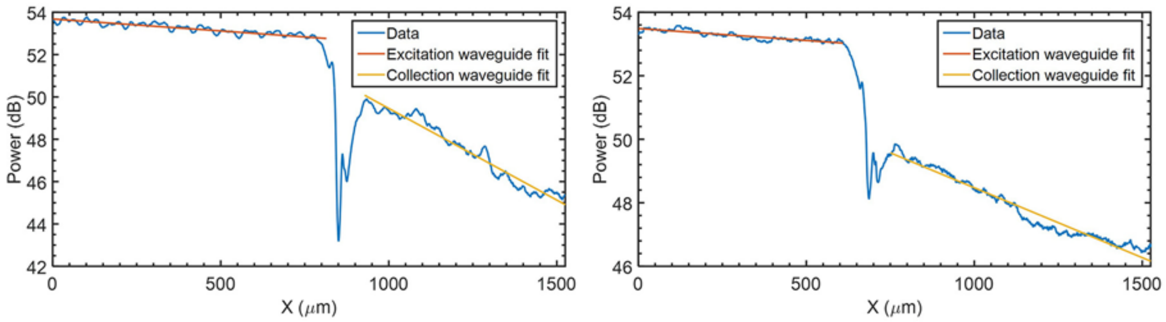

c) 9.2 µm wide WG, TE polarisation **d) 9.2 µm wide WG, TM polarisation**

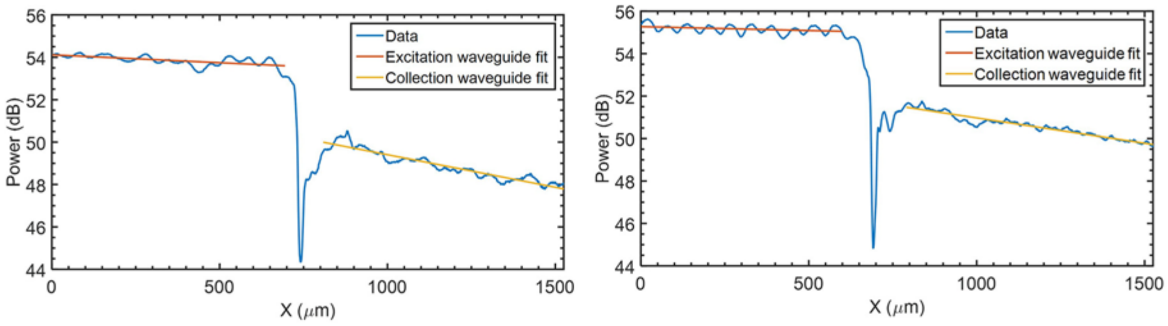

Figure 5.8: Analysis of the insertion loss caused by a 21.1 µm wide microfluidic channel at a wavelength of 532 nm. All plots show autofluorescence power versus X distance along waveguide measured for a 2.0 µm wide waveguide with (a) TE and (b) TM input polarisations and for a 9.2 µm wide waveguide with (c) TE and (d) TM input polarisations.

These measured insertion losses are higher than the simulated insertion losses for a ~20 µm wide channel which were simulated as 1.0 dB and 0.6 dB for 2 µm and 10 µm width waveguides respectively. The increased insertion losses are likely to be partly due to Fresnel reflection and most significantly scattering at the fluid/waveguide interfaces which were not accounted for in the simulations. The input polarisation only appeared to significantly affect the insertion loss for the 2.0 µm waveguide and may have been due to features on the end facets of this waveguide. The waveguide width did not significantly affect the insertion loss. The channel coupling losses would be expected to be higher if the fluidic channel were filled with air ($n_{532nm} = 1$) instead of water as the increased refractive index contrast would cause greater beam divergence. .A common observation was that the propagation loss of the output waveguide was greater than the output waveguide as shown by the steeper gradient of the linear fit. This may be due to the rapidly decaying leaky modes which could be launched in the collection waveguide.

Overall the insertion loss incurred by the microfluidic channel was low enough to allow coupling efficiencies of 0.53 and 0.45 for 2 µm and 9.2 µm wide waveguides respectively. These coupling efficiencies were expected to allow enough light to be collected by the output waveguide for transmission based detection of flowing beads with a high signal to noise ratio. Detection with a high signal to noise ratio was demonstrated in the flow cytometry studies described in Chapter 6.

5.3.4 Device insertion loss

The insertion loss of a device including the microfluidic channel was measured using the same technique used for the waveguide insertion loss and was 19.59 dB. The total losses calculated from all the components of the light path (Table 5.3) are slightly lower than the measured device insertion loss. The difference is likely to be due to slight differences in the real coupling losses compared to the simulated values used.

Table 5.3 Losses for each component of optical light path compared to measured device insertion loss

Component	**Loss (dB)**
Input coupling	0.66
Input WG (L= 0.5cm)	7.40
Fluidic channel	2.75
Output WG (L= 0.5cm)	7.40
Output coupling loss	0.66
Total loss	18.86
Device insertion loss	19.59

5.4 Beam shape in the microfluidic channel

The shape of the beam was imaged in the microfluidic channel in order to inform the interpretation of fluorescence and transmission signals produced by flowing beads in the studies described in Chapter 6. Imaging of the beam at a wavelength of 532 nm crossing the microfluidic channel was achieved by pumping a solution of the fluorescent dye R-phycoerythrin (0.4 µM in distilled water with 0.2% v/v Tween20 surfactant) through the channel and imaging from above with the microscope and CCD camera shown in Figure 5.1. The beam shape for the 2.0 µm and 9.2 µm wide waveguides were measured for TE polarisation input. The full width at $1/e^2$ maximum intensity was measured by taking an intensity profile using MATLAB in the Y direction at the left and right equilibrium positions of flowing beads. These equilibrium positions were identified experimentally as 5 µm from the left and right channel wall respectively as discussed in more detail in Chapter 6.

Figure 5.9 shows images of beams crossing the microfluidic channel, as revealed by the fluorescent solution, for the 2.0 µm and 9.2 µm wide waveguides. Figure 5.9 (a) shows the narrowest beam width was at the output of the 2.0 µm wide waveguide, the beam widths were 4.3 µm and 5.9 µm for the right and left equilibrium position. The XY plane beam dimensions for the 2 µm width waveguide provide a useful approximation for the XZ plane beam dimensions of all widths of waveguide fabricated, considering they all have a height of 2 µm. The widest beam produced was from the multimode 9.2 µm wide waveguide which yielded a width of 9.3 µm at the right and 9.9

µm at the left positions. Figure 5.9 (b) shows that this multimode waveguide launched a dual-lobed intensity distribution across the channel, which was believed to be due to modal interference in the waveguide due to excitation of multiple modes in the waveguide.

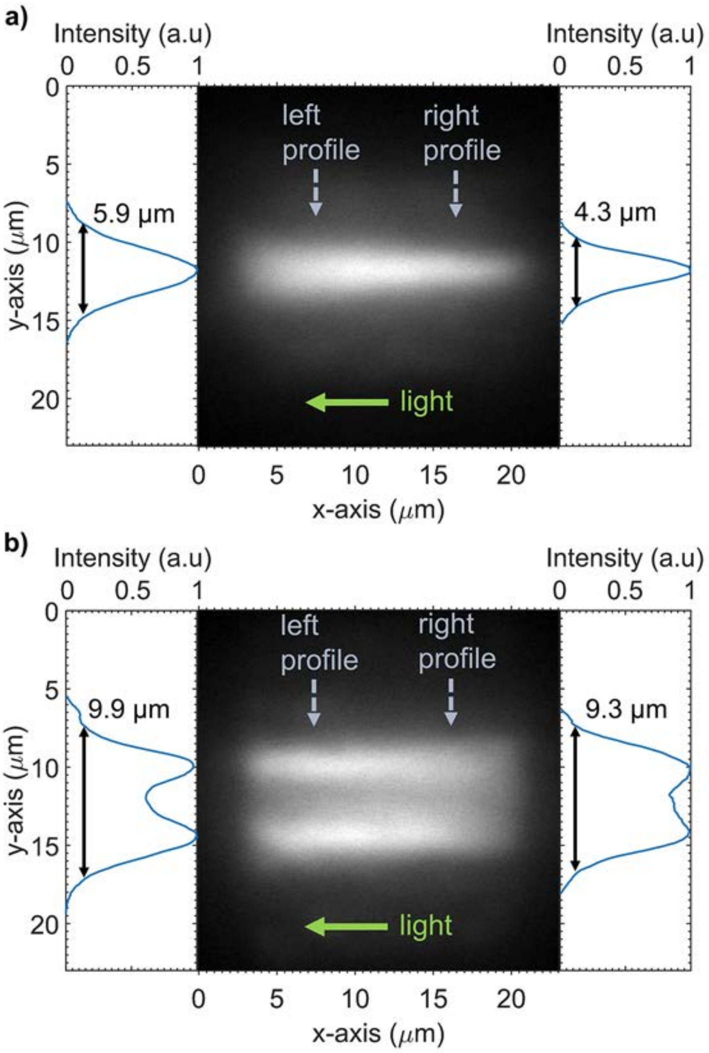

Figure 5.9: Fluorescence microscope images of the beam crossing the microfluidic channel with accompanying profiles showing the intensity distribution parallel to the Y axis for the right and left inertial focussing position (a) 2.0 µm wide single mode waveguide and (b) 9.2 µm µm wide multimode waveguide.

The width of the beam in the Y direction determines the illumination time and intensity for a bead flowing through the beam. The choice of waveguide width to be used for the flow cytometry studies was based upon maximising the signal to noise ratio for the mode of measurement. For the measurement of the total fluorescent energy emitted from a flowing bead using a CCD camera as descirbed in detail in Chapter 6, the 9.2 µm wide waveguide was chosen. The wider beam allows the flowing beads to be illumnated for longer without saturation of the CCD camera pixels, resulting in a greater total fluorescence energy measured, and therefore higher signal to noise ratio. In addition the 9.2 µm wide waveguide was used for the transmission measurements as it was expected to produce transmission signals with longer durations which were thought to allow greater accuracy for measurement of bead velocity.

5.5 Conclusion

The optical characterisation of the light path in the fabricated integrated optical microflow cytometer devices has been described. The 2.0 µm wide by 2.0 high waveguide fabricated was shown to be single mode at both 532 nm and 637 nm as predicted by the simulations in Chapter 3. These waveguides were shown to produce Gaussian like mode intensity profiles with spotsizes of 2.5 µm and 3.0 µm at wavelengths of 532 nm and 637 nm respectively.

The power budget for the fabricated devices was established to assess the impact of optical attenuation of device performance. As the measured spotsizes were similar to the simulated spotsizes, the coupling efficiency for the 2.0 µm wide by 2.0 high waveguide was approximated by the simulation coupling efficiencies from Chapter 3 adjusted for Fresnel reflection of 0.86 and 0.79 for wavelengths of 532 nm and 633 nm respectively. These high coupling efficiencies were expected to minimise the light propagating in the substrate ensuring a low background signal for fluorescence and transmission based detection of flowing beads. The propagation losses for the waveguides were measured by two methods, from the waveguide insertion loss and by measuring light decay along the waveguide. The propagation losses were shown to be from 13.9-15.5 dB/cm for the 2.0 µm and 9.2 µm wide waveguides. The insertion loss incurred by the 21.1 µm wide microfluidic channel was measured at 2.75 dB and 3.6 dB for the 2.0 µm wide and 9.2 µm wide waveguides for input light at a wavelength of 532 nm with TE polarisation. These insertion losses were expected to be low enough to allow transmission based detection of flowing beads with a high signal to noise ratio.

The shape of the beam launched by the input waveguide across the microfluidic channel was revealed by fluorescence imaging. The smallest beam width which could be produced was from the 2.0 µm wide waveguide and were 4.3 µm and 5.9 µm for the right and left equilibrium positions. The largest beam width was from the 9.2 µm wide waveguide which produced beam widths of 9.3 µm at the right and 9.9 µm at the left equilibrium positions. The wider beam was deemed to be the more suitable for fluorescence energy quantification using a microscope and CCD camera as it would allow a greater total illumination power without saturating the CCD camera ensuring a high signal to noise ratio. The wider beam was also thought to allow transmission based measurement of bead velocity with greater accuracy.

CHAPTER 6

Flow cytometry studies using fabricated devices

6.1 Introduction

Previously Chapter 3 and Chapter 4 described the design and fabrication of the integrated optical microflow cytometer devices. This chapter evaluates the performance of the fabricated devices according to the design specification with three studies. First, the extent to which inertial focussing causes confinement of the flowing beads in the microfluidic channel of device 1 was assessed by fluorescence streak imaging, measuring the count rate of the beads and measuring the signal variation. Second, device 2 was used to measure the fluorescence from beads incubated with human TNFα standard. Third, device 2 was used for transmission based detection of flowing beads.

6.2 Characterisation of inertial focussing of beads in device

6.2.1 Introduction

The straight, square rectangular cross section microfluidic channel design was designed to confine beads by inertial focussing into two equilibrium positions centred on the long faces of the channel cross section. This was expected to cause a greater proportion of beads to flow through the beam and also to reduce signal variation by minimising variation in the total excitation power intersecting with each bead. To test the effectiveness of the channel design, the extent to which inertial focussing was causing confinement of the bead flow streams was assessed using fluorescence streak imaging, measuring the count rate of the beads and measuring the fluorescence signal variation of the beads. The fluorescence signals from inertially focussed beads in the left and right equilibrium positions were also compared as these were expected to be different due to the different beam illumination beam profiles at these positions.

6.2.2 Materials and Method

Characterisation of the inertial focussing of beads was conducted with device 1, which had a microfluidic channel with a width of 21.1 μm ±0.9 μm and a depth of 28.8 μm. The input waveguide used to illuminate the flowing beads was positioned 17 mm downstream from the entrance of the microfluidic channel and was 9.2 µm wide by 2.0 µm deep. The widest waveguide was used as although it was multimode, it provided a wider illumination area and thus a longer illumination time. This allowed a greater amount of total fluorescence energy to be collected without saturating the pixels in the CCD image.

The device was placed in the optical apparatus shown in Figure 6.1 with the etched side of the substrate facing down so that all imaging was done through approximately 1 mm of substrate. The region of the microfluidic channel illuminated by the input waveguide was imaged with a 20× objective onto a cooled CCD camera (ORCA-R2, Hamamatsu, Japan) through a 542 nm long pass filter to cut out stray pump light. The fluidic input tubing was attached to the chip by pressure sealing a flat bottomed ferrule connection against the input reservoir hole. Light from a 20 mW fibre coupled, diode pumped solid state laser at 532 nm (OZ-2000-532-3.5/125-P-40-3S-3A-1-20, OZ optics, Canada) was butt-coupled into the input waveguide using a single mode fibre under polarisation control. Light leaving the output waveguide was collected with an objective lens and focussed through a TE oriented polariser and then through a pinhole onto a photodetector attached to a power meter. The total transmitted power was monitored for separate data acquisitions to allow normalisation of fluorescence measurements between data sets. The polarisation was set to TE by manipulating the polarisation controller until the output power was maximum [94].

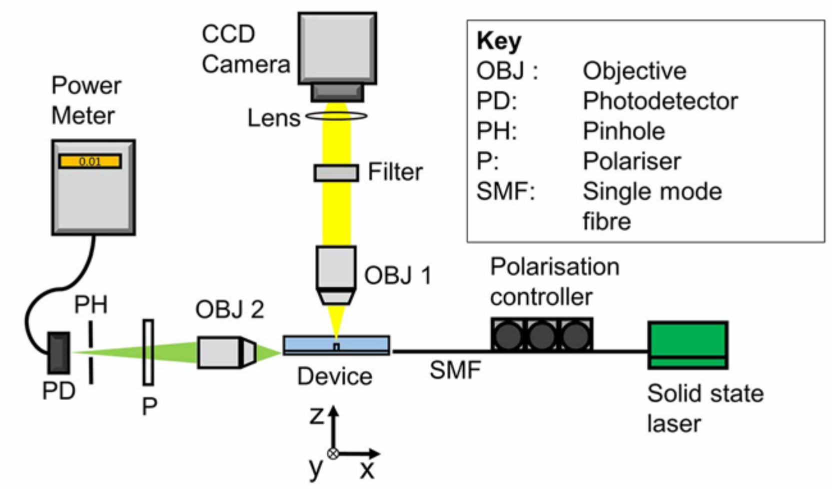

Figure 6.1: Schematic of the optical set up for imaging fluorescence from flowing beads.

The beads used to characterise the inertial focussing were fluorescence intensity calibration beads for fluorescence microscopy (Inspeck Orange, ThermoFisher, USA) [96]. These polystyrene beads are 5.6 µm in diameter and are designed to produce repeatable fluorescence emission signals at a wavelength of 560 nm under excitation light at a wavelength of 532 nm. The beads were suspended at a concentration of 20 beads/µL in 0.2% Tween20, 1% bovine serum albumin (BSA), phosphate buffered Saline. (PBS). The low bead concentration was intended to minimise the chance of coincident signals and the Tween20 surfactant and BSA were included to prevent aggregation and nonspecific binding to surfaces.

The bead suspension was pumped to the chip using a syringe pump through a 10 µm pore size filter to remove clusters and then through tubing coupled to the chip input reservoir. A video of the channel area illuminated by the waveguide was recorded at 79.5 frames per second with an image exposure time of 0.0125 s and an interval of 79 µs between frames when no data was being recorded. As the transit time of each bead was much shorter than the exposure time, each image of a streak of florescence left by a bead represented the total fluorescence energy emitted by that bead. Figure 6.2 shows example frames from a video acquisition showing the region of the microfluidic channel illuminated by the input waveguide when no bead is present in the beam (Figure 6.2(a)) and when a bead passes leaving a fluorescent streak (Figure 6.2(b)). The resultant fluorescence energy collected from passing beads was calculated by post processing in MATLAB. A rectangular region of interest, shown in Figure 6.2(b), was defined around the area in the image illuminated by the waveguide and all the pixel values within this box were summed, for each frame, giving the total fluorescence energy collected in pixel intensity units.

The origin of pixel intensity units is as follows, each photon incident on a CCD pixel during the exposure time is converted into an electron by the photoelectric effect. Some photons do not produce electrons and so a pixel array is assigned a quantum efficiency value which is the ratio of the number of electrons stored in a pixel to the number of incident photons during the acquisition. The charge accumulated in each pixel is directly proportional to the number of incident photons during the exposure time provided that the pixel does not become saturated. At the end of the exposure time the charge is shifted from each line of the pixel array onto a linear register which is then readout through an output amplifier which converts the charge packet for each pixel into a proportional voltage and applies a gain factor. Following this an analogue-to-digital converter (ADC) converts the voltage form each pixel into a binary code which is readable by the computer. The bit depth of the ADC defines the resolution with which each pixel intensity value can be represented, for example a 16-bit digital value will be on a scale from 0 to 65536 pixel intensity units. A CCD array can therefore be used to measure the total light energy incident on a pixel as long as the as the quantum efficiency, gain factor, ADU conversion factor and bit depth are known [97].

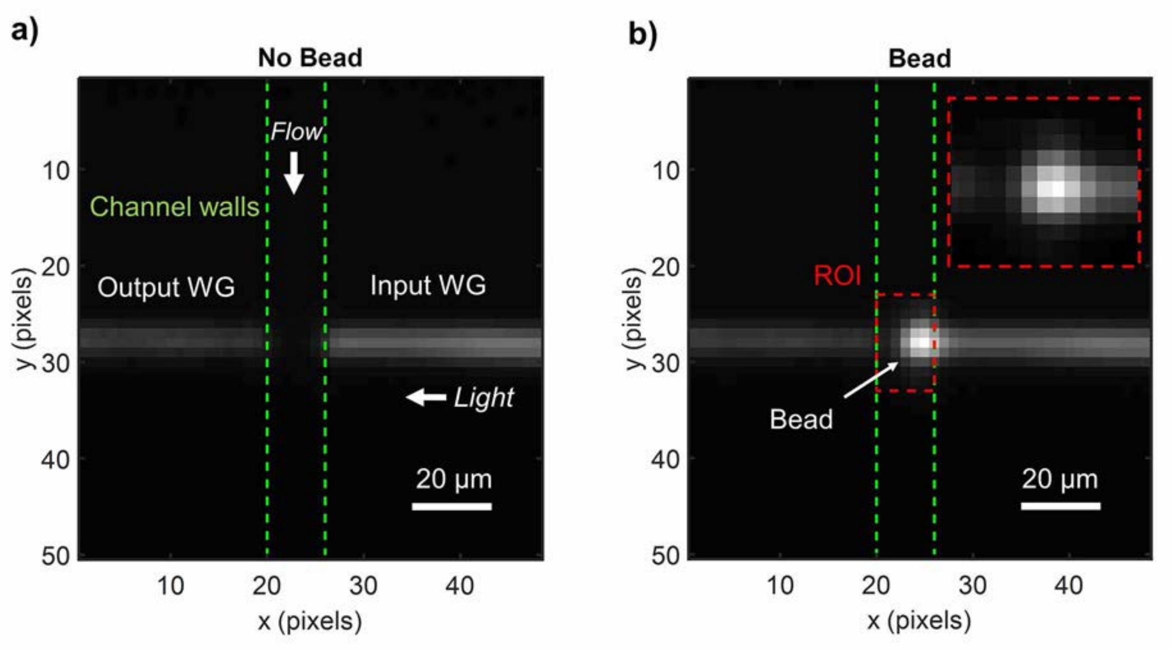

Figure 6.2: Individual frames from video taken on a the fluorescence microscope of the region of the microfluidic channel illuminated by the input waveguide when (a) no bead is passing through the beam and (b) there is fluorescence from a bead passing through the beam within the region of interest (ROI).

The contribution to the signal from chip autofluorescence and intrinsic background in the camera was eliminated by subtracting the summed pixel intensity of the region of interest when only buffer solution was flowing. The background corrected, summed pixel intensity value was converted to energy in joules using equation 6.1 where E is energy in Joules, I_{px} is 16 bit pixel intensity, F is conversion factor of 0.275 electrons/analogue-to-digital-unit, E_p is photon energy at 578 nm of 3.44×10^{-19} J/photon, G is the camera gain, Q_λ is the quantum efficiency of 0.7 electrons/ photon at 578 nm [98].

$$E = \frac{I_{px} F E_p}{G Q_\lambda} \qquad 6.1$$

The baseline background fluorescence was recorded when buffer alone was flowing. The standard deviation of this background fluorescence was ~0.5 fJ. Any fluorescence energy values which exceeded a threshold of ten standard deviations of the of the background fluorescence above the baseline were deemed to be bead signals, with lower values discarded as noise. This process is shown in Figure 6.3. To prevent the high peaks from distorting the interpretation of the data, peaks from images where two beads are visible were excluded from the subsequent data analysis.

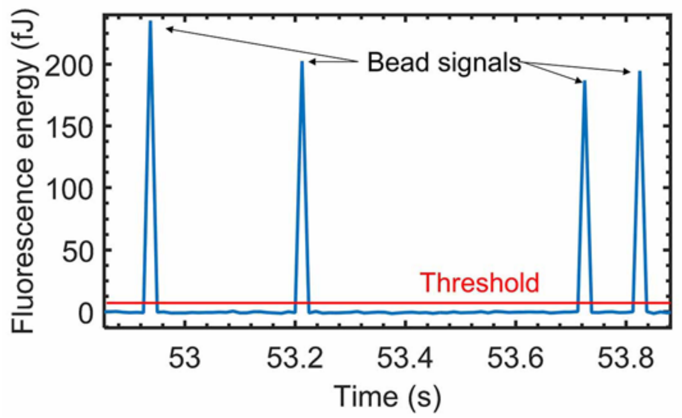

Figure 6.3: Fluorescence energy collected by the CCD camera from beads flowing through the beam. Showing the threshold at 10 × Standard deviation of the signal when only buffer is flowing. Peaks above the threshold are from fluorescence from beads.

Two flow rates were investigated, 0.1 µl/s ($U = 0.17$ m/s) and 0.2 µl/s ($U = 0.33$ m/s). Inertial focussing parallel to the short face of the microfluidic channel cross section (x-axis) was examined using pixel by pixel summing of all the video frames containing a bead into a single image to give the lateral distribution of beads passing through the beam. Inertial focussing parallel to the long face of the microfluidic channel cross section (z-axis) was assessed by comparing the count rate of beads detected to the maximum possible count rate determined by the bead concentration and flow rate.

6.2.3 Results and discussion

Due to a high back pressure, running the chip at flow rates higher than 0.2 µl/s resulted in delamination of the lid sealing the microfluidics and so the inertial focussing behaviour of beads could only be investigated up to this flow rate. In addition blocking of the channel caused by bead aggregates occurred quickly at higher flow rates and required the chip to be dismantled, cleaned and resealed. Strategies for overcoming the operational limitations caused by high back pressure and blocking are covered in section 7.2. At 0.2 µl/s the particle Reynolds number for the device channel dimensions was calculated using equation 2.2 to be 1.25 which is above the threshold of 1 required for inertial focussing to take place.

The 2 µm width waveguide was shown to excite fluorescence from flowing beads however using the wider 9.2 µm waveguide produced approximately twice the fluorescence energy as the bead was illuminated for around twice the time. The difference in fluorescence signal was due to the use of a single CCD image acquisition to integrate the entire fluorescence power produce by a bead over time. Another commonly used metric for fluorescence signal is the peak fluorescence power [99] which can be measured using a fast photodetector such as an avalanche photodiode. In this case the 2 µm waveguide would produce the same peak power as the wider waveguides if the same illumination intensity were used. Measurement of the fluorescence energy using a CCD camera was adequate for the flow cytometry studies conducted in this work and so the wider 9.2 µm waveguide was used throughout to excite fluorescence.

Figure 6.4 shows the combined fluorescence image from 612 individual fluorescent beads which flowed through the beam during the video acquisition time driven at a flow rate of 0.2 µl/s ($U = 0.33$ m/s). The image shows that the beads are tightly confined into left and right equilibrium positions centred 5 µm ± 1 µm from the microfluidic channel walls which indicates that inertial focussing is well developed parallel to the short face of the channel (X axis). This agrees with the mechanism suggested by Zhou et al that particle migration to equilibrium positions occurs quickly parallel to the short face of the channel [54]. The dual lobed intensity distribution in the Y direction observed previously in Figure 5.9 is again revealed in Figure 6.4 as the beads produce fluorescence directly proportional to the excitation intensity as they pass through the beam. The greater fluorescence intensity observed for the right equilibrium position is due to a bias for beads to pass on the right side of the channel with a ratio of 2:1. This bias was likely to be due to asymmetrical feeding from clumps of beads forming in the input reservoir as the bias was shown to switch sides for separate experiments.

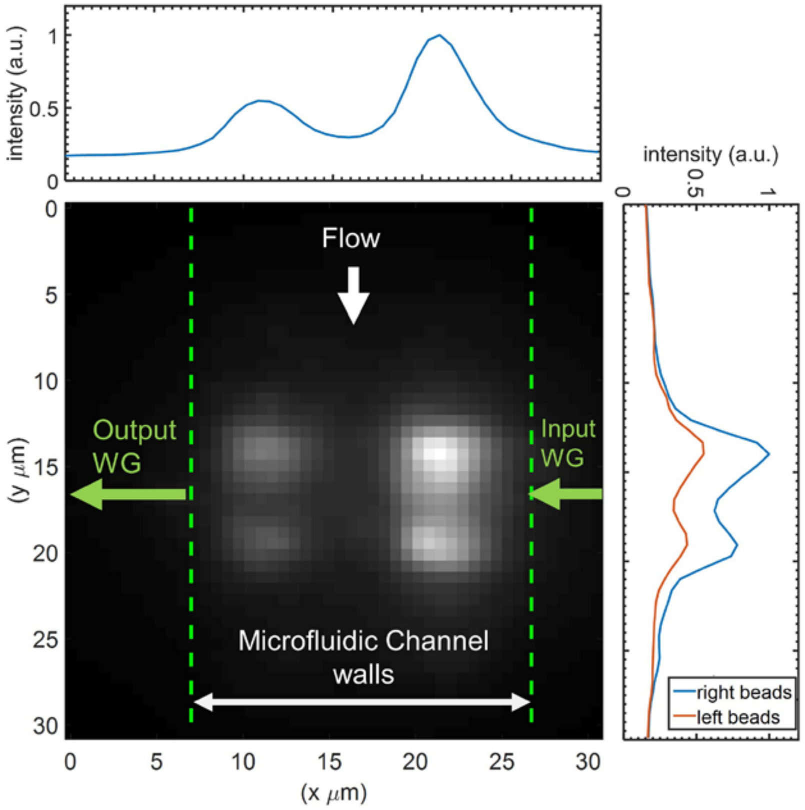

Figure 6.4: Fluorescence microscope image showing the summed fluorescence from 612 beads which have flowed through the beam driven at a flow rate of 0.2 µl/s. Intensity in the y direction is proportional to the excitation beam intensity.

The measured bead count rate at a flow rate of 0.2 µl/s was 142 beads/minute which is 59% of the maximum count rate determined by the input bead concentration and flow rate. If flowing beads were randomly distributed in the Z dimension then only 28% of beads would be expected to flow through the beam based on the assumed dimensions of the beam in the XZ plane. This shows that inertial focussing parallel to the long face of the channel is occurring but is not fully developed because the analysis region is positioned 17 mm downstream and so there has not been enough downstream distance for all particles to reach the equilibrium positions [49], [100]. Reducing the flow rate to 0.1 µL/s ($U = 0.17$ m/s) reduced the proportion of beads flowing through the beam to 35 % which also confirms the presence of inertial focussing at the higher flow rate. It is predicted using equation 2.5 that using a higher flow rate of 0.35 µl/s would lead to fully developed inertial focussing at the analysis region causing all beads flow through the beam.

The fluorescence energies for beads flowing at 0.1 µl/s and 0.2 µl/s were compared. Figure 6.5 (a) and (b) show the fluorescence energy collected by the CCD camera for beads pumped at flow rates of 0.1 µl/s and 0.2 µl/s. The action of inertial focussing is clearly demonstrated by the reduction in the variation of the bead signal amplitudes at the higher flow rate. The reduction in signal variation can also be clearly seen by comparing the histograms of the fluorescence energy measured at each flow rate in Figure 6.5 (c) and (d). The histogram for the 0.2 µl/s flow rate in Figure 6.5 (d) shows a clear peak representing the modal fluorescence energy whilst there is no clear peak in fluorescence energy for the 0.1 µl/s flow rate. Table 6.1 summarises the fluorescence energy statistics obtained for each flow rate. The coefficient of variation (CV), for the measured fluorescence energy is lower for the higher flow rate of 0.2 µl/s. At the right equilibrium position the CV of the fluorescence energies is reduced from 58% to 40% when the flow rate is increased from 0.1 µl/s to 0.2 µl/s. At the left equilibrium positon the CV of the fluorescence energies is reduced from 92 % to 40% when the flow rate is increased from 0.1 µl/s to 0.2 µl/s. This observation confirms that inertial focussing in both dimensions acts to reduce the fluorescence signal variation as intended by the design of the device.

The measured fluorescence energy for the beads flowing at left and right equilibrium positions were compared for the 0.2 µl/s flow rate. Figure 6.5 (d) shows the histogram of the fluorescence energies of all the beads from this sample and compares the fluorescence energies for the right and left beads. Table 6.1 presents the key statistical data. The median fluorescence energy for individual beads passing on the right hand side, close to the input waveguide, at 205 fJ is ~12% greater than those from beads passing on the left (178 fJ). This is believed to be due to diffraction in the Z direction resulting in less of the incident pump power being intersected by beads on the output (left) side of the channel. The coefficient of variation for the right and left bead position are the same at 40% indicating that beam dimensions have a minimal effect on signal variation. Due to the significant difference between the left and right bead signals, it was decided that quantitative comparisons of fluorescence signals between different samples of beads should use values from the same side equilibrium position. It is expected that the lowest achieved fluorescence signal CV of 40% in device 1 may be reduced further by using higher flow rates to further confine the beads in the Z direction.

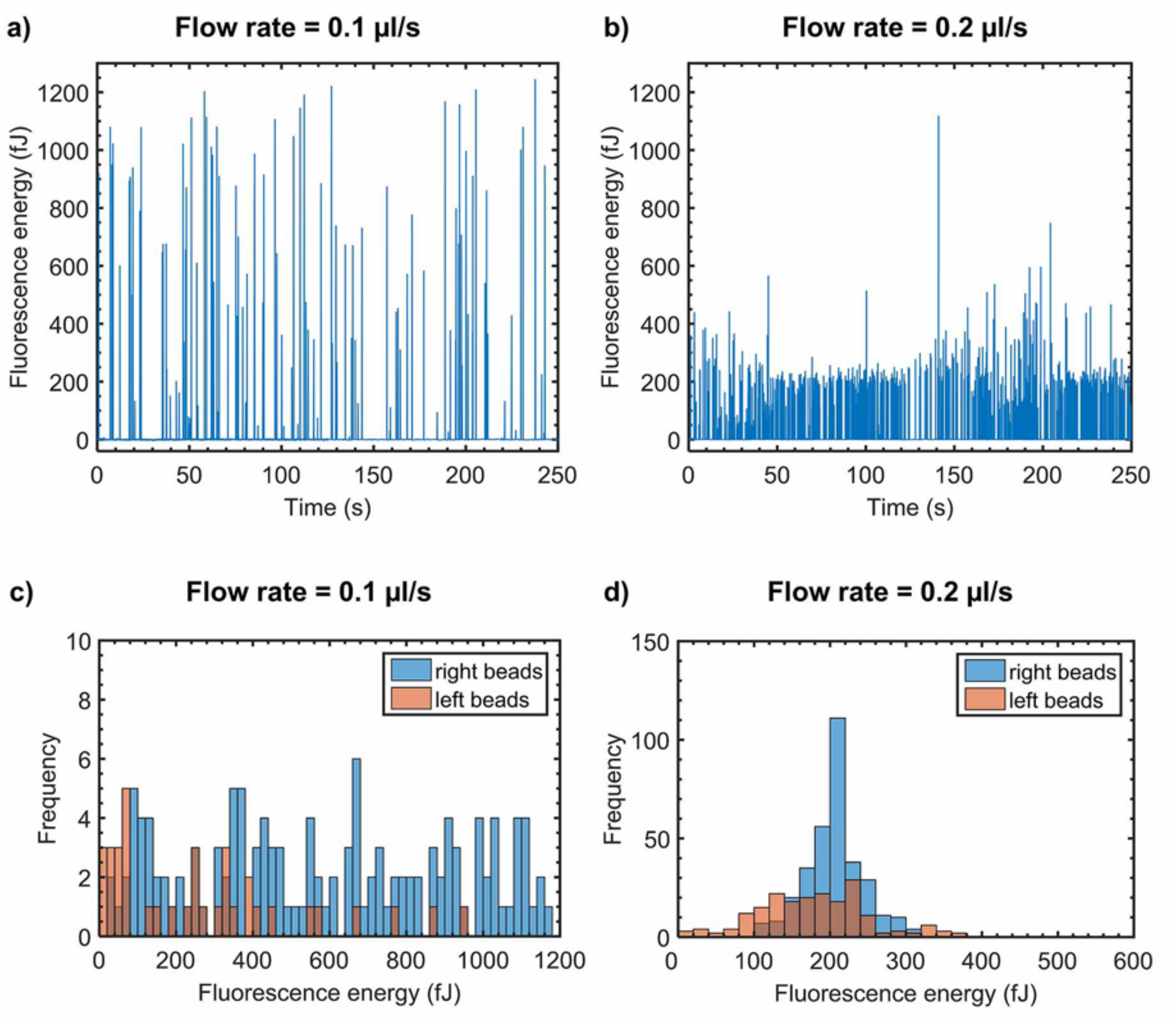

Figure 6.5: Top row: Fluorescence energy collected by the CCD camera for beads flowing at (a) 0.1 µl/s and (b) 0.2 µl/s through the beam from a 9.2 µm wide waveguide. Bottom row: histograms comparing the fluorescence energies of beads flowing through the beam on the right (blue) and left (pink) side of the channel for flow rates of (a) 0.1 µl/s and (b) 0.2 µl/s

Table 6.1: Fluorescence energy collected by the CCD camera for flowing calibration beads at flow rates of 0.1 µl/ and 0.2 µl/s and for beads passing at left or right equilibrium positions for each flow rate.

	0.1 µl/s		**0.2 µl/s**	
	Left position	**Right position**	**Left position**	**Right position**
Mean fluorescence energy (fJ)	270.63	584.40	179.28	203.95
Median fluorescence energy (fJ)	242.07	572.83	178.42	204.53
Standard deviation (fJ)	249.99	337.74	72.28	81.23
CV (%)	92.37	57.79	40.31	39.83

6.3 Device immunoassay for human TNFα

6.3.1 Introduction

The microflow cytometer developed in this project was designed to measure the fluorescence from beads used in a bead-based immunoassay, providing an alternative platform to the traditionally used macro scale flow cytometers. To demonstrate this application device 2 was used to measure the fluorescence from beads used in an immunoassay for the human version of the cytokine, tumour necrosis factor alpha (TNFα). TNFα is a small cell signalling protein which is primarily involved in the regulation of immune cells during systemic inflammatory responses. TNFα was chosen as an example analyte as there is a broad interest in its role in the biological and medical research community. TNFα, amongst other inflammatory cytokines, has been identified as an important biomarker for the investigation of chronic neurodegenerative diseases in which chronic inflammation plays a role such as Alzheimer’s disease [101]-[104] and Parkinson’s disease [105], [106]. TNFα has also been implicated in the response of neurons after a stroke [107] and may be a useful biomarker for lung cancer [108]. Typical circulating levels of TNFα in healthy individuals are in the pg/ml range and these levels can spike by up to 3 orders of magnitude into the ng/ml range during an acute inflammatory response [109] and are present at slightly elevated levels in the 10s of pg/ml range during chronic inflammation [104]. Due to the role of TNFα as part of a wider signalling network of cytokines it is advantageous for researchers to measure the concentration of multiple cytokines at once and so many studies rely on the multiplex analysis capabilities of bead based immunoassays [32], [110].

The immunoassay kit used for this study was the magnetic Luminex performance assay kit for human TNFα (Cat number LUHM000, R&D systems, USA) [111]. The immunoassay beads used by the kit are 6 µm diameter superparamagnetic microparticles which can be retained in the reaction tube with a magnet whilst the supernatant is removed allowing efficient removal of unbound species after each incubation step. The beads are made from a polystyrene core coated a with a shell doped with ferrite (Fe_3O_4) nanoparticles which impart the superparamagnetic properties. As the concentration of ferrite in the shell is < 50%, the beads are still transparent [112].

They also have the same fluorescence properties of standard Luminex immunoassay beads, the reporter signal quantifies the bound analyte and is excitable at a wavelength of 532 nm and emits fluorescence around 565 nm, while the classification signal, designating the analyte, is excitable at 635 nm and emits fluorescence at 670 nm and 700 nm. The aim of the study was to measure the reporter fluorescence of beads incubated with a range of known concentrations of TNFα standard in buffer in order to produce a standard curve. This standard curve could then be used in future studies to measure the TNFα concentration in serum samples. An example standard curve provided by the manufacturer is shown in Figure 6.6. Reporter calibration beads (CAL2, Luminex Corp., USA) are used to normalise between bead fluorescence measurements taken at different times allowing for drift in the device illumination conditions and detector responses. These beads emit a repeatable median fluorescence intensity (MFI) which is verified by the manufacturer. The MFI of the calibration beads corresponds to a virtual concentration of analyte at 847pg/mL which has been added to the curve on Figure 6.6. In Figure 6.6 the right Y axis scale displays the fluorescence intensity relative to the calibrator bead value as a percentage.

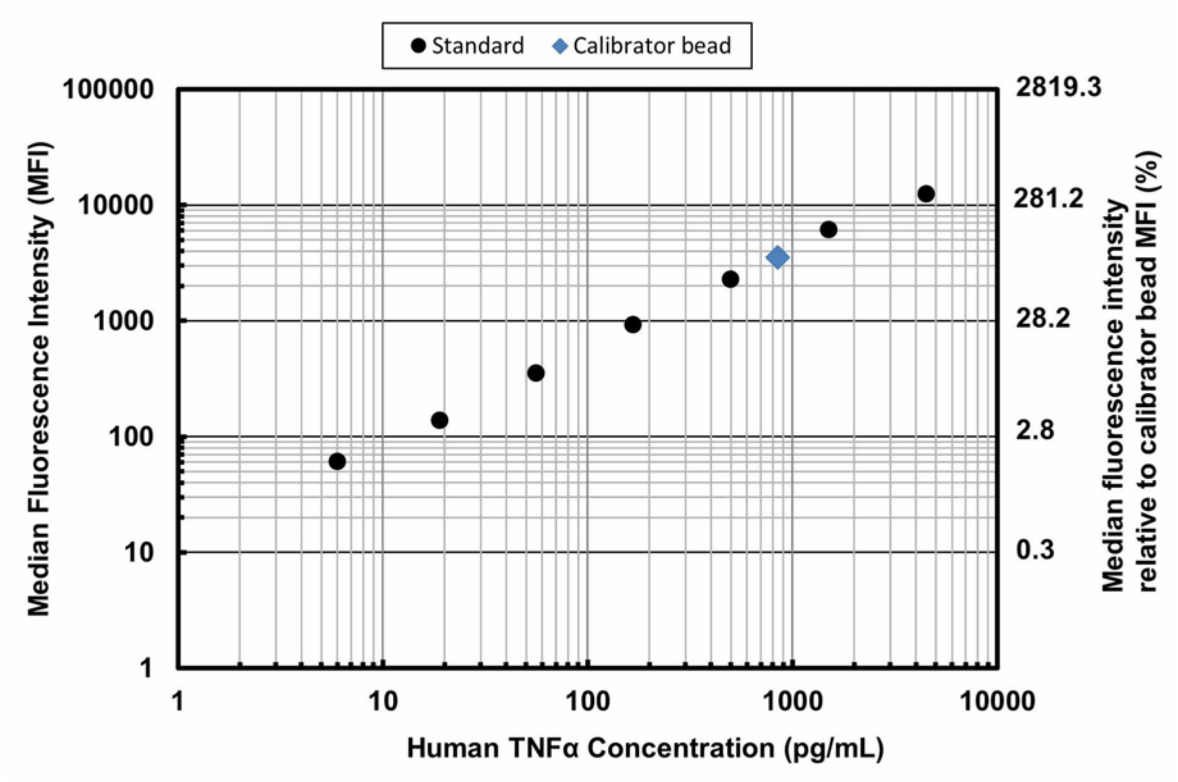

Figure 6.6: Standard curve taken from the product data sheet for the Magnetic-Luminex® Performance Assay Human TNF-α Kit [111]. The MFI value for the reporter calibrator beads are shown on the plot to illustrate the relative fluorescence of the beads within the scale of the calibration range. The right Y axis scale is the fluorescence intensity relative to the calibrator beads as a percentage.

6.3.2 Materials and method

The reagents and equipment used to perform the bead-based immunoassay for human TNFα are detailed in Table 6.2. The details of most of the reagents used in the kit are proprietary but concentrations and compositions are given if known.

Table 6.2: Reagents and equipment used for the bead based immunoassay for human TNFα (Performance Assay Human TNF-α Kit Cat number LUHM000, R&D systems, USA) [111].

Reagent/equipment	**Description**
Magnetic microparticles	Magnetic microparticles, 6 µm diameter, coated in anti-hTNF-α which acts as the capture antibody in the sandwich style immunosassay.
Biotin-antibody	Biotin-anti-hTNF-α which binds as the detection antibody in the sandwich style assay.
Cytokine standards 1 and 2	A mixture of recombinant human cytokines including Human TNF-α in buffered protein base. The cytokine standards were serially diluted to produce samples containing TNFα at 154 pg/ml and 4150 pg/ml
Wash Buffer	Buffer for washing microparticles.
Calibrator diluent	Buffered protein base to dilute the human recombinant cytokine standard.
Microparticle diluent	Buffered protein base for diluting magnetic microparticles.
Biotin Antibody diluent	Buffered protein base for diluting detection antibody.
Streptavidin-PE	Streptavidin phycoerythrin conjugate. Binds to the biotin on the biotin-antibody, fluorescently labelling the beads.
1.5 mL tubes	To hold sample for reaction
Magnetic separator tube rack	Tube rack for 1.5 mL tubes with a magnet at the one side of the bottom of the tube.
Vortex mixer	Horizontal orbital vortex mixer with 4.5 mm diameter orbit with holder for 1.5 mL tubes. For mixing samples.
Precision pipette	For measuring and dispensing reagents.

Table 6.3 details the protocol for the immunoassay. The immunoassay was performed following the manufacturer’s protocol for the human TNFα assay kit however the incubation volumes used were 5 × larger than the recommended 50 µl to allow a 200 µl sample of beads to be injected into the microflow cytometer device. A smaller sample injection volume would have been possible if a parallel injection loop system was incorporated into the fluidic system however the equipment was not available at the time of the study. To account for the altered mixing dynamics of the larger volume the incubation time for the microparticles with the TNFα sample was extended to 5 hours to ensure full binding. The magnetic microparticles from the kit were incubated with human TNFα standards at 154 pg/ml, 4150 pg/ml and a blank buffer sample as a background reference.

Table 6.3: Protocol used for the bead based immunoassay for human TNFα.

Step	**Protocol**
1.	250 µL of each TNFα standard dilution were added to separate tubes containing 250 µL of microparticle suspension and then placed in a rack on a horizontal vortex mixer with 4.5 mm diameter orbit at 800rpm for 5 hours at room temperature.
2.	The suspension was washed to remove the free TNF-α using the magnetic tube rack. The tubes were place in the rack and left for 5 minutes to allow the magnetic microparticles to form a pellet on the side wall at the bottom of the tube. Whilst still magnetised the liquid in the tube was removed completely with a pipette. The tubes were removed from the magnet and the beads are resuspended in 500µL of wash buffer. The process is repeated three times and on the final time no wash buffer was added.
3.	250 µL of biotinylated anti-hTNFα was added to each tube and incubated for 1 hour at room temperature at 800 rpm.
4.	The wash step was repeated to remove free biotinylated antibody
5.	250 µl of Streptavidin-PE was added to each tube, which were then incubated for 30 minutes at room temperature at 800 rpm.
6.	The wash step was repeated to remove free Streptavidin PE.
7.	The particle were resuspended in 500 µL of wash buffer and incubated on the shaker at 800 rpm for 2 minutes. They samples were then ready for analysis

Device 2 was used to measure the fluorescence of the beads. This device had a microfluidic channel 21.1 µm ± 0.1 µm wide by 30.5 µm ± 0.5 µm deep. The input waveguide used was 9.2 µm wide by 2.0 µm deep and located 22 mm downstream from the microfluidic channel entrance. The same free space fluorescence collection system was used as for the measurement of fluorescence from calibration beads in section 6.2. Both the reporter calibration beads and magnetic microparticles from the assay kit were at a final concentration of 25 beads/µl in the assay wash buffer and were flowed through the device for analysis at 0.1 µl/s. The lower flow rate had to be used to avoid delamination of the chip over the extended operation time. Reporter calibration beads (CAL2, Luminex Corp., USA) were run through the device before the immunoassay beads in order to check beads were being inertially focused.

6.3.3 Results and discussion

All fluorescence data were taken from beads passing through the right equilibrium position as a greater number passed on this side. The fluorescence from calibration beads was measured on the device first to establish the extent to which inertial focussing was occurring in device 2. Inertial focussing in the X direction was confirmed with fluorescent streak imaging, showing confinement into left and right equilibrium positions. The measured bead count rate was 113 beads/minute which was 75% of the expected count rate at a concentration of 25 beads/µl and a flow rate of 0.1 µl/s. This showed that inertial focussing in the Z dimension was confining most of the beads to flow through the beam. The proportion of beads to flow through the beam was greater for device 2 than previously observed in device 1 even though a lower flow rate of 0.1 µl/s was used with device 2. The CV measured for the calibration beads with device 2 was lower at 29% compared to 40% in device 1 also indicating increased Z confinement in device 2. The increased Z confinement in device 2 may be due to the slightly greater h/w aspect ratio of 1.45 in device 2 compared to 1.36 in device 1 [49]. In device 2 the greater aspect ratio channel may have caused beads to migrate primarily to the equilibrium positions centred at the long face of the channel resulting in a greater proportion of beads flowing through the beam. In device 1 the lower aspect ratio channel may allowed stable equilibrium positions centred on the short faces of the channel which would have reduced the number of beads which could migrate to the equilibrium positions centred on the long faces of the channel and resulted in a lower proportion of beads flowing through the beam. In addition the input waveguide in device 2 is position 5 mm further downstream compared to device 1 which allows more time for beads to migrate to equilibrium positions, increasing the confinement.

Figure 6.7 compares the histograms of the fluorescence energies measured for the calibration beads and immunoassay beads. The histogram for the calibration beads in Figure 6.7(b) shows a clear modal peak confirming inertial focussing. The frequency distribution of the fluorescence energy measured for the sample incubated with 154 pg/ml TNFα in Figure 6.7(a) shows a possible 3 modal peaks. The lowest peak at 2.5 fJ is likely to be due to some fluorescent debris remaining in the sample. The peaks at 27.5 fJ and 62.5 fJ are most likely from the fluorescent beads, and the higher peak may be due to fluorescence from two beads being collected in the same frame during the integration time. As the beads would have passed on same side, the algorithm for detection of a double signal would not have excluded these points from the data. In future work a fluorescence collection system which uses a data acquisition rate in the MHz range would be expected to almost eliminate the occurrence of coincident signals. The histogram for the fluorescence energy measured from the 4150 pg/ml sample in Figure 6.7(c) shows a lower total number of beads (n=43) were measured compared to the other samples. This was attributed to beads being lost during the immunoassay wash step and so only a weak modal peak at 7.5 fJ is observed.

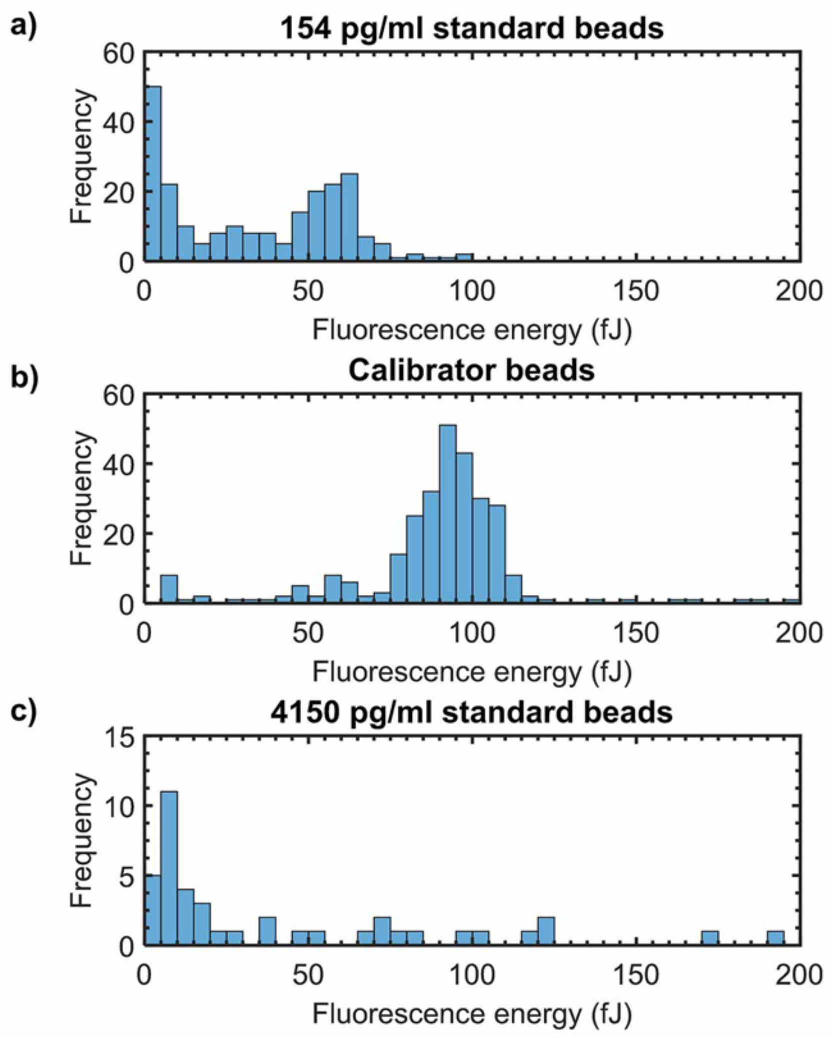

Figure 6.7: Histograms of fluorescent energies collected by the CCD camera for bead samples incubated with TNFα standard at concentrations of (a) 154 pg/ml and (c) 4150 pg/ml and also (b) reporter calibrator beads.

Figure 6.8 shows the median fluorescence energies measured using microflow cytometer device 2 for the two TNFα standard concentrations and also including the data point for the calibration beads plotted at a position equivalent to a bead sample incubated with 847 pg/ml TNFα standard. The right Y axis scale shows the median fluorescence energy relative to the calibrator bead sample MFI as a percentage for easy comparison. Median fluorescence values were plotted as the median is distorted less by outliers. Table 6.4 details the statistical data for these data points. The median fluorescence value measured for the 154 pg/ml sample was 37% of the calibration beads median fluorescence value at 35 fJ compared to 93 fJ. The calibration curve given by the manufacturer [111] predicts that the relative fluorescence intensity from an assay for 154 pg/ml TNFα should be 26% of the calibrator intensity. The high signal value may be due to the inclusion of double signals in the data. If the middle modal peak from Figure 6.7(a) at 27.5 fJ were used to represent the data for the 154 pg/ml sample then the relative fluorescence intensity would be 29% and would be closer to the value measured by the manufacturer. The median fluorescence value measured for the

4150 pg/ml sample was 20% of the calibrator and so was much lower than the 352% percent given by the manufacturers calibration curve. The low number of beads measured for the 4150 pg/ml sample limits the confidence in the measured fluorescence for this sample and a repeat study would have to be conducted. It is possible that at high antigen (TNFα) concentrations there may still be unbound antigen in the bulk and this will reduce the valency of the free floating detection antibody resulting in fewer detection antibodies binding to the beads. This effect, known as the ‘hook’ effect [113] has been documented in Luminex flow cytometers and microflow cytometers [18].

The immunoassay beads show a higher CV of 74% and 124% compared to the calibrator beads at 29% which indicates that the immunoassay protocol has increased the signal variation. In future experiments, variation could be reduced by using the same sample volume as the manufacturer in a 96 well plate format which would allow duplicated data points to be measured. A parallel study on a luminex flow cytometer would also allow comparison and verification of results.

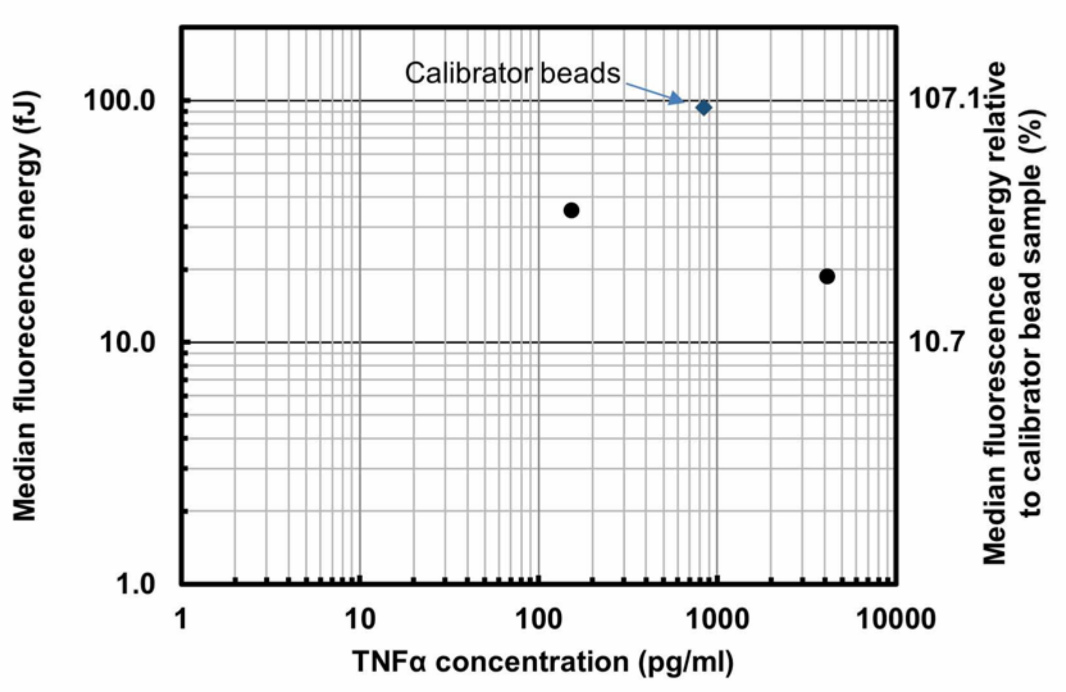

Figure 6.8: Standard curve for fluorescence measurement of beads incubated with human-TNFα standards at 154 pg/ml and 4150 pg/ml using microflow cytometer device 2. Also showing the fluorescence measurements for the calibrator beads plotted at a position equivalent to a bead sample incubated with 847 pg/ml TNFα. The right Y axis scale is the fluorescence energy relative to the calibrator beads as a percentage.

Table 6.4: Fluorescence energies measured at the right equilibrium position for bead samples incubated with TNFα standard and also calibrator beads.

TNFα standard Concentration	**Mean (fJ)**	**Median (fJ)**	**Standard deviation (fJ)**	**CV (%)**
Blank 0 pg/ml	0	0	1	0
154 pg/ml	34	35	26	74
Calibrator beads (equivalent to 847 pg/ml)	89	93	26	29
4150 pg/ml	51	19	64	124

The high CV for the standard samples has prevented a quantitative analysis of the dose-response relationship. The large signal variation was attributed to the immunoassay protocol and not the device which measured a CV at 29% for calibration beads which is only 9% higher than another inertial focussing fluorescence microflow cytometer in the literature [114]. Strategies for reducing the signal variation caused by the immunoassay protocol are discussed in Chapter 7. A reduced CV and a greater range of standard concentrations and repetitions will be needed in future experiments to plot a calibration curve. The detection of fluorescence from immunoassays beads incubated with TNFα at concentrations as low as 154 pg/ml does however show that the device is capable of detecting fluorescence from beads within a clinically useful concentration range for an acute inflammatory response [109]. Future experiments will aim to achieve the assay limit of detection of 1.5 pg/ml [111].

Fluorescence signal variation arises from a number of factors such as size variation of particles, variation in fluorophore concentration, fluctuation in laser power and vibration induced changes in input coupling efficiency. The primary source of signal variation for the measurement of calibration beads is due to positional variation in the Z dimension due to incomplete inertial focussing. The illumination intensity profile in the vertical direction has a Gaussian intensity profile with a spotsize of 4.3 µm and so a bead 1 µm off the vertical axis will be experience ~75% if the illumination intensity of an axially aligned bead. The most effective way to decrease signal variation is to reduce the variation in Z position by increasing the flow rate to ensure full inertial focussing is taking place. In device 2, increasing the flow rate to 0.27 µl/s ($U = 0.45$ m/s) would ensure that full inertial focussing is achieved at the analysis region positioned 22 mm downstream from the channel entrance. Another method to reduce the impact of the variable position of beads in the Z direction would be to use a deeper waveguide to produce a broader beam in the Z direction which would reduce the variation in illumination intensity per micron of Z translation.

6.4 Measurement of transmission signal of passing beads

6.4.1 Introduction

In addition to measurement of bead fluorescence the change in transmitted optical power from the input waveguide to the axially aligned output waveguide may be measured as beads pass through the beam. This transmission based detection of flowing beads allows measurement of the total count rate of beads, recognition of double signals and potentially synchronisation of fluorescence data collection for noise-reduction. Transmission based detection of flowing beads can also be used to measure bead velocity. For fully inertially focused beads, flowing on the same plane as the optical axis, the reduction in transmitted power should be directly related to bead diameter and so can be used to detect bead size [115]. If beads are not fully inertially focussed then the reduction in transmitted power was expected to also be related to the displacement of a bead in the Z dimension from the centre of the beam.

A study was conducted to measure the change in transmitted optical power from the input waveguide to the output waveguide as beads pass through the beam. From the simulations of the transmission signal of beads in Chapter 3 the transmission signal was expected to predominantly show a reduction in transmission as the bead deflects the beam and possibly a slight increase if the bead acts as a lens to focus light into the collection waveguide.

6.4.2 Materials and method

Device 2 was used to measure the transmission signal of the beads. This device had a microfluidic channel 21.1 µm ± 0.1 µm wide by 30.5 µm ± 0.5 µm deep. The input/output pair of waveguides used were 9.2 µm wide by 2.0 µm deep and located 22 mm downstream from the microfluidic channel entrance. The same free space fluorescence imaging system used shown in Figure 6.1 was used as to image the fluorescence from calibration beads whilst transmission measurements were taken. This was done in order to confirm inertial focussing was taking place and also measure the intensity profile of the beam. To measure the effect of beads flowing through the beam on the optical transmission between the input and output waveguide, the output waveguide was butt-coupled to a 60 µm diameter core multimode fibre connected to an avalanche photodetector (APD) (APD120A2/M, Thorlabs, USA) with an output bandwidth of 50 MHz. The zero baseline power was determined with the laser turned off, to allow determination of fractional transmission across the channel. A fluorescent bead suspension (Inspeck Orange, ThermoFisher, USA) at 10 beads/µl concentration was prepared and flowed through the device at flow rates of 0.2 µL/s and 0.05 µL/s whilst transmission measurements were recorded. The higher flow rate was used to ensure good confinement of the beads by inertial focussing and the lower flow rate was used to take transmission measurements when beads were not being inertially focussed. The power transmitted across the fluidic channel and collected by the output waveguide was acquired multiple times on a digital oscilloscope recording 10^5 data points at 200 ns interval. Each acquisition was initiated manually and displayed on the scope screen and checked by eye, any acquisitions containing a bead signal were saved.

6.4.3 Results and discussion

To confirm that inertial focussing was taking place at a flow rate of 0.2 µl/s ($U = 0.33$ m/s), during the period that the transmission measurements were recorded, a video of the fluorescence streaks was acquired during the same time period. The summed image of all the fluorescence streaks would also reveal the intensity profile of the illumination beam in the Y direction and inform the interpretation of the measured transmission signals. Figure 6.9 shows an image combining the fluorescence from 163 beads which passed through the channel during the time the transmission data was acquired with a driving flow rate of 0.2 µl/s. The left and right streaks of fluorescence confirm beads are well confined to left and right inertial focussing equilibrium positions. At each equilibrium position the average displacement of the bead centre from the nearest channel wall was 5 µm ± 1 µm. As observed in the immunoassay experiments, with the same device, there was a bias of beads to pass on one side as the ratio of beads which passed at the left and right equilibrium positions was 3 to 2 respectively. This bias is reversed compared to the measurements taken for the immunoassay indicating that the bias is unstable and may be dependent on beads clumping on one side in the reservoir before being fed into the channel. The bias is not represented in the image in Figure 6.9, as the pixel intensity for the right and left beads have been normalised to represent the intensity distribution on the right and left equally even though more beads passed on the right. Inertial focussing in the Z dimension was confirmed by 63% of beads flowing through the beam with a fluorescence energy CV of 28% for the beads at the right equilibrium position. The intensity profile in the Y direction for left and right beads is shown in Figure 6.9 and reveals the beam has a multilobed intensity profile due to the multimode excitation waveguide. The beam intensity profile for the right side beads has 2 asymmetric peaks while the beam intensity profile for the left side beads has 2 or possibly 3 asymmetric peaks. The beam width in the Y direction, defined as the full width of the intensity profile at $1/e^2$ of the intensity profile maximum, was 9.6 µm for the right beads and 10.0 µm for the left beads.

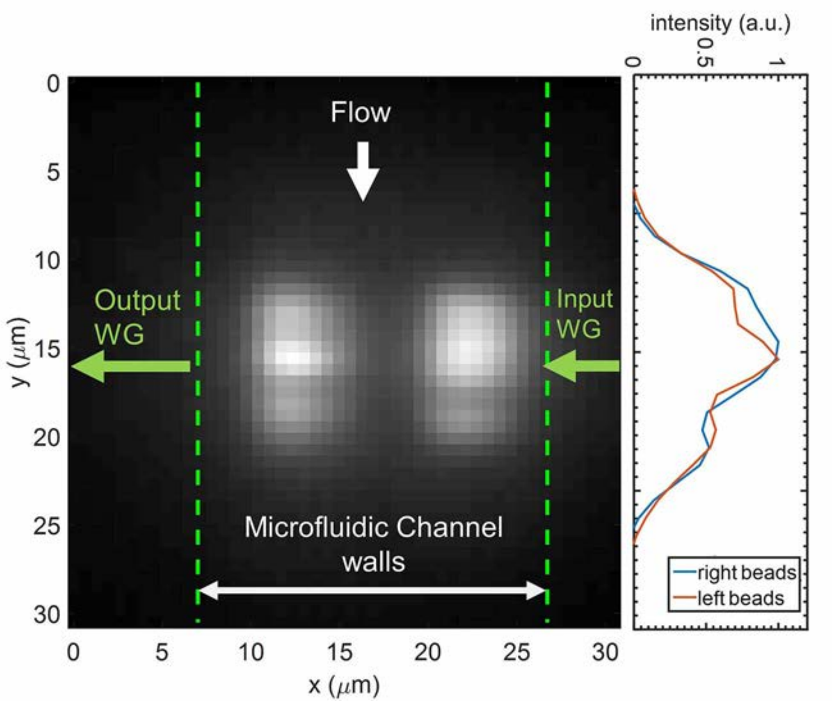

Figure 6.9: Fluorescence microscope image showing the summed fluorescence from 163 beads which have flowed through the beam driven at a flow rate of 0.2 µl/s during the period when the transmission measurements were taken. Intensity in the Y direction is proportional to the excitation beam intensity.

Transmission data for 15 beads were collected to evaluate the change in transmitted power for nominally identical beads. Figure 6.10(a) and (b) show the change in transmissivity across the fluidic channel measured from the output waveguide as beads flow through the beam, normalised to the transmissivity with buffer solution alone flowing in the channel, for flow rates of 0.2 µL/s and 0.05 µL/s, respectively. In Figure 6.10(a), in the case of the higher flow rate, beads 1 and 2 show large decreases in transmission (decreases of 71% and 59% respectively) indicating that a large proportion of the optical power leaving the input waveguide is absorbed or deflected away from the output waveguide by the bead. The signal variation of the baseline transmission signal was recorded as the standard deviation of the transmission signal recorded when only buffer was flowing in the fluidic channel over 10 acquisition cycles and was 1.14%. The minimum detectable change in transmission, defined as a transmission change of thrice the baseline transmission signal, was therefore 3.42%. The signal to noise ratio for transmission based detection was calculated using equation 3.6 with $\sigma_B = 1.14\,\%$ giving a maximum signal to noise ratio of 61 for the maximum ΔT of 71%. This signal to noise ratio is better than transmission based detection on a similar integrated optical microflow cytometer developed by Rosenauer et al who used a chip with photoresist waveguides to detect 12 µm beads with a signal to noise ratio of 26 [115]. The high signal to noise ratio measured on the device in this thesis shows promise for detection of particles of <5.6 µm in diameter which will incur a lower change in transmission.

According to the simulations of the transmission signal of a passing bead, performed in Chapter 3, the increased refractive index of the bead, combined with its circular shape can act to refract light away from the output waveguide causing a transmission decrease up to 88%. Such a large transmission decrease was not observed experimentally because the illumination beam used is at least 4 µm wider than the bead diameter and so even when the bead is entirely within the beam there is always some light transmitted to the output waveguide which does not interact with the bead. In addition the beads are not fully confined in the Z direction and so some light may pass under or above a bead without interacting with the bead. Other contributing causes for the decrease in transmission in the experimental transmission measurements are absorption of light by the fluorophore in the bulk of the bead, and deflection of the light away from the output waveguide by either reflection at the buffer-bead interface if the bead surface is smooth or by scattering.

The amplitude of the transmission decrease is believed to be related to the volume of bead which is interacting with the beam with a greater interacting volume causing a greater decrease in transmission. This relationship has been observed by Rosenauer et al [115]. In the case of the transmission measurements taken in this thesis, where all beads are of the same diameter, it is thought that the amplitude dip of the transmission represents the Z displacement of a bead from the centre of the beam so that a bead with zero displacement will produce the maximum possible decrease in transmission. This measurement would therefore be useful for assessing the Z confinement of flow streams to confirm inertial focussing. It is envisaged that transmission based detection of particle size would be particularly useful for alternative applications such as the detection of the size of cells and microvesicles. In future work the use of a data logging system will allow large numbers of transmission signals to be obtained enabling a more rigorous statistical evaluation.

Increases in transmission as beads passed through the beam were also measured. In Figure 6.10(a), bead 3 shows two peaks of increased transmission of 109 % and 106 % as the bead passes through the beam. When the flow rate was reduced to 0.05 µl/s a similar two peak increase was observed for beads 1 and 2 but over a longer time period due to the slower bead velocities. The simulations in Chapter 3 showed that the bead can act as a lens to focus more light into the collection waveguide increasing transmission. It is also possible that scattering or reflection from the surface of the bead may also contribute to an increase in transmission by directing more light into the output waveguide.

An additional observation is that the shape of the transmission dip for bead 1 in Figure 6.10(a) appears to reflect the shape of the beam Y intensity profile in Figure 6.9. It is supposed that the two minima in this signal coincide with the bead passing through the two intensity maxima of the illumination beam in the Y direction.

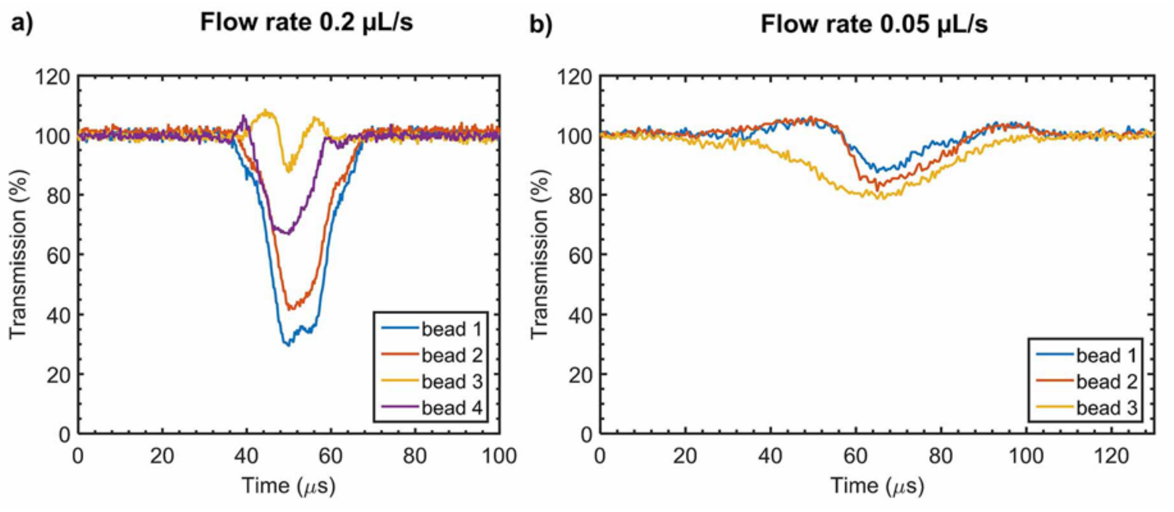

Figure 6.10: The change in optical power transmitted across the microfluidic channel as beads flow through the beam for flow rates (a) 0.2 µl/s and (b) 0.05 µl/s. Multiple bead signals are overlaid for comparison.

If all beads were fully inertially focussed and therefore confined to flow on the same plane as the excitation beam, the transit time of a bead passing through the beam could be used to calculated bead velocity, U_B. The transit time of a bead, t, was defined as the total time that the transmission power was greater than 3 standard deviations above or below the mean background transmission when only buffer was flowing. The beam width in the Y direction, ω_y, and the bead diameter, a, were then be used to calculate bead velocity using the following equation.

$$U_B = (\omega_y + a)/t \qquad 6.2$$

The measured mean bead velocity, for $\omega_y = 10.0$ µm, and $a = 5.6\ \mu m$ was 0.71 m/s ±0.22 m/s for a flow rate of 0.2 µl/s and 0.32 m/s ±0.09 m/s for a flow rate of 0.05 µl/s. The theoretical maximum flow velocity in the rectangular cross section microfluidic channel, U_m, was calculated to compare against the measured bead velocities using the following equation [49].

$$U_m = \frac{3}{2}\left(\frac{Q}{hw}\right) \qquad 6.3$$

Here Q is the flow velocity. The theoretical maximum flow velocities in the microfluidic channel of device 2 were 0.67 m/s and 0.17 m/s for flow rates of 0.2 µl/s and 0.05 µl/s respectively. The measured bead velocities were therefore faster than the theoretical maximum flow velocities indicating that the transmission based measurement of velocity overestimates bead velocity. The overestimation may be due to variation in the Z position of each bead as a bead with a centre displaced above or below the optical axis of the beam will present a smaller diameter to the beam and therefore will exhibit a shorter transit time. A method which will more accurately measure bead flow velocity, irrespective of the Z position of a bead is by using two sets of input/output waveguides of known separation and measuring the time difference between the transmission minima.

In summary, transmission based detection of flowing beads has been demonstrated with a signal to noise ratio of 61, showing good potential as an additional source of information for measuring bead size, velocity and Z displacement in the channel.

6.5 Conclusion

The three studies presented in this chapter have demonstrated that the fabricated microflow cytometer devices function as intended by the design specification. Characterisation of the distribution of flowing beads in the microfluidic channel has shown that inertial focussing acts to confine flowing immunoassay beads in two dimensions as intended by the design. Beads were well confined parallel to the short face of the channel into left and right equilibrium positions 5 µm ±1 µm from the channel walls. There was also partial confinement parallel to the long face of the channel indicated by 59 % of beads flowing through the illumination beam. This confinement was shown to effectively reduce the fluorescence signal variation from fluorescent calibration beads down to a CV of 29% which is only 9% higher than another inertial focussing fluorescence microflow cytometer in the literature [114]. Further confinement of the bead flow streams was expected at higher flow rates but could not be tested due to delamination of the chip at flow rates above 0.2 µl/s ($U = 0.33$ m/s). The device was used to measure the fluorescence from beads used in an immunoassay for TNFα and was demonstrated to detect fluorescence from bead samples incubated with TNFα at 154 pg/ml. Finally the device was used to demonstrate transmission based detection of flowing beads with a maximum signal to noise ratio of 61. This mode of detection shows promise to provide additional functionality for this microflow cytometry platform allowing measurement of particle size, velocity and Z displacement in the microfluidic channel.

The experiments conducted represent the first demonstration of an integrated optical microflow cytometer in an all glass system which combines integrated optics with inertial focussing.

CHAPTER 7

Conclusions and future work

7.1 Conclusions

The work presented in this thesis has demonstrated the realisation of a silica-based microflow cytometer combining inertial focussing with integrated optics suitable for performing bead based immunoassays. This work was motivated by the need to integrate a light control system with microfluidics enabling the mass production of low cost, compact, high performance microflow cytometers. Integrated optical waveguides were identified as the ideal system to achieve this as they offer compact, precise light control and are intrinsically aligned to the microfluidic structures during fabrication. A silica-based material system was selected for efficient optical coupling, and the potential for low propagations losses, low absorption and low autofluorescence in the visible wavelength range as well as mechanical and chemical robustness. Silica chips can also be mass produced using conventional fabrication techniques employed by the microelectronics industry, reducing costs. A suitable application for the proposed microflow cytometer was identified as that of bead based immunoassays due to the well-established fluorescence properties of commercially available beads and the immediate applications in biological and medical research.

A range of techniques for particle focussing in microfluidic channels were reviewed with respect to their suitability for combination with silica-based integrated waveguides. The main criteria were ease of integration, simplicity of fabrication using mass production techniques, simplicity of operation and minimisation of additional equipment bulk. The most established techniques use sheath fluid to hydrodynamically focus particles in 1 or 2 dimensions into the centre of a microfluidic channel. Typical structures used for 2D sheath based focussing require complex 3D fabrication processes which are not suitable for mass production and the extra pumps to control sheath fluid infusion add operational complexity and bulk to a device. Magnetic focussing with aligned soft magnetics tips is well suited for magnetic beads used in immunoassays however the system reviewed was bulky, required alignment and could not focus particles continuously which would limit the throughput of a device. Dielectrophoretic focussing shows good potential for full integration on chip and could also be used to sort particles downstream however the patterning of the electrodes would have added a third fabrication step increasing fabrication time and reducing yield. Inertial focussing using straight, rectangular cross section microfluidic channels was identified as the most suitable technique. The microfluidic channels are simple to fabricate by photolithography and deep reactive ion etching and control of the focussing only requires control of the flow rate at which the sample is injected. An additional useful feature of inertial focussing occurs when the particle concentration is high enough to bring the particles into close proximity (within 4 particle diameters). In this case flow proceeds with an even staggered spacing preventing coincident signals caused by multiple beads passing through a beam simultaneously.

The design of the optical light path in the microflow cytometer was addressed. A basic waveguide layout of axially aligned input and output channel waveguides bisected by a rectangular cross section microfluidic channel was devised. Positioning the waveguide layer halfway up the height of the microfluidic channel cross section would allow illumination of both inertial focussing equilibrium positions and allow transmission based detection of flowing beads. A silica based material system with a germania doped core was selected as the refractive index is similar to that used in the cores of commercially available optical fibres allowing efficient input and output coupling. The index contrast is sufficient to ensure the majority of the optical power is contained in the core allowing fine control of the spotsize by adjustment of the waveguide dimensions. The high silica content in the core material was also intended to minimise any difference in etch rates which can cause etch defects. The refractive indices of the deposited films at the wavelengths required for excitation of bead based assays were measured by ellipsometry and confirmed with prism coupling. The sputtered germania-silica films had a refractive index of 1.471 and 1.467 at wavelengths of 532 nm and 633 nm respectively. The PECVD silica had a refractive index of 1.461 and 1.456 at wavelengths of 532 nm and 633 nm respectively, and was shown to match that of bulk silica.

The measured refractive indices were used as parameters in the subsequent numerical simulations of the optical light path using the BeamPROP software which uses the beam propagation method. The waveguide dimensions required for single mode operation at both 532 nm and 637 nm wavelengths were determined to be 2 µm wide by 2 µm high. The coupling efficiency for butt-coupling of light with a single mode waveguide to a 2 µm wide by 2 µm high integrated waveguide were calculated as 0.90 and 0.84 for wavelengths of 532 nm and 633 nm respectively. Simulated mode profiles of the single mode waveguides confirmed the majority of the optical power is confined in the core. Simulations of the coupling efficiency of axially aligned channel waveguides, optically coupled across a microfluidic channel determined that a 20 µm microfluidic channel has a coupling efficiency of 0.79 and 0.88 for 2 µm and 10 µm waveguide widths respectively allowing enough light across to the collection waveguide for transmission based detection of flowing beads. The effect of a flowing bead interrupting transmission between waveguides by passing through the beam was simulated revealing a dual dip transmission signal caused by refraction based deflection of the beam by the passing bead. The transmission minima corresponded to a transmission dip of 78% which was expected to allow transmission based detection with a high signal to noise ratio.

The dimensions of the microfluidic channel required for inertial focussing of 5.6 µm diameter immunoassay beads were determined. The cross sectional dimensions were chosen to be 30 µm high and 20 µm wide and were determined from rules in the literature and also the limitations of the fabrication processes to be used. The channel length required for the devices was determined to be 30 mm by analysis of inertial focussing in PDMS test channels. A fabrication process using two masks and conventional microelectronics fabrication techniques was developed. The germania-silica waveguide films deposited by magnetron sputtering had a thickness of 2 µm ± 0.050 µm with a refractive index of 1.469 ±0.0007 at a wavelength of 633 nm. ICP etching produced waveguide structures 2.0 µm average width suitable for single mode operation and a range of waveguide widths up to 9.2 µm for multimode operation. An optimised PECVD process was developed as a viable method to deposit the 18 µm thick waveguide cladding layer with no stress induced cracking and at a refractive index matching bulk silica. Annealing of both the films deposited by magnetron sputtering and PECVD in the presence of oxygen was shown to reduce refractive index. Etching of the microfluidic channels with ICP etching produced trenches up to 30 µm deep with near vertical side walls at 91 $^{\circ}$±4.3° which are suitable for inertial focussing. Sealing of the microfluidic channel with a glass lid and SU-8 adhesive layer was shown to be effective up to a channel pressure drop of 5.18 bar (Flow rate of 0.2 µl/s). Three microflow cytometer devices were fabricated, devices 1 and 2 had microfluidic channels ~20 µm wide by ~30 µm deep and device 3 had a microfluidic channel ~15 µm wide by ~30 µm deep.

The optical path of the fabricated microflow cytometers devices were characterised. The 2.0 µm average width by 2.0 µm height waveguides were shown to be single mode at 532 nm and 637 nm respectively agreeing with BPM simulations. These waveguides were shown to produce Gaussian like mode intensity profiles with spotsizes measured at full width of $1/e^2$ maximum intensity of 2.5 µm and 3.0 µm at wavelengths of 532 nm and 637 nm respectively. The power budget for the fabricated devices was established to assess the impact of optical attenuation of device performance. As the measured spotsizes were similar to the simulated spotsizes, the coupling efficiency for the 2.0 µm wide by 2.0 high waveguide was approximated by the BPM simulation coupling efficiencies of 0.86 and 0.79 for wavelengths of 532 nm and 633 nm respectively. These high coupling efficiencies were expected to minimise the light propagating in the substrate ensuring a low background signal for fluorescence and transmission based detection of flowing beads. The propagation losses of the waveguides were high however still allowed enough optical power for fluorescence excitation at in the microfluidic channel and transmission across the chip. The insertion loss incurred by the 21.1 µm wide microfluidic channel in device 1 was measured at 2.75 dB and 3.6 dB for the 2.0 µm wide and 9.2 µm wide waveguides for input light at a wavelength of 532 nm with TE polarisation. These insertion losses were expected to be low enough to allow transmission based detection of flowing beads with a high signal to noise ratio. The shape of the beam launched by the input waveguide across the microfluidic channel was revealed by fluorescence imaging. The smallest beam width which could be produced was from the 2.0 µm wide waveguide and were 4.3 µm and 5.9 µm for the right and left equilibrium positions. The largest beam width was from the 9.2 µm wide waveguide which produced beam widths of 9.3 µm at the right and 9.9 µm at the left equilibrium positions. The wider beam was deemed to be the more suitable for fluorescence energy quantification using a microscope and CCD camera as it would allow a greater total illumination power without saturating the CCD camera ensuring a high signal to noise ratio. The wider beam was also thought to allow transmission based measurement of bead velocity with greater accuracy.

The performance of the fabricated devices as microflow cytometers were evaluated. Observation of fluorescence calibration beads flowing in the microfluidic channel revealed confinement of the bead flow streams in two dimensions by inertial focussing. Beads were well confined parallel to the short face of the channel into left and right equilibrium positions 5 µm ±1 µm from the channel walls. There was also partial confinement parallel to the long face of the channel indicated by 59 % of beads flowing through the illumination beam. This confinement was shown to effectively reduce the fluorescence signal variation from fluorescent calibration beads down to a CV of 29% which is only 9% higher than another inertial focussing fluorescence microflow cytometer in the literature [114]. Further confinement of the bead flow streams was expected at higher flow rates but could not be tested due to delamination of the chip at flow rates above a channel pressure drop of 5.18 bar ($Q = 0.2$ m/s, $U = 0.33$ m/s). A fluorescence bead immunoassay was conducted for the cytokine TNFα at a range of concentrations demonstrating the application of the device. The device was demonstrated to detect fluorescence from bead samples incubated with TNFα at 154 pg/ml. Finally the device was used to demonstrate transmission based detection of flowing beads. Flowing beads produced transmission attenuation of up to 71% corresponding to a maximum signal to noise ratio of 61. This mode of detection shows promise to provide additional functionality for this microflow cytometry platform allowing measurement of particle size, velocity and Z displacement in the microfluidic channel.

The devices produced and tested in this work are the first demonstration of a monolithic glass based microflow cytometer which combines integrated optics with inertial particle focussing. The platform allows mass production of robust chips with high quality optics offering a compact and affordable alternative to traditional flow cytometry machines. It is also expected that this adaptable platform can be applied to a variety flow cytometry applications including analysis of cells and microvesicles.

7.2 Future work

7.2.1 Overcoming pressure and blockage problems in the microfluidic channel

The long narrow dimensions of the microfluidic channel were designed primarily to inertially focus the beads. These dimensions however meant that the channel was liable to blocking and also had a high pressure drop which could cause delamination of the lid. The adhesive bonding process can be further optimised. Carlier et al have developed a method which has been tested up to 80 bar which uses a silane coupling agent covalently attached to the glass to promote adhesion to the SU-8 adhesive layer [73]. They also used a heated wafer bonding press to evenly apply a set amount of pressure to the bond ensuring good conformal contact of the adhesive to the wafer. Increasing the cross sectional area of the microfluidic channel will reduce blocking and but will increase the pressure drop across the channel because a longer channel and greater flow rate will be required to produce inertial focussing. For example a 40×60 μm^2 channel will require $Q = 1.28$ μl/s ($U = 0.53$ m/s) to produce focussing over $L_f = 14.9$ cm producing a pressure drop of 10.29 bar. As the height:width aspect ratio must be at least 3:2 for inertial focussing with two equilibrium positions, increasing the cross sectional area will also require thicker cladding and deeper etching in order to keep the waveguides halfway up the height of the channel. An alternative approach would be to swap the aspect ratio to 2:3 and using a spiral channel as discussed in section 7.2.3 may be a better solution as a greater cross sectional area can be used whilst minimising the cladding depth and etch depth required for the channel. Using a curving microchannel can also reduce the downstream length required to focus particles by up to a factor of 5 reducing the channel pressure drop by the same factor [54].

7.2.2 Planar chip top surface

A fully planarized chip top surface is desirable as it prevents bumps on the microfluidic channel floor after etching and also improves the adhesive sealing of the lid. Specialised chemical-mechanical planarization systems are available for chips fabricated on 4” or 6” circular wafers. The need for planarization can be avoided by using an altered waveguide layer pattern devised by Friis et al [29]. The structure shown in Figure 7.1 uses a narrow strip of waveguide core material framing the shape of the microfluidic channel. This means that the etched microfluidic channel has a flat bottom and there is a greater contact area on the top surface to improve the strength of the sealing.

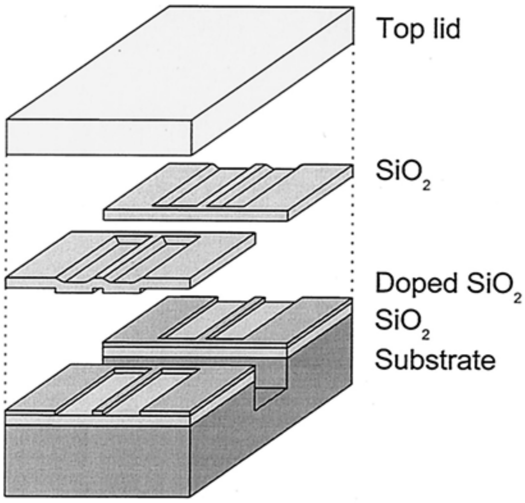

Figure 7.1: Structure of waveguide layer used by Friis et al allowing a flat bottom to an etched fluidic channel [29].

The extra strip of core material is narrow enough so that it does not significantly affect the shape of the beam launched across of the microfluidic channel.

7.2.3 Inertial focussing with a single equilibrium position

In order to remove the 12 % difference in fluorescence signal for beads on the near and far equilibrium positions the design of the microfluidic channel can be altered to produce only one equilibrium position. Curved microfluidic channels can be used to induce a secondary transverse flow know as Dean flow to push particles on to a single equilibrium positon. In a curving microchannel operating at channel Reynolds numbers greater than 1, the momentum of the faster moving flow at the centre of the channel forces it towards the outside of the channel. This movement induces recirculation flows which are directed back to the inner wall of the channel curve flowing along the top and bottom walls of the channel. A secondary flow destabilises the equilibrium position on the outside of the curve and also the equilibrium positions on the top or bottom of the channel leading to beads only flowing at the equilibrium position close to the inside wall of the curve. This process is illustrated in Figure 7.2.

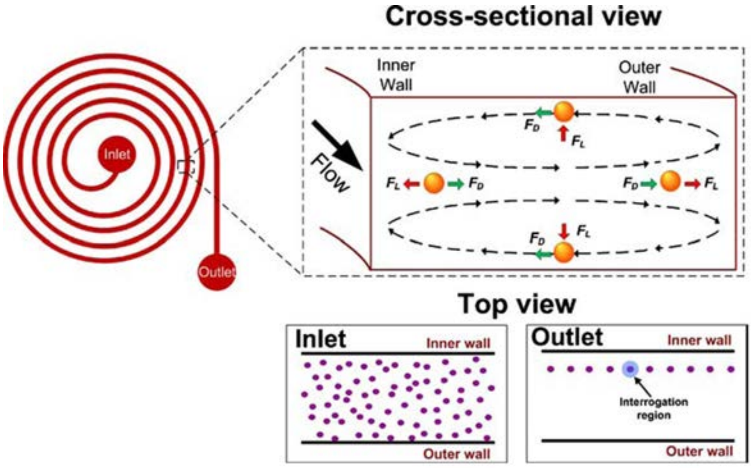

Figure 7.2: Schematic of a spiral channel used by Bhagat et al [114]. Inertial lift forces direct particles to equilibrium positions while recirculating Dean flows destabilised all inertial focussing positions except the one centred on the wall at the inside of the channel curve.

Spiral designs are compact and reduce overall chip length but reduce the accessibility of the microfluidic channel to waveguides [114]. An increased linear length at the end of the spiral would allow greater access. Sinusoidal microfluidic channels can be used to produce Dean flow and are more accessible for integration of waveguides [47], [57].

7.2.4 Reduction of signal variation from immunoassay beads

The high CV measured for the fluorescence bead immunoassay compared to the control beads indicated high variability in the amount of detection antibody binding to beads during the immunoassay procedure. The immunoassay protocol was adapted from the manufacturer’s protocol for a 250 µl sample volume in a 1.5 ml tube rather than the recommended 50 µl sample volume in a 96 well microplate. A 50 µl syringe could not be used to inject the sample because the volume of the tubing and filter before the chip was ~100 µl and so the sample would not have reached the chip. Instead a 250 µl volume syringe was used to inject the sample. Whilst the larger sample volume should not have affected the binding kinetics of the antibody-antigen interaction as the concentrations were the same, the mixing action and wash step mechanics were different. Inefficient mixing in the Eppendorf may have led to heterogeneous binding amongst each bead sample increasing the CV. An inefficient magnetic wash protocol may also have altered the amount of free analyte and free detection antibody present in the sample. This would have altered the amount of detection antibody bound to the beads leading to a fluorescence measurement that was unrepresentative of the analyte concentration. Future immunoassays will be conducted exactly to the manufacturer’s protocol with 50 µl sample volumes in a 96 well plate. A parallel sample injection loop can be included in the injection system so small sample volumes can be injected into the chip. In addition results will be verified with parallel measurements on a conventional Luminex flow cytometer and all data points will be from triplicate measurements.

7.2.5 Compact fluorescence collection

The free-space fluorescence collection system used in this work can be replaced with a more compact system. Off chip solutions include positioning a high numerical aperture fibre over the illumination region to collect fluorescence or placing a small area photodetector immediately over and close to this region. The ideal solution is on chip collection of fluorescence using wide waveguides with a high numerical aperture set at a minimum of 90 degrees to the excitation waveguide to minimise collection of pump light. Increasing the thickness of the waveguiding layer will improve collection efficiency but will introduce multimode behaviour to the excitation waveguide. Using a 2 µm thick waveguide layer with a 2 µm wide single mode input waveguide for illumination and a wide multimode output waveguide for collection would offer the best compromise for illumination and collection performance.

7.2.6 Device instrumentation and packaging.

The optical and fluidic apparatus used in this work to evaluate the device can be altered and packaged to make the device more user friendly. Precise sample injection can be enabled with the inclusion of a parallel sample loop injector which allows µl volumes to be injected into a flow stream without introducing bubbles into the system. As mentioned previously a large reduction in device footprint and operation complexity can be made by on chip fluorescence collection using waveguides or fibres. Permanently gluing fibres to the input and output waveguides will produce a very mechanically robust optical connection which does not need re-alignment. Fluorescence or transmission light signals can be detected by fibre coupled avalanche photodiodes which are connected to a data acquisition card with a fast sampling rate (2.8MS/s). Such data acquisition cards can be integrated with signal processing and control software such as labVIEW™ (National Instruments, US) which can be programmed to detect and log fluorescence or transmission peaks allowing real time presentation of the data. This software can also be used to control the laser power and pump flow rate.

7.2.7 Integration of optical focussing structures

Integrated structures such as kinoform microlenses [21] and multimode interference devices [20] for light focussing have been demonstrated and would allow narrow beam widths to be maintained across the wider microfluidic channels proposed in in sections 7.2.1 and 7.2.3. Multimode interference devices are particularly appealing as they have less stringent fabrication tolerances compared to kinoform microlenses. MMI devices consist of a single mode length of waveguide joined to a wider, multimode section of waveguide of an exact length. The multiple modes excited in the wider section constructively and destructively interfere with each other with propagation length resulting in reimaging of the single mode input at a particular distance from the input [116]. The microfluidic channel can be positioned at the end of the MMI device and the position of focus is determined by the MMI device length. MMI devices have been demonstrated to reimage single mode spots at a distances exceeding 40 µm into a microfluidic channel filled with DI water [20]. Such small spotsizes, maintained across a microfluidic channel can be used for characterisation of sub-micron diameter particles such as microvescicles.

7.2.8 Investigation of microvesicles

The small spotsize which can be produced by the integrated optical waveguides is useful for interrogation of small biological particles called microvesicles. Microvesicles are small fragments shed from the plasma membrane of cells which form into submicron diameter particles which can act as vectors for information exchange between cells [117]. They are typically shed by cells in response to specific stimuli, and shedding has been associated with a number of processes such as inflammation [118] and cancer progression [119] and as such they have been identified as a useful biomarker for investigations of health and disease. Elevated microvesicle numbers in the blood or expression of particular membrane proteins may indicate a disease state. Flow cytometry is commonly used to quantitatively assess microvesicle populations. Forward scatter measurements can count numbers and measure size, and fluorescence from specific stains can identify the proteins expressed on the surface of microvesicles. The ideal beam width for interrogating microvesicles is only slightly wider than the microvesicle diameter. In this case the chance of coincident signals from multiple particles is reduced and also the proportion of optical power interacting with the particle is maximised which ensures a high signal to noise ratio for scatter measurements[120].

Inertial focusing of microparticles using straight channels becomes impractical as very narrow channels are required which exert a very high channel pressure drop. For example, inertial focusing of 0.2 µm diameter particles would require a channel of $w \times h = 1.4 \times 2.8$ µm^2 and $L = 10$ mm which would have to operate at a flow rate of 0.05 µl/s ($U = 13.2$ m/s.) incurring a channel pressure drop of 1.2$\times 10^4$ bar. Instead, focusing techniques which employ dean flows for sample stream confinement are appealing as they can be implemented with channels of widths 10-300 µm [40], [121], [122]. The technique detailed in section 2.2 and shown Figure 2.2 which uses expanding and contracting sections of channel to induce dean vortices for vertical confinement could be easily applied to the current chip format [40]. Curving channels could also be used to induce dean flow based vertical confinement. A microflow cytometer devised by Mao et al (Figure 7.3) used a 90° bend in a channel to redirect a sheath input above and below a sample flow causing vertical confinement of the sample. Horizontal confinement was achieved by introducing a sheath flow from each side downstream of the bend [122].

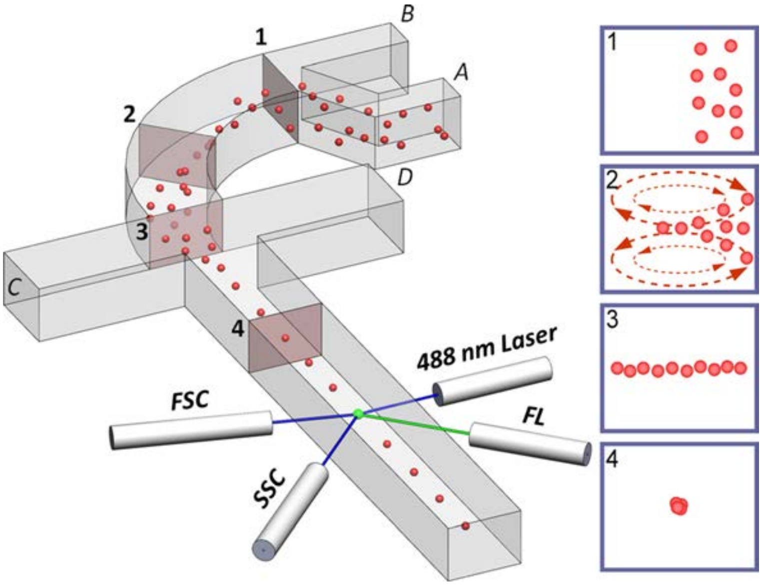

Figure 7.3: Vertical confinement of a sample input (A) by redirection of a sheath input (B) using induced dean flow at a 90° bend. Horizontal focussing is achieved downstream by side sheath inputs C and D. Image taken from [122]

7.2.9 Measurement of forward and side scatter

A configuration similar to the waveguide layout used by Kotz et al [25], shown in Figure 2.7, and Golden et al [38] would allow forward scatter and side scatter to be measured. Collection waveguides slightly offset from the excitation waveguide and at an angle of 0.5º-2.0º would collect the forward scatter and waveguides at an angle of 60º or greater would collect side scattered light. Narrower width waveguides would give finer discrimination of the scatter angle but would collect less light while wider waveguides would collect more light but reduce the angular discrimination. The addition of scattering measurements would allow the chip to be used to measure the size and internal structure of particles and could be applied to investigation of cell populations or microvesicles.

7.3 Concluding remarks

The work described in this thesis has produced a novel platform for microflow cytometry which integrates waveguides with deep microfluidic channels suitable for inertial particle focussing. The all glass platform offers a robust, mass producible system that can be adapted to include advanced integrated optical components allowing a multitude of flow cytometry applications to be developed.

List of references

[1] P. K. Cheo, “Integrated optical devices and applications,” *J.Phys.E:Sci.Intrum*, vol. 12, no. 2, pp. 1–12, 1979.

[2] Á. Ríos, M. Zougagh, and M. Avila, “Miniaturization through lab-on-a-chip: Utopia or reality for routine laboratories? A review,” *Anal. Chim. Acta*, vol. 740, pp. 1–11, 2012.

[3] T. Thorsen, “Microfluidic Large-Scale Integration,” *Science (80-.).*, vol. 298, no. 5593, pp. 580–584, 2002.

[4] D. Psaltis, S. R. Quake, and C. Yang, “Developing optofluidic technology through the fusion of microfluidics and optics,” *Nature*, vol. 442, no. 7101, pp. 381–386, 2006.

[5] A. Floris, S. Staal, S. Lenk, E. Staijen, D. Kohlheyer, J. Eijkel, and A. van den Berg, “A prefilled, ready-to-use electrophoresis based lab-on-a-chip device for monitoring lithium in blood,” *Lab Chip*, vol. 10, no. 14, p. 1799, 2010.

[6] C. M. Puleo, W. McIntosh Ambrose, T. Takezawa, J. Elisseeff, and T.-H. Wang, “Integration and application of vitrified collagen in multilayered microfluidic devices for corneal microtissue culture.,” *Lab Chip*, vol. 9, no. 22, pp. 3221–7, 2009.

[7] Q. Ramadan, H. Jafarpoorchekab, C. Huang, P. Silacci, S. Carrara, G. Koklü, J. Ghaye, J. Ramsden, C. Ruffert, G. Vergeres, and M. a M. Gijs, “NutriChip: nutrition analysis meets microfluidics.,” *Lab Chip*, vol. 13, no. 2, pp. 196–203, 2013.

[8] J. P. Hauschild, E. Wapelhorst, and J. Müller, “Mass spectra measured by a fully integrated MEMS mass spectrometer,” *Int. J. Mass Spectrom.*, vol. 264, no. 1, pp. 53–60, 2007.

[9] S. Schumacher, J. Nestler, T. Otto, M. Wegener, E. Ehrentreich-Förster, D. Michel, K. Wunderlich, S. Palzer, K. Sohn, A. Weber, M. Burgard, A. Grzesiak, A. Teichert, A. Brandenburg, B. Koger, J. Albers, E. Nebling, and F. F. Bier, “Highly-integrated lab-on-chip system for point-of-care multiparameter analysis,” *Lab Chip*, vol. 12, no. 3, p. 464, 2012.

[10] P. Hua, J. Hole, J. Wilkinson, G. Proll, J. Tschmelak, G. Gauglitz, M. Jackson, R. Nudd, H. Griffith, R. Abuknesha, J. Kaiser, and P. Kraemmer, “Integrated optical fluorescence multisensor for water pollution,” *Opt. Express*, vol. 13, no. 4, pp. 1124–1130, 2005.

[11] F. S. Ligler and J. S. Kim, *The microflow cytometer*, 1st ed. Pan Standford Publishing, 2010.

[12] P. F. Mullaney, “Cell Sizing: A Light Scattering Photometer for Rapid Volume Determination,” *Rev. Sci. Instrum.*, vol. 40, no. 8, p. 1029, 1969.

[13] R. a Hoffman, P. C. Kung, W. P. Hansen, and G. Goldstein, “Simple and rapid measurement of human T lymphocytes and their subclasses in peripheral blood.,” *Proc. Natl. Acad. Sci. U. S. A.*, vol. 77, no. 8, pp. 4914–4917, 1980.

[14] N. Baumgarth and M. Roederer, “A practical approach to multicolor flow cytometry for immunophenotyping,” *J. Immunol. Methods*, vol. 243, no. 1–2, pp. 77–97, 2000.

[15] X. Xuan, J. Zhu, and C. Church, “Particle focusing in microfluidic devices,” *Microfluid. Nanofluidics*, vol. 9, no. 1, pp. 1–16, Mar. 2010.

[16] D. Holmes, J. K. She, P. L. Roach, and H. Morgan, “Bead-based immunoassays using a micro-chip flow cytometer.,” *Lab Chip*, vol. 7, no. 8, pp. 1048–1056, 2007.

[17] N. Hashemi, J. S. Erickson, J. P. Golden, K. M. Jackson, and F. S. Ligler, “Microflow Cytometer for optical analysis of phytoplankton.,” *Biosens. Bioelectron.*, vol. 26, no. 11, pp. 4263–9, Jul. 2011.

[18] J. S. Kim, G. P. Anderson, J. S. Erickson, J. P. Golden, M. Nasir, and F. S. Ligler, “Multiplexed detection of bacteria and toxins using a microflow cytometer,” *Anal. Chem.*, vol. 81, no. 13, pp. 5426–5432, 2009.

[19] R. Zmijan, D. C. Spencer, M. C. Mowlem, and H. Morgan, “Differentiation of micro spheres by narrow angle scattered light detection on low cost PMMA micro flow cytometer chip,” in *15 th international conference on minituarised systems for chemistry and life sciences*, 2011, pp. 1263–1265.

[20] H. C. Hunt and J. S. Wilkinson, “Multimode interference devices for focusing in microfluidic channels.,” *Opt. Lett.*, vol. 36, no. 16, pp. 3067–9, Aug. 2011.

[21] H. C. Hunt and J. S. Wilkinson, “Kinoform microlenses for focusing into microfluidic channels.,” *Opt. Express*, vol. 20, no. 9, pp. 9442–57, Apr. 2012.

[22] K. Suzuki, Y. Hida, T. Shibata, Y. Inoue, H. Takahashi, and K. Okamoto, “Silica-based arrayed-waveguide gratings for the visible wavelength range,” *NTT Tech. Rev.*, vol. 4, no. 6, pp. 48–51, 2006.

[23] Z. Cai, W. Qiu, G. Shao, and W. Wang, “A new fabrication method for all-PDMS waveguides,” *Sensors Actuators A Phys.*, vol. 204, pp. 44–47, 2013.

[24] K. B. Mogensen, J. El-Ali, A. Wolff, and J. P. Kutter, “Integration of polymer waveguides for optical detection in microfabricated chemical analysis systems.,” *Appl. Opt.*, vol. 42, no. 19, pp. 4072–4079, 2003.

[25] K. T. Kotz, A. C. Petrofsky, R. Haghgooie, R. Granier, M. Toner, and R. G. Tompkins, “Inertial focusing cytometer with integrated optics for particle characterization,” *Technology*, vol. 01, no. 01, pp. 27–36, Sep. 2013.

[26] R. Kitamura, L. Pilon, and M. Jonasz, “Optical constants of silica glass from extreme ultraviolet to far infrared at near room temperature,” *Appl. Opt.*, vol. 46, no. 33, p. 8118, 2007.

[27] R. Brückner, “Properties and structure of vitreous silica. I,” *J. Non. Cryst. Solids*, vol. 5, no. 2, pp. 123–175, Nov. 1970.

[28] C. Iliescu, H. Taylor, M. Avram, J. Miao, and S. Franssila, “A practical guide for the fabrication of microfluidic devices using glass and silicon,” *Biomicrofluidics*, vol. 6, no. 1, pp. 16505–1650516, 2012.

[29] P. Friis, K. Hoppe, O. Leistiko, K. B. Mogensen, J. Hübner, and J. P. Kutter, “Monolithic integration of microfluidic channels and optical waveguides in silica on silicon.,” *Appl. Opt.*, vol. 40, no. 34, pp. 6246–6251, 2001.

[30] J. M. Berg, J. L. Tymoczko, and L. Stryer, *Biochemistry*, 6th ed. Freeman, 2006.

[31] J. R. Kettman, T. Davies, D. Chandler, K. G. Oliver, and R. J. Fulton, “Classification and properties of 64 multiplexed microsphere sets,” *Cytometry*, vol. 33, no. 2, pp. 234–243, 1998.

[32] W. de Jager, H. te Velthuis, B. J. Prakken, W. Kuis, and G. T. Rijkers, “Simultaneous detection of 15 human cytokines in a single sample of stimulated peripheral blood mononuclear cells,” *Clin. Diagn. Lab. Immunol.*, vol. 10, no. 1, pp. 133–139, 2003.

[33] F. Chowdhury, A. Williams, and P. Johnson, “Validation and comparison of two multiplex technologies, Luminex® and Mesoscale Discovery, for human cytokine profiling,” *J. Immunol. Methods*, vol. 340, no. 1, pp. 55–64, 2009.

[34] G. Blankenstein and U. D. Larsen, “Modular concept of a laboratory on a chip for chemical and biochemical analysis,” *Biosens. Bioelectron.*, vol. 13, no. 3–4, pp. 427–438, 1998.

[35] D. P. Schrum, C. T. Culbertson, S. C. Jacobson, and J. M. Ramsey, “Microchip flow cytometry using electrokinetic focusing.,” *Anal. Chem.*, vol. 71, no. 19, pp. 4173–7, 1999.

[36] R. Yang, D. L. Feeback, and W. Wang, “Microfabrication and test of a three-dimensional polymer hydro-focusing unit for flow cytometry applications,” *Sensors Actuators A Phys.*, vol. 118, no. 2, pp. 259–267, 2005.

[37] P. B. Howell, J. P. Golden, L. R. Hilliard, J. S. Erickson, D. R. Mott, and F. S. Ligler, “Two simple and rugged designs for creating microfluidic sheath flow.,” *Lab Chip*, vol. 8, no. 7, pp. 1097–103, Jul. 2008.

[38] J. P. Golden, J. S. Kim, J. S. Erickson, L. R. Hilliard, P. B. Howell, G. P. Anderson, M. Nasir, and F. S. Ligler, “Multi-wavelength microflow cytometer using groove-generated sheath flow.,” *Lab Chip*, vol. 9, no. 13, pp. 1942–50, Jul. 2009.

[39] C. J. Morgan, R. R. Vallance, and E. R. Marsh, “Micro-machining and micro-grinding with tools fabricated by micro electro-discharge machining,” *Int. J. Nanomanuf.*, vol. 1, no. 2, pp. 242–258, 2006.

[40] M. G. Lee, S. Choi, and J.-K. Park, “Three-dimensional hydrodynamic focusing with a single sheath flow in a single-layer microfluidic device.,” *Lab Chip*, vol. 9, no. 21, pp. 3155–60, Nov. 2009.

[41] S.-Y. Yang, K.-Y. Lien, K.-J. Huang, H.-Y. Lei, and G.-B. Lee, “Micro flow cytometry utilizing a magnetic bead-based immunoassay for rapid virus detection.,” *Biosens. Bioelectron.*, vol. 24, no. 4, pp. 861–8, Dec. 2008.

[42] R. Afshar, Y. Moser, T. Lehnert, and M. a M. Gijs, “Three-dimensional magnetic focusing of superparamagnetic beads for on-chip agglutination assays.,” *Anal. Chem.*, vol. 83, no. 3, pp. 1022–9, Mar. 2011.

[43] J. Vykoukal, D. M. Vykoukal, J. A. Schwartz, and P. R. C. Gascoyne, “A three-dimensional dielectrophoretic particle focusing channel for microcytometry applications,” *J. Microelectromechanical Syst.*, vol. 14, no. 3, pp. 480–487, Jun. 2005.

[44] D. Holmes, H. Morgan, and N. G. Green, “High throughput particle analysis: Combining dielectrophoretic particle focussing with confocal optical detection,” *Biosens. Bioelectron.*, vol. 21, no. 8, pp. 1621–1630, 2006.

[45] S. Fiedler, S. G. Shirley, T. Schnelle, and G. Fuhr, “Dielectrophoretic sorting of particles and cells in a microsystem.,” *Anal. Chem.*, vol. 70, no. 9, pp. 1909–1915, 1998.

[46] G. Segre and A. Silberberg, “Radial Particle Displacements in Poiseuille Flow of Suspensions,” *Nature*, vol. 189, no. 4760, pp. 209–210, Jan. 1961.

[47] D. Di Carlo, D. Irimia, R. G. Tompkins, and M. Toner, “Continuous inertial focusing, ordering, and separation of particles in microchannels.,” *Proc. Natl. Acad. Sci. U. S. A.*, vol. 104, no. 48, pp. 18892–7, Nov. 2007.

[48] J. M. Martel and M. Toner, “Inertial focusing in microfluidics.,” *Annu. Rev. Biomed. Eng.*, vol. 16, pp. 371–96, 2014.

[49] H. Amini, W. Lee, and D. Di Carlo, “Inertial microfluidic physics.,” *Lab Chip*, vol. 14, no. 15, pp. 2739–61, 2014.

[50] S. C. Hur, H. T. K. Tse, and D. Di Carlo, “Sheathless inertial cell ordering for extreme throughput flow cytometry.,” *Lab Chip*, vol. 10, no. 3, pp. 274–80, Feb. 2010.

[51] J.-P. Matas, J. F. Morris, and É. Guazzelli, “Inertial migration of rigid spherical particles in Poiseuille flow,” *J. Fluid Mech.*, vol. 515, pp. 171–195, 2004.

[52] E. S. Asmolov, “The inertial lift on a spherical particle in a plane Poiseuille flow at large channel Reynolds number,” *J. Fluid Mech.*, vol. 381, pp. 63–87, 1999.

[53] L. Zeng, F. Najjar, S. Balachandar, and P. Fischer, “Forces on a finite-sized particle located close to a wall in a linear shear flow,” *Phys. Fluids*, vol. 21, no. 3, p. 033302, 2009.

[54] J. Zhou and I. Papautsky, “Fundamentals of inertial focusing in microchannels.,” *Lab Chip*, vol. 13, no. 6, pp. 1121–32, Feb. 2013.

[55] D. R. Gossett, H. T. K. Tse, J. S. Dudani, K. Goda, T. A. Woods, S. W. Graves, and D. Di Carlo, “Inertial Manipulation and Transfer of Microparticles Across Laminar Fluid Streams,” *Small*, vol. 8, no. 17, pp. 2757–2764, 2012.

[56] C. Liu, G. Hu, X. Jiang, and J. Sun, “Inertial focusing of spherical particles in rectangular microchannels over a wide range of Reynolds numbers,” *Lab Chip*, vol. 15, no. 4, pp. 1168–1177, 2015.

[57] J. Oakey, R. W. Applegate, E. Arellano, D. Di Carlo, S. W. Graves, and M. Toner, “Particle focusing in staged inertial microfluidic devices for flow cytometry.,” *Anal. Chem.*, vol. 82, no. 9, pp. 3862–7, May 2010.

[58] R. Marz, *Integrated optics design and modelling*. 1995.

[59] Thorlabs, “Single Mode Fiber : 405 to 532 nm,” 2015.

[60] R. D. Maurer and P. C. Schultz, “Germania containing optical waveguide,” 1975.

[61] A. S. Huang, Y. Arie, C. C. Neil, and J. M. Hammer, “Study of refractive index of GeO2:SiO2 mixtures using deposited-thin-film optical waveguides,” *Appl. Opt.*, vol. 24, no. 24, pp. 4404–4407, 1985.

[62] H. G. Tompkins, *A User’s guide to ellipsometry*. Elsevier, 1993.

[63] J. Singh, *Optical properties of condensed matter and applications*. Wiley, 2007.

[64] P. K. Tien and R. Ulrich, “Theory of Prism-Film Coupler and Thin-Film Light Guides,” *J. Opt. Soc. Am.*, vol. 60, no. 10, p. 1325, 1970.

[65] M. Mansuripur, “The beam propagation method,” in *Classical Optics and Its Applications*, 2nd ed., Cambridge University Press, 2009, pp. 459–475.

[66] H. C. Hunt, “Integrated Microlenses and Multimode Interference Devices for Microflow Cytometers,” University of Southampton, 2010.

[67] H. Nishihara, M. Haruna, and T. Suhara, *Optical integrated circuits*, 1st ed. McGraw-Hill, 1985.

[68] Thorlabs, “SM600 - Single mode fiber specification,” 2015.

[69] Thorlabs, “Single Mode Fiber : 488-633 nm,” 2013.

[70] G. Ajoy and T. K., *Introduction to fibre optics*, 1st ed. Cambridge university press, 1998.

[71] Marcuse, “Loss analysis of single-mode fiber splices.pdf,” *Bell System Technical Journal*, vol. 56, no. 5. pp. 703–718, 1976.

[72] M. J. Fuerstman, A. Lai, M. E. Thurlow, S. S. Shevkoplyas, H. a Stone, and G. M. Whitesides, “The pressure drop along rectangular microchannels containing bubbles.,” *Lab Chip*, vol. 7, no. 11, pp. 1479–1489, 2007.

[73] J. Carlier, K. Chuda, S. Arscott, V. Thomy, B. Verbeke, X. Coqueret, J. C. Camart, C. Druon, and P. Tabourier, “High pressure-resistant SU-8 microchannels for monolithic porous structure integration,” *J. Micromechanics Microengineering*, vol. 16, no. 10, pp. 2211–2219, Oct. 2006.

[74] H. Becker and C. Gärtner, “Polymer microfabrication technologies for microfluidic systems.,” *Anal. Bioanal. Chem.*, vol. 390, no. 1, pp. 89–111, 2008.

[75] D. C. Duffy, J. C. McDonald, O. J. A. Schueller, and G. M. Whitesides, “Rapid Prototyping of Microfluidic Systems in Poly(dimethylsiloxane),” *Anal. Chem.*, vol. 70, no. 23, pp. 4974–4984, 1998.

[76] M. J. Owen and P. J. Smith, “Plasma treatment of polydimethylsiloxane,” *J. Adhes. Sci. Technol.*, vol. 8, no. 10, pp. 1063–1075, 1993.

[77] M. A. Eddings, M. A. Johnson, and B. K. Gale, “Determining the optimal PDMS–PDMS bonding technique for microfluidic devices,” *J. Micromechanics Microengineering*, vol. 18, no. 6, p. 067001, Jun. 2008.

[78] A. Piruska, I. Nikcevic, S. H. Lee, C. Ahn, W. R. Heineman, P. A. Limbach, and C. J. Seliskar, “The autofluorescence of plastic materials and chips measured under laser irradiation,” *Lab Chip*, vol. 5, no. 12, pp. 1348–1354, 2005.

[79] M. J. Madou, *Fundamentals of Microfabrication and Nanotechnology: Volume 2*, Third. CRC Press, 2012.

[80] C. Ho, K. Pita, N. Q. Ngo, and C. H. Kam, “Optical functions of (x)GeO2:(1-x)SiO2 films determined by multi-sample and multi-angle spectroscopic ellipsometry.,” *Opt. Express*, vol. 13, no. 3, pp. 1049–54, Feb. 2005.

[81] K. D. Mackenzie, D. J. Johnson, M. W. Devre, R. J. Westerman, and B. H. Reelfs, “Stress control of Si-Based PECVD Dieletrics,” in *Silicon Nitride and Silicon Dioxide thin insulating films and other emerging dielectrics VIII*, 2005, no. May, pp. 148–159.

[82] D. H. Kim, Y. T., Cho, S. M., Seo, Y. G., Yoon, H. D. Im, Y. M., Yoon, “Influence of hydrogen on SiO2 thick film deposited by PECVD and FHD for silica optical waveguide,” *Cryst. Res. Technol.*, vol. 37, no. 12, pp. 1257–1263, 2002.

[83] E. Quartarone, P. Mustarelli, F. Marabelli, M. Battagliarin, and S. Turato, “GeO2-doped SiO2 sputtered thin films: Microstructure, stoichiometry, and optical properties,” *J. Vac. Sci. Technol. A Vacuum, Surfaces, Film.*, vol. 22, no. 6, p. 2234, 2004.

[84] UQG-Optics, “UV fused silica-spectrosil,” 2015.

[85] G. D. Emmerson, S. P. Watts, C. B. E. Gawith, V. Albanis, M. Ibsen, R. B. Williams, and P. G. R. Smith, “Fabrication of directly UV-written channel waveguides with simultaneously defined integral Bragg gratings,” *Electron. Lett.*, vol. 38, no. 24, pp. 1531–1532, 2002.

[86] A. L. Bogdanov, J. Lapointe, and J. H. Schmid, “Electron-beam lithography for photonic waveguide fabrication: Measurement of the effect of field stitching errors on optical performance and evaluation of a new compensation method,” *J. Vac. Sci. Technol. B Microelectron. Nanom. Struct.*, vol. 30, no. 3, p. 031606, 2012.

[87] Michrochem Corp, “LOR and PMGI Resists,” 2015.

[88] F. Messow, C. Welch, A. Eifert, W. C. Ang, N. S. Hoe, T. Kusserow, and H. Hillmer, “Deep single step vertical ICP–RIE etching of ion beam sputter deposited SiO2/Si multilayer stacks,” *Microelectron. Eng.*, vol. 113, pp. 70–73, Jan. 2014.

[89] H. C. Lee, H. H. Hou, R. J. Yang, C. H. Lin, and L. M. Fu, “Microflow cytometer incorporating sequential micro-weir structure for three-dimensional focusing,” *Microfluid. Nanofluidics*, vol. 11, pp. 469–478, 2011.

[90] S. Bhattacharya, a. Datta, J. M. Berg, and S. Gangopadhyay, “Studies on surface wettability of poly(dimethyl) siloxane (PDMS) and glass under oxygen-plasma treatment and correlation with bond strength,” *J. Microelectromechanical Syst.*, vol. 14, no. 3, pp. 590–597, Jun. 2005.

[91] F. Niklaus, G. Stemme, J. Q. Lu, and R. J. Gutmann, “Adhesive wafer bonding,” *J. Appl. Phys.*, vol. 99, no. 3, 2006.

[92] S. Tuomikoski and S. Franssila, “Free-standing SU-8 microfluidic chips by adhesive bonding and release etching,” *Sensors Actuators, A Phys.*, vol. 120, no. 2, pp. 408–415, 2005.

[93] F. J. Blanco, M. Agirregabiria, J. Garcia, J. Berganzo, M. Tijero, M. T. Arroyo, J. M. Ruano, I. Aramburu, and K. Mayora, “Novel three-dimensional embedded SU-8 microchannels fabricated using a low temperature full wafer adhesive bonding,” *J. Micromechanics Microengineering*, vol. 14, pp. 1047–1056, 2004.

[94] B. G. Koehler and J. E. Bowers, “In-line single-mode fiber polarization controllers at 155, 130, and 0.63 µm,” *Appl. Opt.*, vol. 24, no. 3, p. 349, 1985.

[95] E. Hecht, *Optics*, 4th ed. Pearson education, 2002.

[96] Thermofisher, “Inspeck Microscope image intensity calibration kits,” 2001.

[97] W. S. Boyle and G. E. Smith, “Charge Coupled Semiconductor Devices,” *Bell Syst. Tech. J.*, vol. 49, no. 4, pp. 587–593, Apr. 1970.

[98] Hamamatsu Photonics, “ORCA R2 Digital CCD Camera,” 2015.

[99] H. M. Shapiro, *Practical Flow Cytometry*. Hoboken, NJ, USA: John Wiley & Sons, Inc., 2003.

[100] Y.-S. Choi, K.-W. Seo, and S.-J. Lee, “Lateral and cross-lateral focusing of spherical particles in a square microchannel.,” *Lab Chip*, vol. 11, no. 3, pp. 460–465, 2011.

[101] V. K. Singh and P. Guthikonda, “Circulating cytokines in Alzheimer’s disease,” *J. Psychiatr. Res.*, vol. 31, no. 6, pp. 657–660, 1996.

[102] S.-M. Kim, J. Song, S. Kim, C. Han, M. Park, Y. Koh, S. Jo, and Y.-Y. Kim, “Identification of peripheral inflammatory markers between normal control and Alzheimer’s disease,” *BMC Neurol.*, vol. 11, no. 1, p. 51, 2011.

[103] S. Ray, M. Britschgi, C. Herbert, Y. Takeda-Uchimura, A. Boxer, K. Blennow, L. F. Friedman, D. R. Galasko, M. Jutel, A. Karydas, J. A. Kaye, J. Leszek, B. L. Miller, L. Minthon, J. F. Quinn, G. D. Rabinovici, W. H. Robinson, M. N. Sabbagh, Y. T. So, D. L. Sparks, M. Tabaton, J. Tinklenberg, J. A. Yesavage, R. Tibshirani, and T. Wyss-Coray, “Classification and prediction of clinical Alzheimer’s diagnosis based on plasma signaling proteins,” *Nat Med*, vol. 13, no. 11, pp. 1359–1362, 2007.

[104] H. Fillit, W. Ding, L. Buee, J. Kalman, L. Altstiel, B. Lawlor, and G. Wolf-Klein, “Elevated circulating tumor necrosis factor levels in Alzheimer’s disease,” *Neurosci. Lett.*, vol. 129, no. 2, pp. 318–320, 1991.

[105] M. Reale, C. Iarlori, A. Thomas, D. Gambi, B. Perfetti, M. Di Nicola, and M. Onofrj, “Peripheral cytokines profile in Parkinson’s disease,” *Brain. Behav. Immun.*, vol. 23, no. 1, pp. 55–63, 2009.

[106] M. Reale, N. H. Greig, and M. A. Kamal, “Peripheral Chemo-Cytokine Profiles in Alzheimer’s and Parkinson's Diseases,” *Mini-Reviews Med. Chem.*, vol. 9, no. 10, pp. 1229–1241, 2009.

[107] S. Sotgiu, B. Zanda, B. Marchetti, M. L. Fois, G. Arru, G. M. Pes, F. S. Salaris, a. Arru, a. Pirisi, and G. Rosati, “Inflammatory biomarkers in blood of patients with acute brain ischemia,” *Eur. J. Neurol.*, vol. 13, no. 5, pp. 505–513, 2006.

[108] E. Dalaveris, T. Kerenidi, A. Katsabeki-Katsafli, T. Kiropoulos, K. Tanou, K. I. Gourgoulianis, and K. Kostikas, “VEGF, TNF-alpha and 8-isoprostane levels in exhaled breath condensate and serum of patients with lung cancer.,” *Lung Cancer*, vol. 64, no. 2, pp. 219–25, 2009.

[109] T. T. Bauer, C. Montón, A. Torres, H. Cabello, X. Fillela, A. Maldonado, J.-M. Nicolás, and E. Zavala, “Comparison of systemic cytokine levels in patients with acute respiratory distress syndrome, severe pneumonia, and controls,” *Thorax*, vol. 55, no. 1, pp. 46–52, 2000.

[110] T. Ishikawa, S. Kokura, N. Sakamoto, M. Okajima, T. Matsuyama, H. Sakai, Y. Okumura, S. Adachi, N. Yoshida, K. Uchiyama, O. Handa, T. Takagi, H. Konishi, N. Wakabayashi, N. Yagi, T. Ando, K. Uno, Y. Naito, and T. Yoshikawa, “Relationship between circulating cytokine levels and physical or psychological functioning in patients with advanced cancer,” *Clin. Biochem.*, vol. 45, no. 3, pp. 207–211, 2012.

[111] RnD sytems, “Mangetic Luminex Performance Assay Human TNF-alpha Kit,” 2015.

[112] D. J. Chandler and J. Bedre, “Magnetic microspheres for use in fluorescence-based applications,” US 8283037B2, 2012.

[113] R. T. Griffey, C. J. Trent, R. A. Bavolek, J. B. Keeperman, C. Sampson, and R. F. Poirier, “‘Hook-like Effect’ Causes False-negative Point-of-care Urine Pregnancy Testing in Emergency Patients,” *J. Emerg. Med.*, vol. 44, no. 1, pp. 155–160, 2013.

[114] A. A. S. Bhagat, S. S. Kuntaegowdanahalli, N. Kaval, C. J. Seliskar, and I. Papautsky, “Inertial microfluidics for sheath-less high-throughput flow cytometry,” *Biomed. Microdevices*, vol. 12, no. 2, pp. 187–195, 2010.

[115] M. Rosenauer, W. Buchegger, I. Finoulst, P. Verhaert, and M. Vellekoop, “Miniaturized flow cytometer with 3D hydrodynamic particle focusing and integrated optical elements applying silicon photodiodes,” *Microfluid. Nanofluidics*, vol. 10, no. 4, pp. 761–771, 2011.

[116] L. B. Soldano and E. C. M. Pennings, “Optical multi-mode interference devices based on self-imaging: principles and applications,” *J. Light. Technol.*, vol. 13, no. 4, pp. 615–627, 1995.

[117] J. Welsh, J. Holloway, and N. Englyst, “Internal Medicine : Open Access Microvesicles as Biomarkers in Diabetes , Obesity and Non-Alcoholic Fatty Liver Disease : Current Knowledge and Future Directions,” 2014.

[118] R. Andriantsitohaina, A. Gaceb, L. Vergori, and M. C. Martínez, “Microparticles as Regulators of Cardiovascular Inflammation,” *Trends Cardiovasc. Med.*, vol. 22, no. 4, pp. 88–92, 2012.

[119] V. Muralidharan-Chari, J. W. Clancy, A. Sedgwick, and C. D’Souza-Schorey, “Microvesicles: mediators of extracellular communication during cancer progression.,” *J. Cell Sci.*, vol. 123, no. Pt 10, pp. 1603–1611, 2010.

[120] a C. Matzdorff, G. Kühnel, B. Kemkes-Matthes, and H. Pralle, “Quantitative assessment of platelets, platelet microparticles, and platelet aggregates with flow cytometry.,” *J. Lab. Clin. Med.*, vol. 131, no. 6, pp. 507–517, 1998.

[121] X. Mao, J. R. Waldeisen, and T. J. Huang, “‘Microfluidic drifting’--implementing three-dimensional hydrodynamic focusing with a single-layer planar microfluidic device.,” *Lab Chip*, vol. 7, no. 10, pp. 1260–2, Oct. 2007.

[122] X. Mao, A. A. Nawaz, S.-C. S. Lin, M. I. Lapsley, Y. Zhao, J. P. McCoy, W. S. El-Deiry, and T. J. Huang, “An integrated, multiparametric flow cytometry chip using ‘microfluidic drifting’ based three-dimensional hydrodynamic focusing.,” *Biomicrofluidics*, vol. 6, no. 2, pp. 24113–241139, 2012.